

Indentation Methods in Experimental Rock Deformation



Dissertation

zur Erlangung des Grades eines
Doktors der Naturwissenschaften
der Fakultät für Geowissenschaften
an der Ruhr-Universität Bochum

vorgelegt von

Dorothee Dorner
aus Holzminden

Bochum, November 2002

Contents

1	Introduction	3
1.1	Objective and structure of the thesis	3
1.2	Approaches to rock rheology	4
1.3	Applying laboratory rheological data to geological conditions	5
1.4	Experimental rock deformation techniques	7
1.4.1	Apparatus used in uniaxial, triaxial, and torsion deformation experiments	7
1.4.2	Indentation hardness tests and indentation creep tests	8
2	Hardness anisotropy and slip systems of olivine investigated by high-temperature microindentation hardness tests	10
2.1	Abstract	10
2.2	Introduction	10
2.3	Method and material	11
2.3.1	Definition of hardness	11
2.3.2	Apparatus	11
2.3.3	Sample preparation, experimental procedure and analytical methods	11
2.3.4	Sample material	12
2.4	Results	14
2.4.1	Mechanical data	14
2.4.2	Morphology of indents	18
2.5	Discussion	21
2.5.1	Hardness anisotropy	21
2.5.2	Deformation regime	23
2.5.3	Comparison with other studies	24
2.6	Conclusions	24
3	An experimental study on the relative plastic strength of a clinopyroxene solid solution series using microindentation hardness tests	27
3.1	Abstract	27
3.2	Introduction	27

3.3	Definition of hardness	28
3.4	Apparatus and experimental procedure	28
3.5	Sample material	29
3.6	Results	30
3.6.1	Indentation hardness of jadeite and diopside	30
3.6.2	Hardness tests on omphacite	30
3.7	Discussion	35
3.7.1	Relative strength of the end members jadeite and diopside	35
3.7.2	Morphology of the indents	40
3.7.3	Unsystematic results on omphacite solid solutions	40
3.8	Summary and conclusions	42
4	Creep of a TiAl alloy: a comparison of indentation and tensile testing	44
4.1	Abstract	44
4.2	Introduction	44
4.3	Experimental	46
4.3.1	Sample material	46
4.3.2	Indentation and tensile creep testing	46
4.4	Results	48
4.4.1	Indentation and tensile creep data	48
4.4.2	Morphological and microstructural aspects of indentation creep testing	51
4.5	Discussion	53
4.5.1	Comparison of indentation and uniaxial tensile creep tests	53
4.5.2	Material bulging and dislocation mechanisms during indentation creep	57
4.6	Summary and conclusions	58
5	Summary and conclusions	61
5.1	Microindentation hardness tests	61
5.2	Indentation creep experiments	61

List of Figures

1	Scheme of the high-temperature microindentation apparatus.	12
2	Scheme of the sample assembly.	12
3	Room temperature FTIR spectra for olivine.	13
4	Hardness of olivine as a function of temperature.	14
5	Hardness versus temperature for two different olivine samples.	16
6	Hardness versus indenter orientation for two different olivine samples.	17
7	SEM images of indents in olivine crystals.	19
8	Scheme of slip lines.	20
9	Orientation of slip lines and corresponding slip planes in olivine.	20
10	Olivine hardness as a function of Schmid or Brookes factor.	26
11	a) High-temperature microindentation apparatus. b) Sample assembly.	29
12	Hardness of jadeite and diopside as a function of temperature.	31
13	Hardness of omphacite as a function of temperature.	33
14	SEM images of indents in omphacite.	34
15	Normalized hardness of jadeite and diopside as a function of temperature I.	37
16	Normalized hardness of jadeite and diopside as a function of temperature II.	38
17	Hardness of jadeite and diopside for different temperatures as a function of the temperature dependent shear modulus.	39
18	SEM image of an indent in jadeite.	41
19	Orientation of linear features in two jadeite and two diopside samples.	41
20	a) Central part of the creep test rig. b) Scheme of the sample assembly for indentation creep experiments with a cylindrical indenter.	47
21	Indentation creep curves for a TiAl alloy.	50
22	Log-log plot of indentation rate versus net section stress for a temperature of 1050 °C.	51
23	Log-log plot of indentation rate versus net section stress for a temperature of 900 °C.	52
24	Log-log plot of indentation rate versus net section stress for a temperature of 750 °C.	53
25	Arrhenius plot of indentation rate versus inverse temperature for a net section stress of 183 MPa.	54
26	a) Scanning electron microscope image of an indent in a TiAl alloy sample. b) Schematic side view of the surface bulge and the gap	55

27	a) Scanning electron microscope image of an indent in a TiAl alloy sample showing a flow pattern in front of the indenter. b) Schematic drawing of the line pattern in front of the indenter.	56
28	Log-log plot of temperature compensated strain rate versus creep stress. . . .	57
29	Simple dislocation model describing the indentation process in an indentation creep test.	60

List of Tables

1	Compilation of hardness data and crystal orientation for olivine.	15
2	Compilation of hardness data for jadeite and diopside.	32
3	Crystal orientation of tested jadeite and diopside grains.	32
4	Results of hardness tests on omphacite.	33
5	Comparison of shear modulus, the Poisson ratio, magnitude of Burgers vector and lattice spacing of the slip plane for jadeite and diopside.	36
6	Compilation of the results obtained from indentation creep tests on a TiAl alloy.	49
7	Compilation of stress exponents and activation energies obtained from indentation creep tests and conventional tensile creep tests.	49

Abstract

The objective of this thesis is to explore the potential of high-temperature indentation techniques in experimental rock deformation. First, microindentation hardness tests using a pyramid-shaped indenter were performed on olivine and clinopyroxene grains within natural aggregates. Second, indentation creep experiments using a cylindrical indenter were employed to investigate the rheological behaviour of an engineering alloy used as an analogue material with well-known creep properties.

Microindentation hardness tests were performed on differently oriented olivine grains at temperatures between 25 °C and 900 °C. The hardness shows a strong dependence on crystal orientation, but depends only slightly on temperature. Investigation of the morphology of the indents revealed linear features in the surface surrounding the indents. These lineations are interpreted as slip lines. Their orientation with respect to the crystal orientation was used to infer $\{110\}[001]$ as the predominant slip system during indentation. For this slip system, a good correlation between hardness and resolved shear stress was found, if loading is assumed to be compression normal to the pyramid faces of the indent. Indentation hardness tests are proposed to be useful for the exploration of the low-temperature plasticity regime.

The hardness of members of the clinopyroxene solid solution series with end members jadeite and diopside was determined at temperatures ranging from 300 °C to 750 °C. Jadeite is found to be significantly stronger than diopside in the low-temperature plasticity regime. Normalization of hardness with respect to the shear modulus considerably reduces the strength contrast, indicating that jadeite and diopside belong to the same isomechanical group. Indentation hardness tests on omphacite with a near-intermediate composition revealed a considerable variability in strength, which is supposed to be related to variations in the degree of ordering, exsolution phenomena, or submicroscopic inclusions.

Indentation creep experiments were performed on a TiAl alloy at temperatures between 750 °C and 1050 °C and net section stresses between 50 MPa and 1430 MPa. This two-phase engineering material was used as a model material for a polyphase silicate aggregate. The stress and temperature dependence of the indentation rate is in good agreement with data obtained from uniaxial tensile testing on the same material. Investigation of the deformed volume in front of the indenter revealed a distinct line pattern reflecting material flow during indentation. Also, a simple dislocation model is proposed to explain volume and shape of the bulge that develops around the indent.

In summery, indentation hardness testing can provide information on the strength anisotropy of minerals, on the activated slip systems, and on the relative strength of minerals in the low-

temperature plasticity regime. The latter can be used to classify minerals into isomechanical groups. Indentation creep experiments can be applied to obtain creep parameters and to investigate flow patterns of non-coaxial deformation. The application of this indentation method to rock forming minerals appears to be promising.

1 Introduction

1.1 Objective and structure of the thesis

The objective of this thesis is to explore the potential of high-temperature indentation techniques in experimental rock deformation. First, microindentation hardness tests using a pyramid-shaped indenter were carried out on various minerals. Second, indentation creep tests with a cylindrical indenter were performed on an engineering alloy that was used as a model material with well specified creep properties to test this method, which shall be applied to a polycrystalline silicate aggregate in the future.

The introductory part of this thesis starts with a brief overview of the different approaches to study the rheological behaviour of rocks including experimental rock deformation, which is the subject of this work. The following section shows the problems that arise when information about the mechanical behaviour of rocks obtained from laboratory experiments is transferred to geological conditions. The final part of the introduction deals with various kinds of experimental techniques that are used to study the rheology of rocks at high temperatures.

The body of the thesis comprises three parts, that were originally written as research papers for publication. The first part "*Hardness anisotropy and slip systems of olivine investigated by high-temperature microindentation hardness test*" by Dorothee Dorner, Martin Schellewald and Bernhard Stöckhert is submitted for publication to *Tectonophysics*. It deals with the orientation dependence of the microhardness of olivine single crystals and uses the orientation of slip steps on the sample surface to infer slip systems. The second part "*An experimental study on the relative plastic strength of a clinopyroxene solid solution series using microindentation hardness tests*" by Dorothee Dorner and Bernhard Stöckhert is prepared for submission to *Tectonophysics*¹. In this paper, microindentation hardness tests on jadeite and diopside are used to analyse the relative strength of this clinopyroxene solid solution series. The third part "*Creep of a TiAl alloy: a comparison of indentation and tensile testing*" by Dorothee Dorner, Klaus Röller, Birgit Skrotzki, Bernhard Stöckhert and Gunther Eggeler is submitted to *Materials Science and Engineering A*². It compares the results of indentation creep experiments on a TiAl alloy with those from uniaxial creep tests on the same material.

Finally, the results of the indentation tests obtained for different materials using different

¹Published meanwhile with the title changed to *Plastic flow strength of jadeite and diopside investigated by microindentation hardness tests*, *Tectonophysics*, Vol. 379, pp. 229-240, 2004

²Published meanwhile: *Materials Science and Engineering A*, Vol. 357, pp. 346-354, 2003

techniques are summarized with regard to the potential that high-temperature indentation methods offer for the investigation of the rheology of rocks.

1.2 Approaches to rock rheology

Rheology is the branch of physics that deals with the deformation and flow of materials (Ranalli, 1987). Rock rheology studies analyse the response of geological materials to deviatoric stresses under various conditions. Modes of failure of rock are localized and ductile deformation, with the latter denoting distributed deformation (Rutter, 1986). Another way of describing rock rheology deals with the microphysical processes during flow. The deformation mechanisms can be classified into diffusive mass transport, intracrystalline plasticity and cataclasis (Rutter, 1986; Paterson, 1987). Parameters that influence the mechanical behaviour of rocks are temperature, pressure or - more precisely - mean stress, chemical environment, pore-fluid pressure and chemistry, microstructure, among others (e. g. Paterson, 1987; Evans and Kohlstedt, 1995). Deformation regimes denote ranges of temperature, flow stress, and strain rate, where different deformation mechanisms and accompanying processes dominate (Frost and Ashby, 1982; Schmid, 1982; Poirier, 1985). The deformation behaviour within a specified regime is described by a mechanical equation of state, commonly referred to as flow law. The deformation regimes, represented by their flow laws, are often visualized in deformation mechanism maps that can be used to predict the dominant deformation mechanisms and the mechanical properties for a specified temperature, flow stress or strain rate (Frost and Ashby, 1982; Poirier, 1985). At high stresses and high strain rates, but low temperatures, the low-temperature plasticity regime is relevant, where dislocation glide is the predominant mechanism, accompanied by mechanical twinning and cracking. At higher temperatures and lower stresses and strain rates, deformation takes place in the dislocation creep regime, where dislocation glide and climb are dominant, accompanied by recrystallization and recovery processes. At even lower stresses and strain rates, diffusive mass transfer becomes the controlling deformation mechanism in the diffusion creep regime. Diffusion can take place through the crystal volume at higher temperatures (Nabarro-Herring creep), along grain boundaries at lower temperatures (Coble creep), or through a fluid phase (dissolution-precipitation creep).

There are different but intimately related approaches to study rock rheology respectively tectonic processes (Carter and Tsenn, 1987; Paterson, 1987, 2001; Rutter, 1993; Handy *et al.*, 2001). Geological field studies reveal structures in natural rocks indicating deformation by plastic flow or fracture. These structures are evident from the microscopic to the global scale. Analysis of naturally deformed rocks yields information about the relative

strength of the various constituents of rocks as well as about the activated deformation mechanisms. Geological field studies reveal the deformation history of rocks, that are exhumed to the earth surface. In contrast, geophysical field studies detect structures that are related to present day tectonic processes in the interior of the earth at various scales. The knowledge gained from both geological and geophysical field studies is used in simulations of tectonic processes like faulting, folding, rifting, subduction, collision, earthquakes, and so on. Quantitative numerical modelling of geodynamic processes requires the knowledge of the mechanical properties of the various relevant rocks types (e.g. Handy *et al.*, 2001). Strength envelope diagrams (e.g. Kirby, 1980; Kohlstedt *et al.*, 1995), which allow quantitative predictions of the strength of the lithosphere, are also based on experimentally determined constitutive equations. Therefore, experimental rock deformation studies aim to derive such flow laws, that describe the mechanical behaviour of rocks under different physical conditions in terms of e.g. stress or temperature. Furthermore, the microstructures that develop during experimental deformation are analysed to identify the corresponding deformation mechanisms and to compare them with the record of natural rocks (e.g. Schmid, 1982; Stöckhert *et al.*, 1999a).

1.3 Applying laboratory rheological data to geological conditions

Various problems arise when the rheological behaviour of rocks is predicted by extrapolating experimentally derived constitutive equations to natural conditions (Paterson, 1987, 2001; Handy *et al.*, 2001). First of all, the time scale of laboratory experiments is short compared to that of natural plastic deformation of rocks. Therefore, the strain rates in rock deformation experiments are up to nine orders of magnitude higher than in nature. Deformation at higher strain rates and comparable stress levels is achieved by applying higher temperatures compared to natural conditions (Tullis and Tullis, 1986; Rutter, 1993). When laboratory data are extrapolated to lower temperatures and natural strain rates, it has to be guaranteed that the deformation regime is identical and the appropriate flow law can be applied. This is done by comparing the microstructures of naturally deformed rocks with those obtained in laboratory experiments (Schmid, 1982; Paterson, 2001; Handy *et al.*, 2001). Examining the microstructures of naturally deformed rocks, it has to be taken into account that these structures became frozen in at some time of the rock history. Thus, the observed microscopic structures possibly reflect the record of a sequence of deformation episodes in different deformation regimes (e.g. Stöckhert *et al.*, 1999a). Also, the deformation microstructures are possibly overprinted by static annealing during exhumation. In contrast, in rock deformation experiments the microstructures are quenched and can be

attributed to specified conditions of temperature, flow stress and strain rate.

It is commonly assumed that natural rocks deform at thermal, mechanical and structural steady state when tectonic processes are simulated (Paterson, 2001). However, it is questionable if there is steady state in natural rock deformation (Paterson, 1987). For example, transient creep can occur in natural rocks during stress relaxation after earthquakes (e.g. Trepmann and Stöckhert, 2001, 2002). Also, it is usually assumed that laboratory experiments take place under steady state conditions, and that the experimentally derived constitutive equations are valid for steady state deformation. However, large strain torsion experiments reveal that - strictly speaking - steady state is not reached until large strains are accumulated (Paterson and Olgaard, 2000; Paterson, 2001).

Natural and experimental rock deformation can differ in the stress and strain states (Paterson, 2001). In nature the stress state can be completely general, whereas in laboratory experiments, in most cases, cylindrical samples are subject to simple stress states (Tullis and Tullis, 1986; Paterson, 1987). In contrast, the stress state in torsion experiments and in indentation experiments is more complex. Similarly the strain in natural deformed rocks can be completely general, whereas the strain state in rock deformation experiments is often simple. Also, the magnitude of strain that can be reached in the laboratory experiments is usually less than that in naturally deformed rocks (Paterson, 2001).

Further problems arise in the application of laboratory data to the simulation of tectonic processes because of the different spatial scales involved in laboratory experiments and in nature. The results obtained from small laboratory specimens have to be applied to the large scale of geological formations, which includes extrapolation over several orders of magnitude. Doing this, it has to be taken into account that large natural rock masses can include large-scale petrological or structural heterogeneities, which possibly determine the rheological behaviour of the whole rock mass.

Laboratory experiments are often performed on monomineralic rock samples to enable the understanding of elementary deformation mechanisms, which requires the analysis of simple systems. Also, deformation experiments on polyphase rocks are often complicated by chemical reactions at the high test temperatures (Evans and Kohlstedt, 1995). Thus, the rheologies for polyphase aggregates have to be calculated using measured rheologies of the constituent phases (Tullis *et al.*, 1991; Ji and Zhao, 1993, 1994). However, polyphase materials can deform by other mechanisms than monophase materials. For instance, the presence of phase boundaries between different minerals appears to be prerequisite for effective deformation by dissolution-precipitation creep (e.g. Schwarz and Stöckhert, 1996; Stöckhert, 2002).

1.4 Experimental rock deformation techniques

This section presents rock deformation techniques used to investigate the plastic deformation behaviour of rocks at high temperatures and, in most cases, simultaneously at high confining pressures. As already pointed out, temperatures in rock deformation experiments have to be high to attain high strain rates. Additionally, laboratory deformation experiments are often performed at high pressures not only to reproduce the conditions within the earth but to suppress brittle failure of rock samples (Tullis and Tullis, 1986; Rutter, 1993). Also, high pressures are required for the investigation of the mechanical behaviour of minerals that are thermodynamically unstable at low pressures (e.g. Stöckhert and Renner, 1998).

1.4.1 Apparatus used in uniaxial, triaxial, and torsion deformation experiments

Rock deformation experiments at temperatures of up to 1500 °C and particularly at high confining pressures up to 3.5 GPa can be performed in a *Griggs-type solid medium apparatus* (Tullis and Tullis, 1986). In this type of deformation apparatus a weak solid is used as the pressure transmitting medium. Using a solid pressure transmitting medium causes substantial friction between the moving parts during a deformation experiment resulting in a low stress resolution. As an alternative to a weak solid, a solid can be used that is molten under experimental conditions of temperature and pressure, and thus increases the stress resolution of the deformation apparatus substantially (Green and Borch, 1989; Rybacki *et al.*, 1998).

Instead of a solid confining medium, a gas is used in a *gas medium deformation apparatus*, which provides a better stress resolution compared to a solid medium apparatus (Paterson, 1970; Tullis and Tullis, 1986; Evans and Kohlstedt, 1995). Since the pressure chamber is difficult to seal and more care has to be taken concerning security equipment, the confining pressures are restricted to less than 700 MPa at temperatures of up to 1400 °C. Recently, gas medium apparatus were upgraded in the way that torsion experiment are possible (e.g. Paterson and Olgaard, 2000). This enables to explore the effect of large strains on the rheological behaviour of rocks (e.g. Bystricky *et al.*, 2000; Mauler *et al.*, 2000)

In both solid and gas medium deformation apparatus, the load is commonly applied using a servohydraulically driven piston. This allows constant strain rate testing as well as creep tests at constant load. In contrast, in a *1-atmosphere creep rig* or *dead-load creep apparatus* (e.g. Mackwell *et al.*, 1990a; Wang *et al.*, 1996a,b; Dimanov *et al.*, 1998) the load is applied by placing "dead" weights on top of the piston. It is operated at atmospheric pressure and

at temperatures of up to 1600 °C. Additionally, the oxygen fugacity of the atmosphere is often controlled. Oxygen fugacity is one controlling factor of the point defect concentration, which in turn influences the rheological behaviour of minerals (e.g. Poumellec and Jaoul, 1984; Ricoult and Kohlstedt, 1985; Karato, 1989; Mackwell *et al.*, 1990b; Bai *et al.*, 1991). Dead-load creep apparatus are simple to operate and used for long term creep experiments.

1.4.2 Indentation hardness tests and indentation creep tests

Two types of indentation techniques are explored in this thesis. The first approach is microindentation hardness tests on minerals. Indentation hardness tests are very common in materials science engineering to characterize the strength of solids (e.g. Standard DIN50133, 1985; Tabor, 1951; Blumenauer, 1994), since they are simple and little effort is required for sample preparation. Microindentation hardness tests are suitable to investigate the local deformation behaviour of materials, e.g. of thin films or particles in composites. For studies on the rheological behaviour of rocks this means that microindentation hardness tests can be performed on selected millimeter-sized grains within natural polyphase rocks. Scratch hardness tests are well known in geosciences from the Mohs hardness scale. Indentation hardness tests are also applied in geosciences, primarily for the identification of ore minerals. Moreover, some studies exist that investigate the mechanical behaviour of silicates using indentation hardness tests (Brace, 1960, 1963, 1964; Evans and Goetze, 1979; Evans, 1984; Darot *et al.*, 1985; Karato *et al.*, 1995a). In indentation hardness tests, an indenter that is harder than the material to be tested is pressed vertically into the sample material. A corresponding hardness number is usually obtained by dividing the applied force by the size of the indent. The exact definition of the hardness number is dependent on the indenter geometry. A widespread indenter geometry, which is also used in this work, is a square-based pyramid called Vickers indenter. The corresponding Vickers hardness H is defined as the applied force F divided by the area A of the generated indent: $H=F/A$. Other common indenter geometries are spheres (Brinell hardness), cones (Rockwell hardness) and rhombus-based pyramids (Knoop hardness). Generally, a hardness test comprises the following steps: (1) loading of the indenter until a specified maximum load is reached, (2) keeping the maximum load for a specified time period of usually 10 s, and (3) unloading the sample. For this type of deformation experiment, it is not straightforward to relate the deformation to a specified flow stress and strain rate. In fact, the corresponding stress and strain fields are very complex in space and time (Tabor, 1951, 1970, 1986; Chiang *et al.*, 1982; Samuels, 1986).

The second indentation technique that is dealt with in this work is indentation creep testing

using a cylindrical indenter. Such creep tests are used in materials science engineering to study the local mechanical behaviour of materials (Li, 2002). Compared to other indenter geometries, indentation testing with cylindrical indenters can provide steady-state results and is simpler in analysis and simulation (Li, 2002). In geosciences, one study exists that uses this test geometry to analyse the development of preferred orientations in non-coaxial deformation (Kunze and Avé Lallemant, 1981). However, so far indentation creep testing has not been employed to investigate the mechanical behaviour of rocks and to derive flow law parameters. On part of this thesis investigates the indentation creep behaviour of an engineering alloy with a complex microstructure and well-defined flow properties. The material serves as a model material for a polyphase silicate aggregates, which will be studied in a next step.

2 Hardness anisotropy and slip systems of olivine investigated by high-temperature microindentation hardness tests

2.1 Abstract

High-temperature microindentation hardness tests have been performed at temperatures between 25 °C and 900 °C on differently oriented olivine grains within a natural peridotite. The hardness shows a strong dependence on crystal orientation, but depends only slightly on temperature. From the orientation of slip lines around the indents, $\{110\}[001]$ was inferred as the predominant slip system in the indentation process. For this slip system, Schmid and Brookes factors were calculated to correlate the hardness with the resolved shear stress on the activated slip system. A good correlation was found, if loading is assumed to be compression normal to the pyramid faces of the indent. Indentation hardness tests are proposed to be useful for the exploration of low-temperature plasticity.

2.2 Introduction

High-temperature microindentation hardness studies on minerals are rare (Westbrook, 1957; Evans and Goetze, 1979; Evans, 1984; Darot *et al.*, 1985; Kollenberg, 1986; Karato *et al.*, 1995b). However, microindentation techniques offer some advantages compared to other rock deformation methods: (1) deformation experiments can be performed on natural rock specimens with small grain size; (2) sample preparation is simple; and (3) a significant number of experiments can be done within a short period of time. Indentation hardness tests are particularly useful for comparative studies of the strength of minerals. For example, variations of hardness with composition, chemical environment or temperature might be studied. Since microindentation tests are performed on single crystals, hardness anisotropy needs to be considered before the relative strength of minerals can be compared.

This study explores the effect of crystal orientation and temperature on the indentation hardness. The morphology of the indents revealing slip lines allows slip systems activated in the indentation process to be derived. This information in turn is used to correlate the hardness data with the resolved shear stress on the activated slip system. Olivine was chosen as the sample material, because it is well studied owing to its importance for the rheology of the upper mantle, hence allowing the comparison of results obtained in various studies.

2.3 Method and material

2.3.1 Definition of hardness

The hardness of a solid is usually understood as its resistance to local deformation (Tabor, 1970, 1986). For a square-based diamond pyramid indenter, referred to as Vickers indenter, a quantitative value of the hardness H is defined as the force F applied on the specimen divided by the pyramidal area A of the indent (e.g. Tabor, 1970):

$$H = \frac{F}{A}.$$

For the Vickers indenter the angle between opposite faces of the pyramid is 136° . Thus, the hardness can be given as

$$H = 1.854 \cdot \frac{F}{d^2},$$

with d denoting the diagonal diameter of the indent. In this study the mean length of the two indent diagonals is used to determine the hardness.

2.3.2 Apparatus

The microindentation apparatus used (Fig. 1) allows indentation tests to be performed at temperatures of up to 900°C in a vacuum of 10^{-3} mbar (Lührig, 1993; Berns and Lührig, 1994). The specimen is fixed on an xy-stage, which can be positioned alternatively under a microscope or under a loading system. Loading is done with a piezo-translator that drives a Vickers indenter in 10 nm steps into the sample surface. A load cell measures the applied load. The specimen and the indenter are independently heated with radiation heaters made from tantalum foils (Fig. 2). The temperatures are measured with two PtRh-Pt thermocouples, one of which is welded to the indenter near the diamond pyramid and the other to the sample holder next to the specimen.

2.3.3 Sample preparation, experimental procedure and analytical methods

Natural peridotite slabs with a thickness of about $200\ \mu\text{m}$, which is about 100 times the indentation depth, were polished mechanically and chemically with colloidal silica. This choice of sample thickness is a compromise to make sure that the indents are not affected by the lower sample surface, while the samples remain transparent to light to enable examination by optical microscopy. Specimens with a diameter of 6 mm were diamond-cored from these slabs.

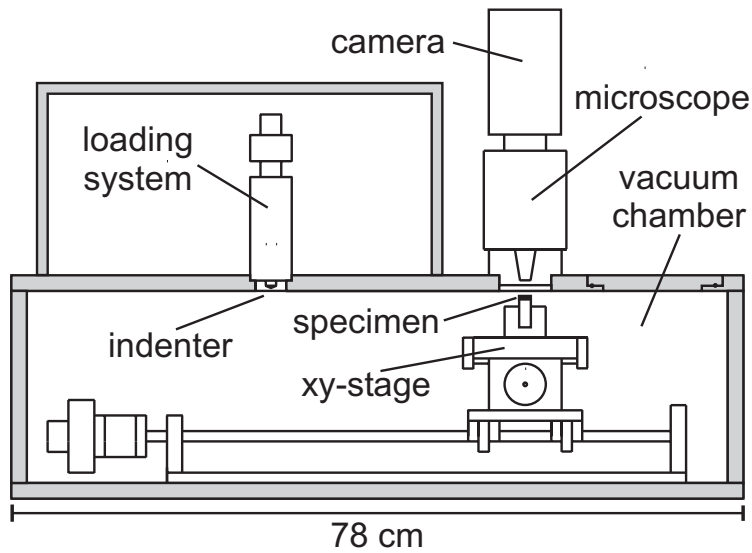


Figure 1: Scheme of the high-temperature microindentation apparatus.

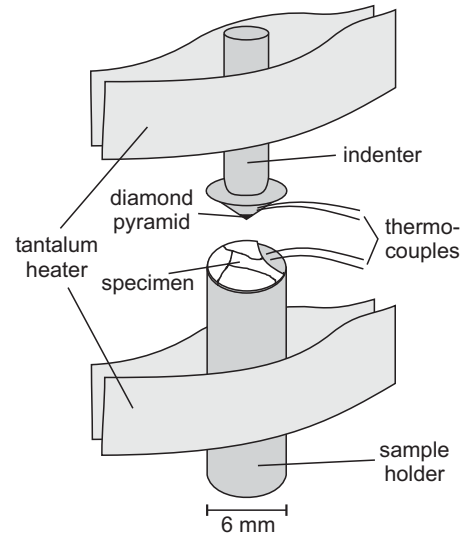


Figure 2: Scheme of the sample assembly.

Specimen and indenter are simultaneously heated to the same temperature. The spots to be analysed are first selected with the microscope. Then the specimen is positioned under the loading system. The specimen is loaded with a constant displacement rate of $0.6 \mu\text{ms}^{-1}$ to a force of 0.5 N. A period of 10 s at constant load follows. The unloading is done with the same displacement rate as the loading. About 30 indents are generated in a single grain at the specified conditions. The distance between the individual indents is at least three times the indent diagonal length ($10\text{--}15 \mu\text{m}$). The same distance is kept from grain boundaries, microfractures, and other discontinuities.

Besides the applied force, the lengths of the diagonals of the indents need to be determined to calculate the hardness. A scanning electron microscope (SEM) is used to measure these lengths and to study the morphology of the indents. The crystal orientation is determined by electron backscatter diffraction (EBSD; Prior *et al.*, 1999).

2.3.4 Sample material

Microindentation hardness tests were performed on selected olivine grains of a mantle peridotite from the Finero complex, Ivrea zone, Western Alps (e.g. Duyster and Stöckhert, 2001). The peridotite contains 85 % olivine, 10 % orthopyroxene and up to 5 % of phlogopite and opaque minerals. The grain size of the olivine is in the order of a millimeter. The chemical composition of the olivine is $\text{Mg}_{1.8}\text{Fe}_{0.2}\text{SiO}_4$ determined by energy dispersive x-ray analysis (EDAX).

The type and concentration of water-related defects in the olivine crystals used for the

indentation tests were investigated by Fourier-Transform-Infrared spectroscopy (FTIR) at room temperature. The IR-microscope attached to a Bruker Spectrometer IFS 48 provides a spatial resolution of about $100\ \mu\text{m}$ for the $200\ \mu\text{m}$ thick polished slabs; the limit of detection is about $0.005\ \text{mole H/l}$ for broadband absorption (e.g. Aines and Rossman, 1984; Paterson, 1982). The spot analysis revealed that water and water-related defects are inhomogeneously distributed. Within the limits of spatial resolution, significant concentrations of water and water-related defects appear to be restricted to grain boundaries and microcracks, while the concentrations remain below the limit of detection in the interior of the clear olivine crystals (Fig. 3, spectrum a). In regions of higher concentration, two broad absorption bands are centered at about $3685\ \text{cm}^{-1}$ and $3650\ \text{cm}^{-1}$ (Fig. 3, spectra b and c). These bands are characteristic of serpentine (Miller *et al.*, 1987), which presumably has formed as an alteration product of olivine along microcracks and grain boundaries. The indentation tests were carried out in the interior of clear crystals. Thus, the effect of water and water-related defects (Mei and Kohlstedt, 2000a,b; Bai *et al.*, 1997; Mackwell *et al.*, 1985) on the indentation hardness of olivine cannot be quantified since potential variations in the water content are below the detection limit.

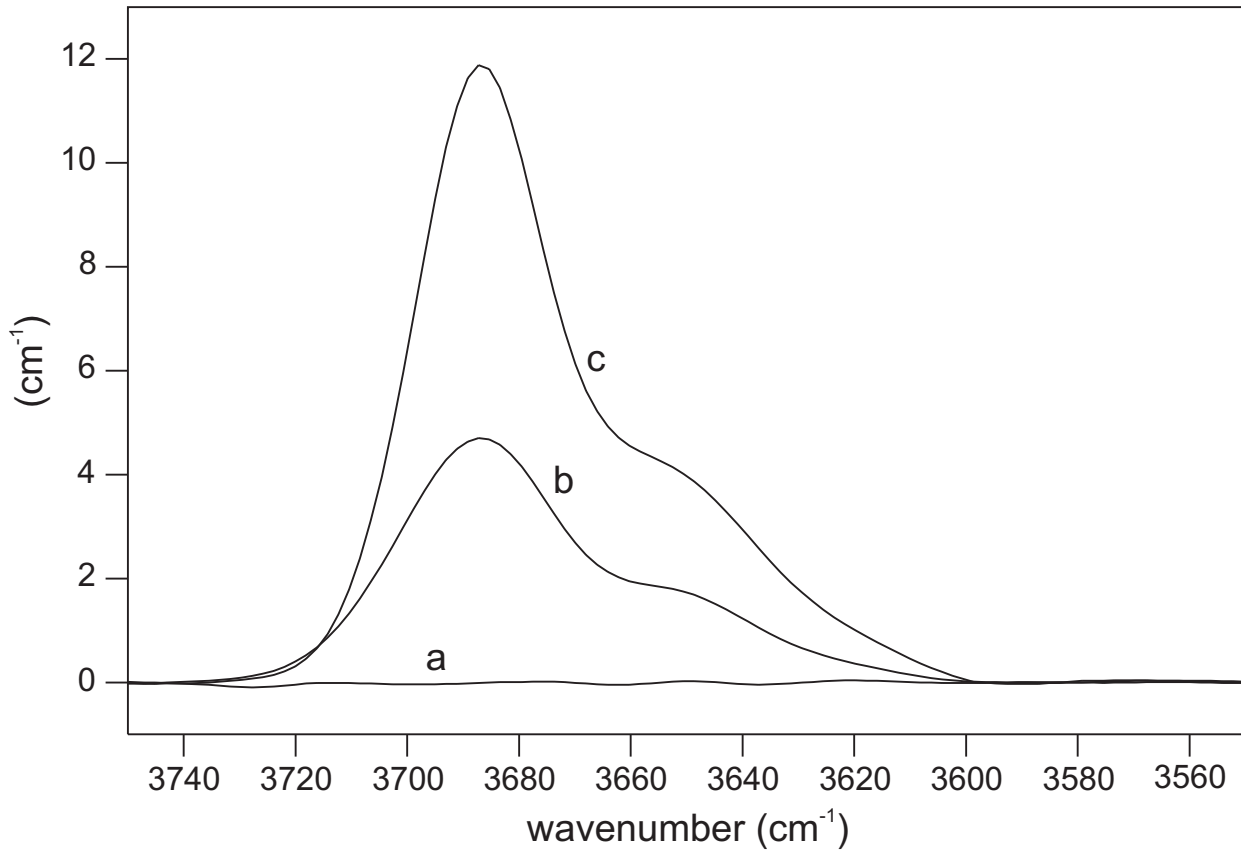


Figure 3: Room temperature FTIR spectra for olivine used for the microindentation tests. The spectra a, b and c are for different spots in the same crystals showing the variation in type and concentration of water-related defects.

2.4 Results

2.4.1 Mechanical data

Microindentation hardness tests were performed at various temperatures between room temperature and 900 °C on twelve olivine crystals with different orientations (Fig. 4; Tab. 1). The tested crystal orientations were selected by chance in contrast to studies on oriented single crystals (Evans and Goetze, 1979; Darot *et al.*, 1985; Karato *et al.*, 1995b). Additionally, some tests were performed with different indenter orientations on the same crystal. The quoted hardness data represent the means obtained from about 25 indents generated at each specified set of conditions.

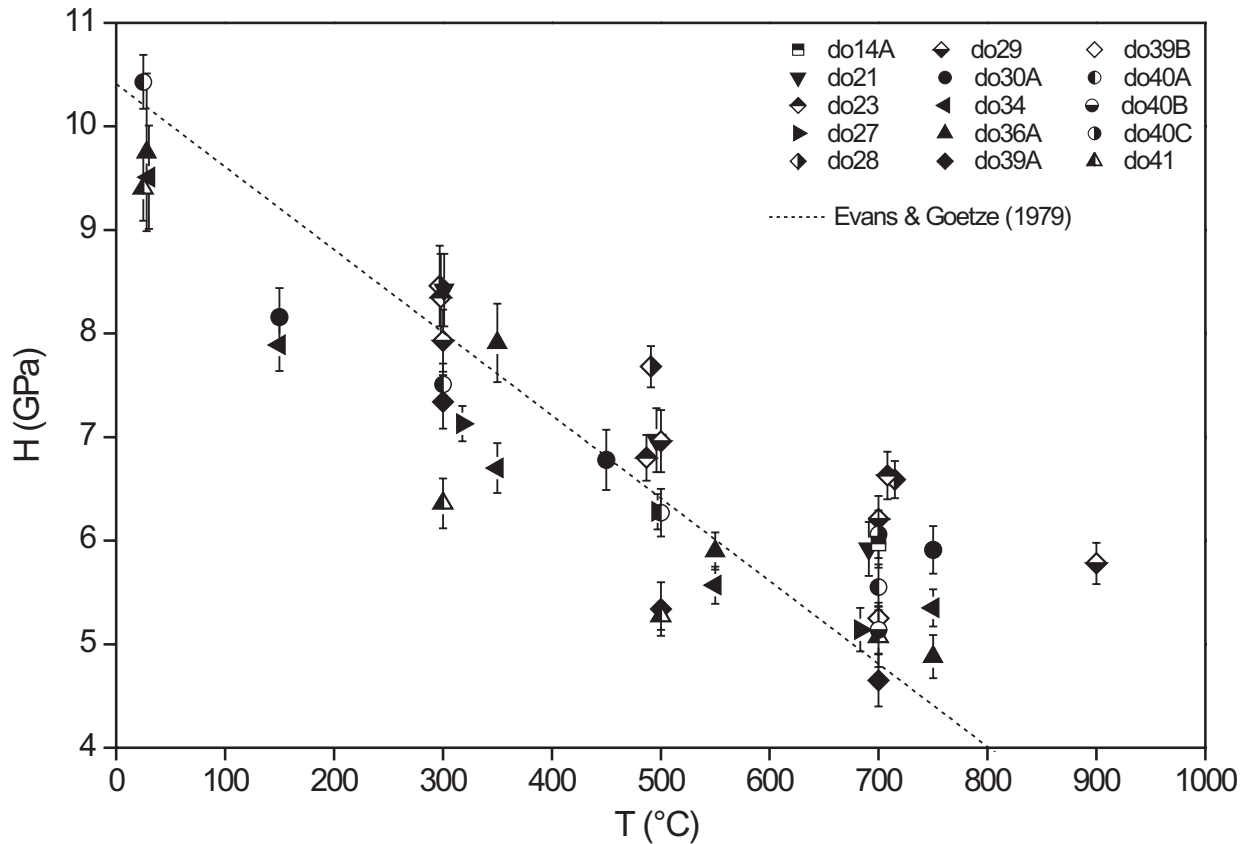


Figure 4: Hardness of olivine as a function of temperature. The experiments were performed on crystals with different orientations (Tab. 1). Capital letters added to the sample number indicate experiments with the same crystal orientation but with the indenter rotated. If the hardness values are nearly identical, only orientation A is displayed. A linear fit of data from Evans and Goetze (1979) is included for comparison.

In the investigated temperature range of 25 °C to 750 °C, corresponding to homologous temperatures of 0.14 to 0.47, the measured hardness ranges from 4.7 GPa to 10.4 GPa (Fig. 4, Tab. 1). For a given orientation, the hardness shows a moderate dependence on temperature

Table 1: Compilation of hardness data and crystal orientation. Hardness data are the means and standard deviations of about 25 individual measurements. The crystal orientation is given as the azimuth and dip of [100], [010], [001] respectively with respect to the indent diagonals. The azimuth is ambiguous, because of the fourfold symmetry axis of the indent. Crystal orientations of Evans and Goetze (1979) and Phakey et al. (1972) are also included (*: values not given).

experiment	temperature (°C)	hardness (GPa)	[100]		[010]		[001]	
			azimuth	dip	azimuth	dip	azimuth	dip
do14A	700	6.0 ± 0.2	125	59	340	26	243	15
do14B	700	6.1 ± 0.2	157	"	12	"	275	"
do14C	700	6.1 ± 0.3	189	"	44	"	306	"
do14D	700	6.1 ± 0.3	218	"	74	"	336	"
do21	301	8.4 ± 0.4	137	54	295	34	32	11
	496	7.0 ± 0.3	"	"	"	"	"	"
	691	5.9 ± 0.3	"	"	"	"	"	"
do23	298	8.4 ± 0.4	13	87	144	2	234	2
	487	6.8 ± 0.2	"	"	"	"	"	"
	708	6.6 ± 0.2	"	"	"	"	"	"
do27	318	7.1 ± 0.2	7	13	102	21	247	65
	497	6.3 ± 0.2	"	"	"	"	"	"
	683	5.1 ± 0.2	"	"	"	"	"	"
do28	297	8.5 ± 0.4	120	20	289	70	28	4
	491	7.7 ± 0.2	"	"	"	"	"	"
	715	6.6 ± 0.2	"	"	"	"	"	"
do29	300	7.9 ± 0.3	142	8	248	63	49	26
	500	7.0 ± 0.3	"	"	"	"	"	"
	700	6.2 ± 0.2	"	"	"	"	"	"
	900	5.8 ± 0.2	"	"	"	"	"	"
do30A	150	8.2 ± 0.3	216	69	345	13	78	16
	450	6.8 ± 0.3	"	"	"	"	"	"
	750	5.9 ± 0.2	"	"	"	"	"	"
do30B	450	7.0 ± 0.3	169	"	297	"	31	"
	750	5.9 ± 0.2	"	"	"	"	"	"
do34	30	9.5 ± 0.5	217	31	109	27	347	46
	150	7.9 ± 0.3	"	"	"	"	"	"
	350	6.7 ± 0.2	"	"	"	"	"	"
	550	5.6 ± 0.2	"	"	"	"	"	"
	750	5.4 ± 0.2	"	"	"	"	"	"
do36A	28	9.8 ± 0.8	185	59	47	24	309	19
	350	7.9 ± 0.4	"	"	"	"	"	"
	550	5.9 ± 0.2	"	"	"	"	"	"
	750	4.9 ± 0.2	"	"	"	"	"	"
do36B	750	5.1 ± 0.3	50	"	272	"	174	"
do39A	300	7.3 ± 0.3	136	14	39	27	251	59
	500	5.3 ± 0.3	"	"	"	"	"	"
	700	4.7 ± 0.3	"	"	"	"	"	"
do39B	700	5.3 ± 0.2	185	"	88	"	300	"
do40A	25	10.4 ± 0.3	168	15	66	39	275	47
	300	7.5 ± 0.2	"	"	"	"	"	"
	500	6.3 ± 0.2	"	"	"	"	"	"
	700	5.6 ± 0.2	"	"	"	"	"	"
do40B	700	5.1 ± 0.2	153	"	51	"	260	"
do40C	700	6.1 ± 0.2	111	"	9	"	218	"
do41	25	9.4 ± 0.3	149	33	241	3	336	57
	300	6.4 ± 0.2	"	"	"	"	"	"
	500	5.3 ± 0.1	"	"	"	"	"	"
	700	5.1 ± 0.3	"	"	"	"	"	"
Evans			*	45	*	45	*	0
Phakey, orientation A			*	45	*	45	*	45
Phakey, orientation B			*	45	*	45	*	0

(Fig. 5). It decreases by only about 5 MPaK^{-1} with increasing temperature. The hardness obtained at the same temperature but for different crystal orientations differs by up to

45% indicating a strong dependence on crystal orientation (Fig. 4, Tab.1). Rotation of the indenter for the crystal orientations do39 and do40 resulted in hardness variations of up to 20% (Fig.6, Tab.1). For other crystal orientations we observed no variation (do14, do30, do36; Fig.6, Tab.1). Thus, the indenter orientation has an influence on hardness only for certain crystal orientations.

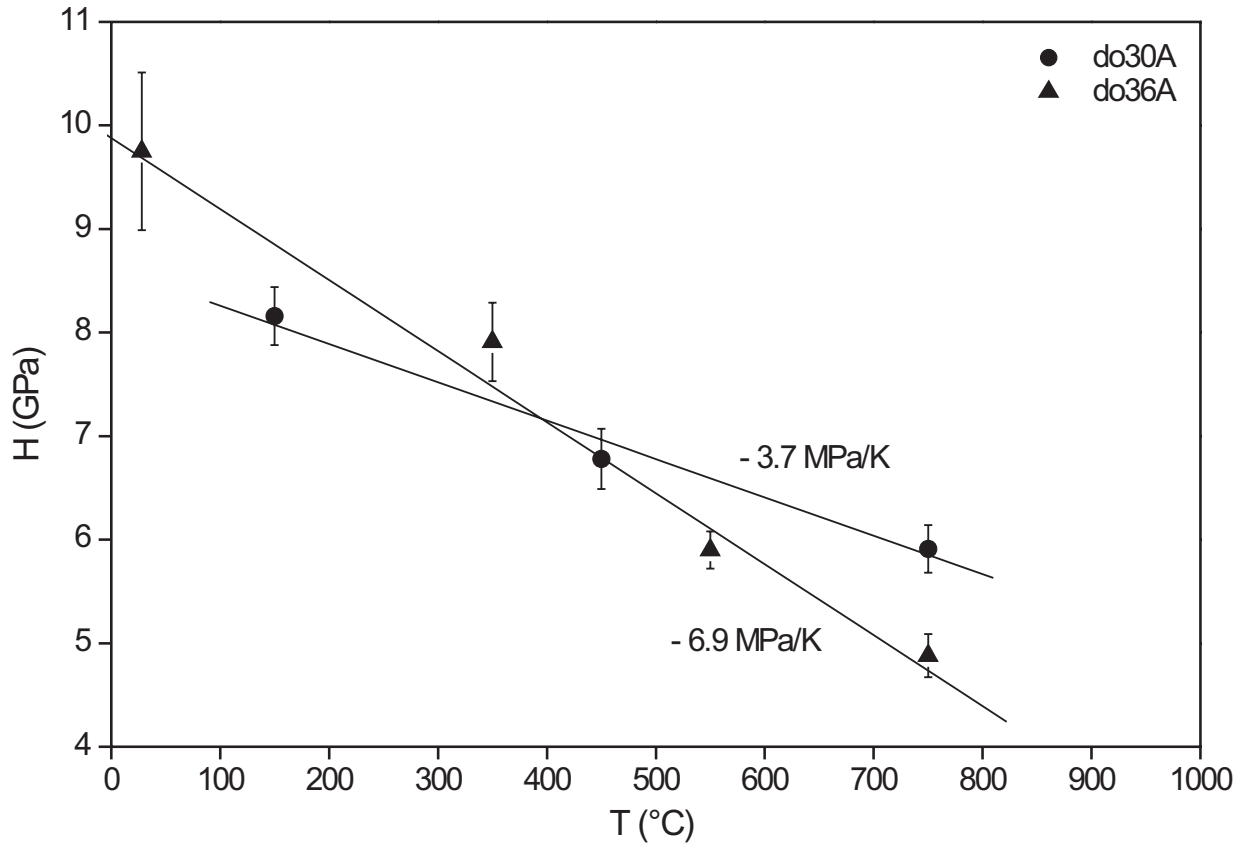


Figure 5: Hardness versus temperature for two different samples. The temperature dependence of the hardness is moderate with about -5 MPaK^{-1} .

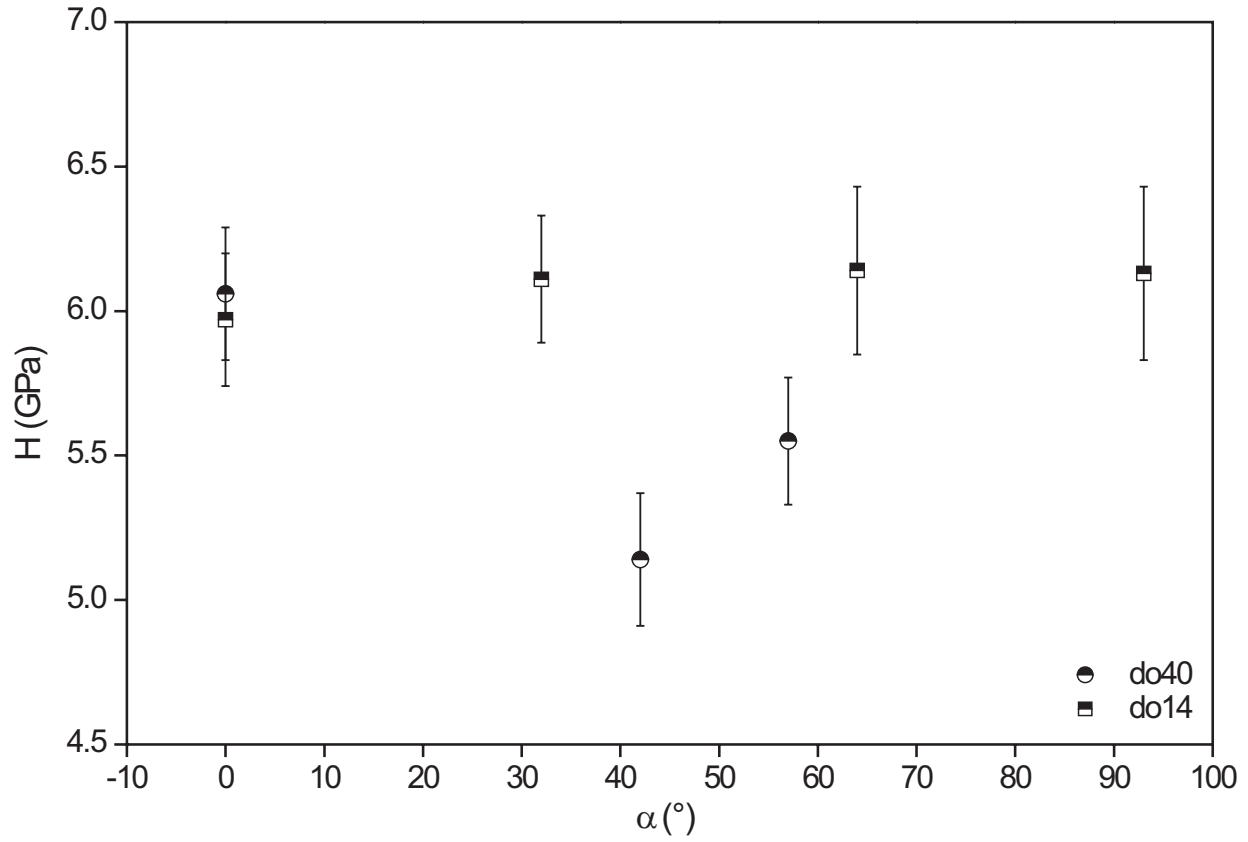


Figure 6: Hardness versus indenter orientation for two different crystal orientations. The angle between the direction of the indent diagonal and the [100] direction is labeled α . Only for some crystal orientations the hardness depends on the indenter orientation.

2.4.2 Morphology of indents

Cracks are visible around most of the indents (Fig. 7). The involved crack energy can be estimated by assuming the generation of two half-penny shaped cracks (Marshall and Lawn, 1986) with a diagonal length of about 30-40 μm . With a specific fracture surface energy for olivine of approximately 1 Jm^{-2} (Swain and Atkinson, 1978) the crack energy is about 1 nJ. From recorded force-displacement curves, the inelastic energy of the indentation process is determined to be about 300 nJ. Thus, the fraction of the inelastic energy used for the crack generation is negligible and therefore crack generation is not considered in detail in this study.

In nine of the twelve tested samples, sets of parallel linear features are visible on the surface around the indents (Fig. 7a). Their occurrence and geometry were found to be dependent on the crystal orientation (Figs. 7b, 7c), but independent on the indenter orientation (Figs. 7d, 7e). These lineations are interpreted as slip lines, reflecting the slip systems activated during the indentation process. Slip lines are steps on a surface generated by localization of dislocation glide on certain crystal planes, provided that the slip direction is inclined to the surface (Fig. 8). Slip lines in minerals around indents were also observed by Brace (1963) and Kollenberg (1988).

The orientation of the slip lines on the sample surface, representing the traces of the slip plane, were measured on crystals with various orientations to derive the activated slip plane. Displaying these orientations with respect to the crystal orientation unambiguously reveals $\{110\}$ as the predominant slip plane (Fig. 9). The corresponding slip direction cannot be directly identified by this method. However, all data points clearly lying on the trace of $\{110\}$ include angles $>20^\circ$ with the $[001]$ direction. Since slip lines require that the slip direction is inclined to the sample surface, we suggest $[001]$ as the corresponding slip direction. The length of the Burgers vector in this direction is 4.8 \AA , and low compared to other possible slip directions in the $\{110\}$ slip plane. Thus, $\{110\}[001]$ is proposed as the predominant slip system activated in the indentation process. This slip system was also identified by optical microscopy (Raleigh, 1968; Carter and Avé Lallemant, 1970) and by transmission electron microscopy (Phakey *et al.*, 1972). Other slip planes cannot be identified (Fig. 9), although some of the data points may be consistent with $\{0kl\}$ pencil glide or the (100) slip plane, which were both considered as possible in olivine by Poirier (1975) and also observed in the studies cited above. Some data points could also be consistent with the $\{310\}$ slip plane, but this is not a likely slip plane (Poirier, 1975).

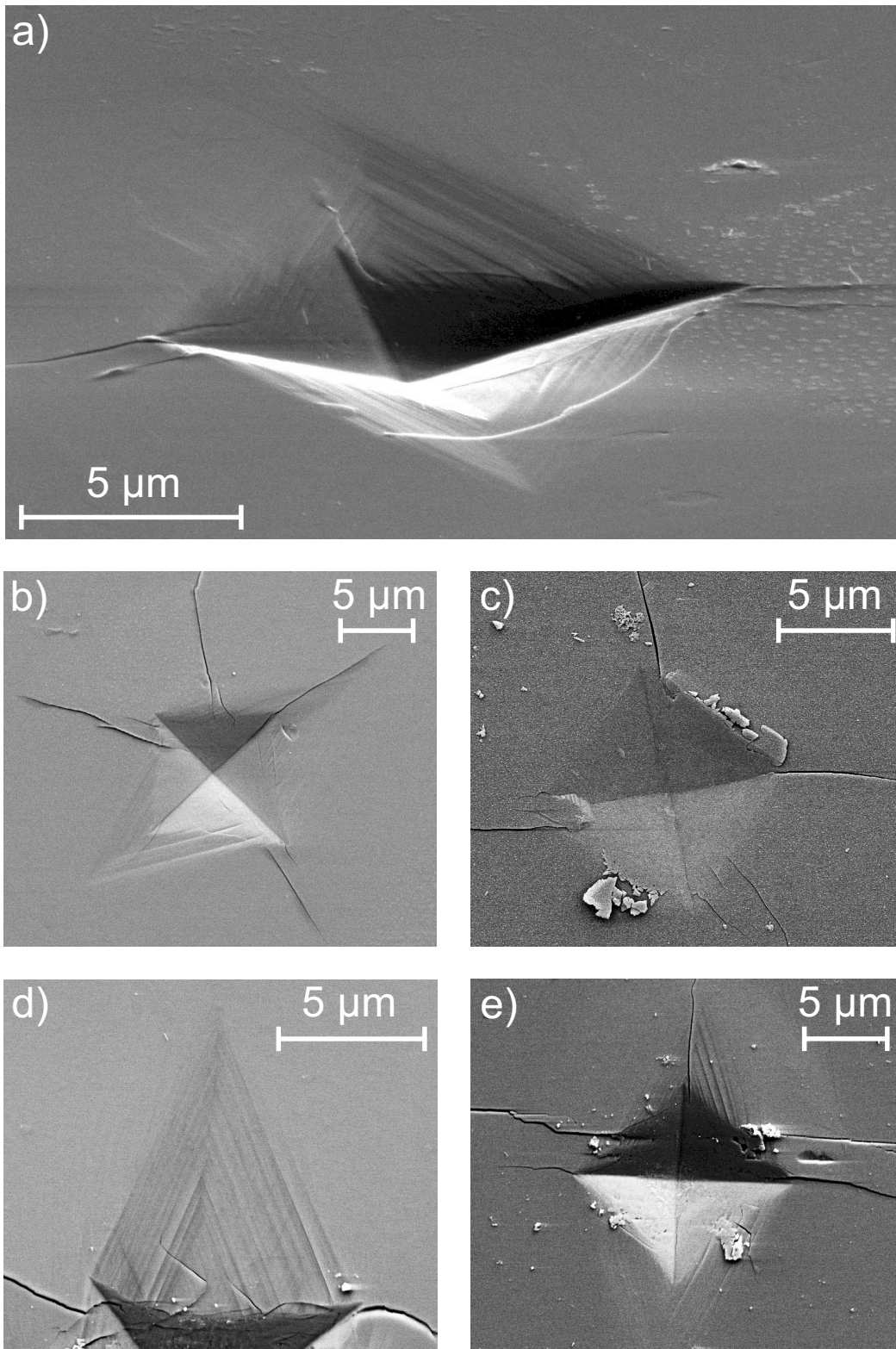


Figure 7: SEM images of indents in olivine crystals with slip lines and cracks. The occurrence of the slip lines is dependent on crystal orientation (Figs. 7b, 7c). The orientation of the slip lines is not influenced by indenter orientation (Figs. 7d, 7e). a) Oblique view (do27, 700 °C). Slip lines and cracks. b) Crystal orientation with slip lines (do27, 700 °C). c) Crystal orientation without slip lines (do23, 700 °C). d) Slip lines (do39A, 700 °C). e) Crystal orientation identical to that in Fig. 7d (do39B, 700 °C), but with the indenter rotated by approximately 45°.

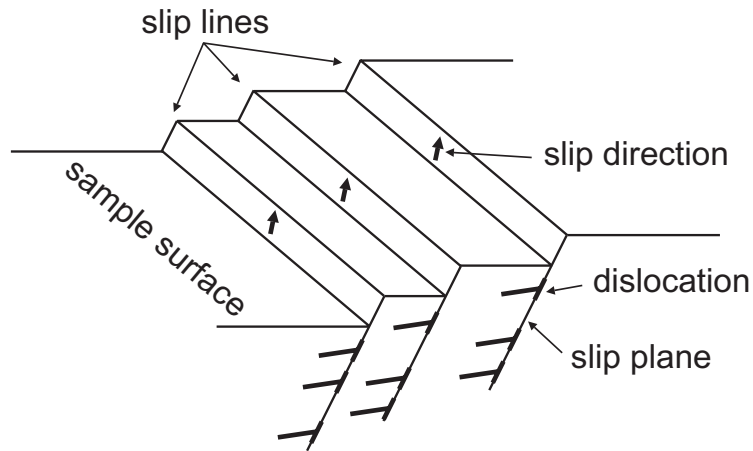


Figure 8: Scheme of slip lines. Glide of dislocations on slip planes in the slip direction can produce steps on the sample surface provided that the slip direction is inclined to the sample surface. These steps can be visible at the sample surface as linear features.

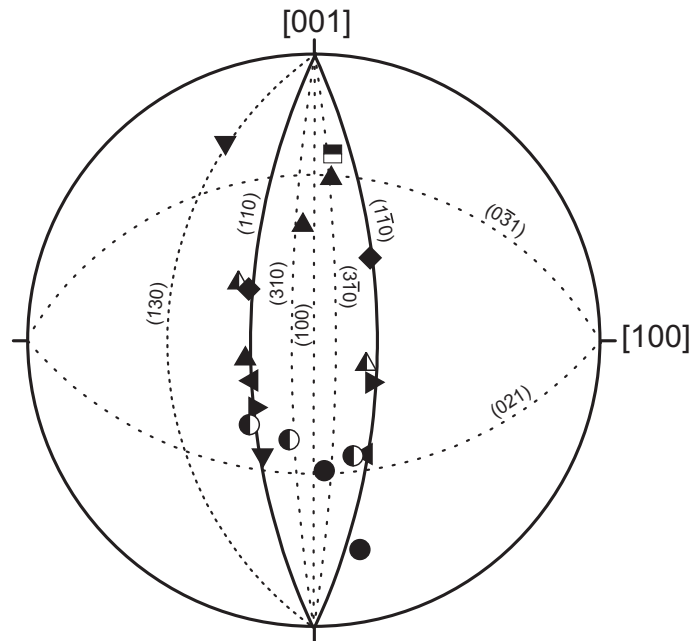


Figure 9: Orientation of slip lines and corresponding slip planes with respect to the crystal orientation. Compilation from all experiments where slip lines are visible. For definition of symbols refer to Fig. 10. Stereographic projection: lower hemisphere, equal angle.

2.5 Discussion

2.5.1 Hardness anisotropy

The orientation dependence of the indentation hardness of olivine was analysed using three different models. Models A and B are based on the Schmid equation (Schmid and Boas, 1950)

$$\tau = \frac{F}{A} \cos \lambda \cos \phi ,$$

with τ denoting the resolved shear stress, F the force applied on the area A , λ the angle between the loading direction and the slip direction, and ϕ the angle between the loading direction and the normal to the slip plane. Brookes *et al.* (1971) extended the Schmid equation taking into account constraints concerning the rotation of slip planes. They stated that the ‘effective resolved shear stress’ τ_e on a slip system is a minimum if the axis of rotation of a slip plane is normal to an indent facet and a maximum if this axis is parallel to the facet. Model C is based on their ‘effective resolved shear stress equation’

$$\tau_e = \frac{1}{2} \cdot \frac{F}{A} \cdot \cos \lambda \cos \phi (\cos \psi + \sin \gamma) ,$$

with ψ denoting the angle between the indent facet and the axis of rotation of the slip plane, and γ the angle between the indent facet and the slip direction. For each model the hardness was correlated with a factor that gives the fraction of the applied stress that is effective on the slip plane in the direction of slip. For models A and B, this is the Schmid factor $S = \cos \lambda \cos \phi$, whereas for model C it is $B = \frac{1}{2} \cdot \cos \lambda \cos \phi (\cos \psi + \sin \gamma)$, here named Brookes factor analogous to the Schmid factor. These factors were calculated for the $\{110\}[001]$ slip system identified earlier by the analysis of the slip lines. Furthermore, for the determination of the Schmid and the Brookes factor the loading direction has to be defined. As a first approximation, Model A assumes the direction of loading to be normal to the sample surface. This assumption does not take into account the indenter geometry and the orientation of the pyramid faces of the Vickers indenter, and therefore cannot explain variations in hardness with the rotation of the indenter. Thus, Schmid factors for model B and Brookes factors for model C were calculated assuming that loading is compression normal to the pyramid faces of the indent. Additionally, loading being tension parallel to the pyramid faces as proposed by Brookes *et al.* (1971) was also considered. For model A, we obtain two Schmid factors, because $\{110\}$ comprises two individual slip planes. In this case, the hardness is correlated with the higher of the two Schmid factors. This seems reasonable, because if slip starts on the slip plane with the higher resolved shear stress, the resolved stress on the other slip plane cannot increase and the value of the Schmid factor for this plane is no longer important. For models B and C, eight individual Schmid and

Brookes factors respectively are determined as the four pyramid faces of an indent give four different loading directions in addition to the two slip planes. In this case, a mean Schmid or Brookes factor is obtained by: (1) determining the two factors for each of the pyramid faces, (2) selecting the higher of the two values for each face as in the case of model A, and (3) calculating the mean of these four factors.

All three models yield similar results (Fig.10). The hardness decreases with increasing Schmid or Brookes factor with the best correlation at temperatures of 300 °C to 350 °C. A high factor means a high resolved shear stress on the considered slip plane in the slip direction. Thus, the crystal is in an easy slip orientation and the obtained hardness is low. The good correlation of hardness and Schmid or Brookes factor supports $\{110\}[001]$ as the predominant slip system, as derived from the orientation of the slip lines. The fact that the correlation of hardness and Schmid or Brookes factor becomes worse at higher temperatures indicates that at temperatures of about 700 °C the slip system $\{110\}[001]$ may no longer predominate, and that other slip systems might become activated. Activation of other slip systems at higher temperatures is reported in other studies (Raleigh, 1968; Carter and Avé Lallemand, 1970; Phakey *et al.*, 1972), although not below 1000 °C. These high-temperature slip systems include $\{0kl\}[100]$, $(010)[100]$ and $(001)[100]$.

For the simple model A, assuming loading normal to the sample surface, the correlation between hardness and Schmid factor is nearly as good as for models B and C. Thus, this assumption provides a good approximation to the real load distribution, although it neglects the indenter geometry and orientation. This is considered as reasonable in view of the small angle of 22° between the sample surface and the indenter facets.

Models B and C both seem equally suitable to explain the dependence of hardness on crystal orientation. The additional constraint of model C does not improve the quality of the correlation of hardness and Schmid or Brookes factor. If the experiments with variable indenter orientation (do14, do30, do36, do39, do40) are compared, model B reflects the variations in hardness slightly better than model C. These experiments were performed at higher temperatures, however, where the correlation of hardness with the Schmid or Brookes factor for $\{110\}[001]$ slip becomes worse and other slip systems might become important.

The assumption of loading being tension parallel to the pyramid faces yields neither a correlation for hardness with the Schmid factor nor the Brookes factor. Thus, we conclude that in our experiments hardness anisotropy cannot be explained assuming that the effective loading direction is tension parallel to the pyramid faces.

2.5.2 Deformation regime

Low-temperature plasticity is the deformation regime accessible with indentation hardness test. This is evident from estimates on yield stress and strain rate, and from the temperature dependence of the hardness.

For a rigid-plastic material, the uniaxial yield stress σ_y in compression is related to the hardness H as

$$H = C \sigma_y ,$$

where C is a constraint factor with a value of about 3 (e.g. Tabor, 1970, 1986). Johnson (1970) derived a formula relating hardness and yield stress considering an elastic-plastic material that is indented by a cone. For a Poisson ratio of 0.25 it is

$$H = \frac{2}{3} \left[1 + \ln \left(\frac{2}{9} \frac{E}{\sigma_y} \tan \beta + \frac{4}{9} \right) \right] \sigma_y ,$$

where E is the Young's modulus and β the angle between the sample surface and the indenter facet. This relation is also used for a Vickers pyramid indenter with $\beta = 19.7^\circ$, which is the angle of a cone which replaces the same volume as the Vickers pyramid (Johnson, 1970). Assuming $E = 170$ GPa for olivine, this relation gives yield stresses of 2.6 GPa to 9.7 GPa for the measured hardness values of 4.7 GPa to 10.4 GPa.

For materials that work-harden during indentation, the hardness-derived yield stress corresponds to an effective strain of 0.08 to 0.10 (Tabor, 1970, 1986). With this strain and considering that the time scale of the indentation process is 10 s, a very high strain rate on the order of 10^{-2} s^{-1} is obtained.

The only moderate temperature dependence of the hardness indicates that thermally activated processes like diffusion are not important in the indentation process. The high hardness-derived yield stresses combined with the high strain rate lead to the conclusion that low-temperature plasticity is the deformation regime accessible with indentation hardness tests. This assumption is supported by the occurrence of slip lines indicative of glide-controlled deformation.

The microstructural record of natural rocks indicates that deformation in the low-temperature plasticity regime is widespread in the upper crust (e.g. McLaren and Hobbs, 1972; Groshong, 1988; Blenkinsop and Drury, 1988; Lloyd and Knipe, 1992; Stöckhert *et al.*, 1999b; Lloyd, 2000). It can also be important in the uppermost plastosphere (Scholz, 1990), where synseismic loading during major earthquakes at the lower termination of crustal fault zones causes very high stress magnitudes and short term plastic deformation at high strain

rates (Küster and Stöckhert, 1999; Trepmann and Stöckhert, 2001, 2002). Recently, the low-temperature plasticity regime was considered in studies modelling the formation of shear zones (Kameyama *et al.*, 1999) or the deformation of subducting slabs (Karato *et al.*, 2001).

2.5.3 Comparison with other studies

High-temperature hardness data for olivine from Evans and Goetze (1979) are included in Fig. 4. They are generally consistent with the results of this study. The crystal orientation tested by Evans and Goetze (1979) resembles mostly our orientations do21, do23 and do28 (Tab. 1). If the data are compared considering these crystal orientations, we find a good agreement at about 300 °C. At about 700 °C the hardness values of Evans and Goetze (1979) are lower than those obtained in our tests. Evans and Goetze (1979) applied a constant load for 15 s, compared to 10 s in our study. This allows more time for creep deformation, which possibly yields larger indents and thus a lower hardness. Since creep is effective at higher temperatures, this could explain why the discrepancy is restricted to these conditions.

We also compared our hardness data to mechanical data that were obtained by Phakey *et al.* (1972) in triaxial deformation experiments performed on cylindrical samples of olivine single crystals. At 800 °C, they observed a significant effect of orientation on flow stress. Their strongest crystal orientation B is similar to our strong orientations do21, do23 and do28, and their weakest orientation A is close to our weak orientation do41 (Tab. 1). The good correlation of the results obtained in indentation hardness tests and in uniaxial or triaxial deformation experiments on cylindrical samples outlines the potential of indentation hardness tests for the acquisition of mechanical data.

2.6 Conclusions

High-temperature microindentation hardness tests on olivine grains within a natural peridotite show that:

- (1) Microindentation hardness of olivine depends strongly on crystal orientation.
- (2) Hardness of olivine depends only moderately on temperature at homologous temperatures between 0.14 and 0.47. The hardness-derived yield stresses and the corresponding strain rate are very high. This confirms that indentation hardness tests access the low-temperature plasticity regime.
- (3) Slip lines are observed on the surface around the indents. The analysis of their orientation allows the determination of the activated slip plane. $\{110\}[001]$ was inferred as the predominant slip system at low temperatures, while other slip systems might become

activated at temperatures above 700 °C.

(4) Schmid and Brookes factors, which relate the shear stress resolved on the slip system to the applied load, were determined for three models, taking $\{110\}[001]$ as the activated slip system. Models assuming the loading direction to be compression normal to the pyramid faces and normal to the sample surface respectively reveal a good correlation between hardness and Schmid or Brookes factor. In contrast, no correlation is obtained if loading is assumed to be tension parallel to the pyramid faces.

(5) In general, microindentation hardness tests on rock-forming minerals can provide information on the activation of slip systems as a function of temperature and on the strength of minerals in the low-temperature plasticity regime. The small required sample size and the use of natural inhomogeneous and polyphase material render this method a powerful tool to compare the strength of different mineral phases and to explore the influence of composition on strength.

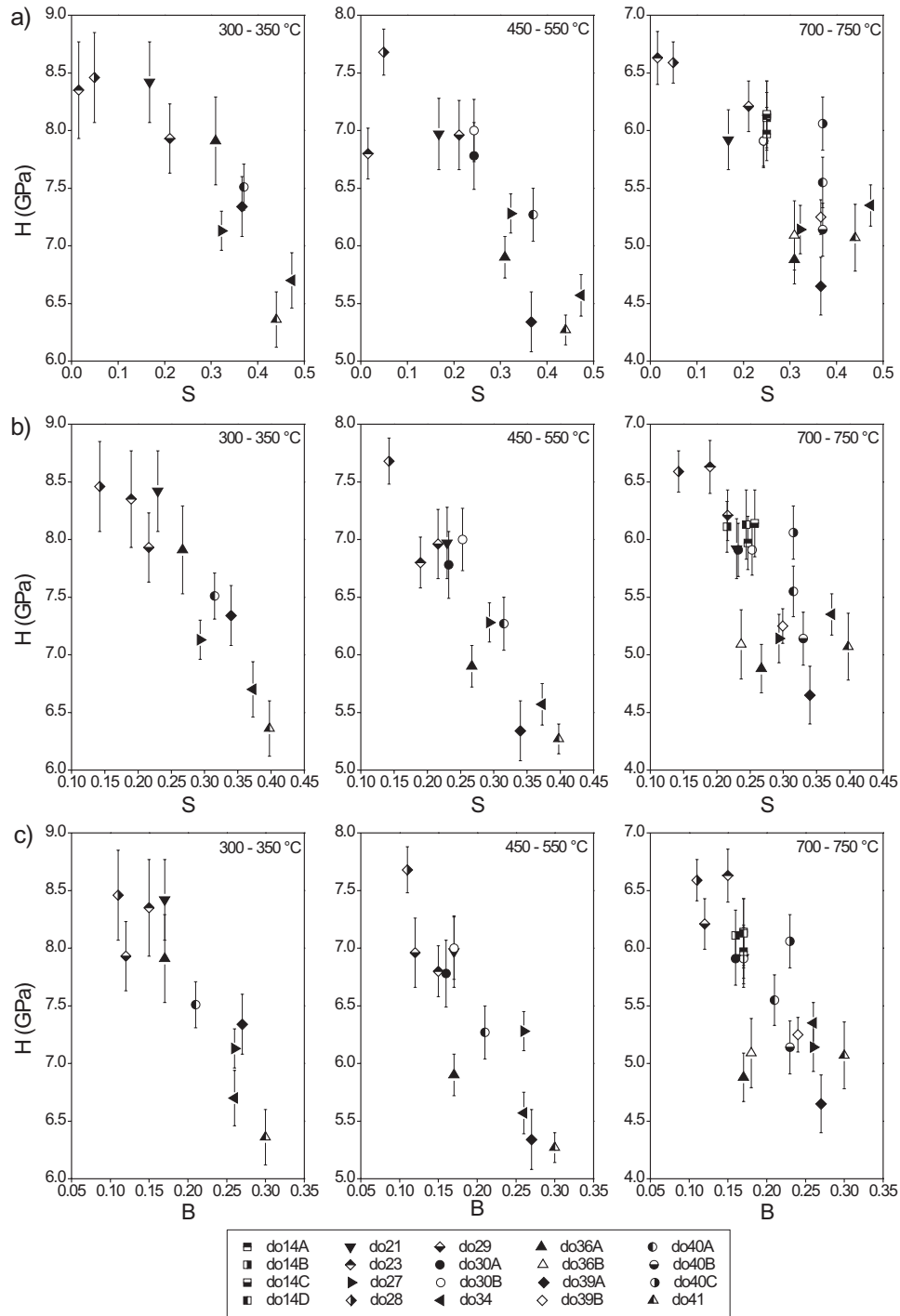


Figure 10: Hardness as a function of Schmid or Brookes factor for three different models, and three temperature ranges each. a) Model A: Correlation of hardness H and Schmid factor S according to the Schmid equation. The loading direction is assumed to be normal to the sample surface. Schmid factors were calculated for the $\{110\}[001]$ slip system. In each case the higher of the two factors is displayed. b) Model B: Correlation of hardness H and Schmid factor S according to the Schmid equation. The loading direction is assumed to be normal to each of the pyramid faces of the indent. Schmid factors were calculated for the $\{110\}[001]$ slip system. For each of the four pyramid faces the higher of the two Schmid factors was selected. The mean of these four values is shown in the diagrams. c) Model C: Like model B, except that Brookes factors B were calculated according to the effective resolved shear stress equation (cf. text).

3 An experimental study on the relative plastic strength of a clinopyroxene solid solution series using microindentation hardness tests

3.1 Abstract

Microindentation hardness tests were performed on the clinopyroxene end members jadeite and diopside as well as on omphacite solid solutions. At temperatures between 300 °C and 750 °C the hardness of jadeite ranges from 7.4 GPa to 8.5 GPa, that of diopside from 4.9 GPa to 6.1 GPa. This reveals that jadeite is significantly stronger in the low-temperature plasticity regime than diopside. Normalization of the hardness data with respect to the shear modulus considerably reduces the strength contrast, indicating that jadeite and diopside belong to the same isomechanical group. For omphacite, a considerable variability in strength is observed, which may be related to variations in the degree of ordering, exsolution phenomena, or submicroscopic inclusions.

3.2 Introduction

The principle advantages of indentation hardness tests in experimental rock deformation (Brace, 1960, 1963, 1964; Evans and Goetze, 1979; Evans, 1984; Darot *et al.*, 1985; Karato *et al.*, 1995a) are that the samples can be very small and that preparation is simple compared to conventional uniaxial or triaxial deformation experiments. Microindentation hardness tests can thus be performed on selected millimeter-sized grains within natural polyphase rocks or on fine-grained aggregates. This opens a wide field of potential applications. For instance, the relation between strength and crystallographic orientation of the individual crystal can be explored, including analysis of the activated glide systems (Dorner *et al.*, in review). More important, indentation tests can be used to study the rheology of minerals which are difficult to synthesize and which are not available as natural monophase rocks with appropriate purity and grain size to be used in conventional rock deformation experiments. This is particularly true for solid solution series, where the mechanical properties may be a strong function of composition, as anticipated for important rock-forming minerals as feldspars, pyroxenes, and amphiboles.

In the present study we use high-temperature microindentation hardness tests to explore the relative strength of members of a clinopyroxene solid solution series as a function of composition. First, the hardness of the end members jadeite $\text{NaAlSi}_2\text{O}_6$ and diopside $\text{CaMgSi}_2\text{O}_6$

is determined. Then, the hardness of omphacite crystals with an intermediate composition near $\text{Na}_{0.5}\text{Ca}_{0.5}\text{Al}_{0.5}\text{Mg}_{0.5}\text{Si}_2\text{O}_6$ along the solid solution series is investigated. Insight into the mechanical properties of this sodic clinopyroxene solid solution series is important, as omphacite controls the strength and flow properties of subducted oceanic crust once transformed to eclogite, and the strength of the uppermost layer of the subducted lithosphere provides an upper bound to interplate shear stress (e. g. Piepenbreier and Stöckhert, 2001).

3.3 Definition of hardness

Qualitatively, hardness means the resistance of a solid to local deformation (Tabor, 1970, 1986). In indentation hardness tests an indenter, that is harder than the material to be tested, is pressed vertically into the sample material. A quantitative measure of the hardness H is then obtained by dividing the force F acting on the indenter by a characteristic area A :

$$H = \frac{F}{A} . \quad (1)$$

Thus the dimension of the hardness (Pascal) is that of a normalized force as that of pressure or stress. For a square-based diamond pyramid indenter with an angle of 136° between the opposite pyramid faces the area A is taken as the contact area between indenter and sample. For this Vickers geometry, using the indent diagonal d , the hardness number is defined by

$$H = 1.854 \cdot \frac{F}{d^2} . \quad (2)$$

3.4 Apparatus and experimental procedure

The apparatus used for the high-temperature microindentation hardness tests of the present study was described by Lührig (1993) and Berns and Lührig (1994). The sample chamber can be evacuated to a pressure of about 0.1 Pa. The specimen is fixed on an xy-stage, which can be alternatively positioned under a microscope or under the loading column (Fig. 11a). Both specimen and indenter are independently heated with tantalum foil radiation heaters (Fig. 11b). Two PtRh-Pt thermocouples are used to measure the temperature of the specimen respectively the indenter. One thermocouple is welded to the indenter near the diamond pyramid, the other is welded to the sample holder next to the specimen (Fig. 11b). The temperature is controlled to within ± 1 °C. Since the sample holder has a high thermal conductivity and the samples are only about $200 \mu\text{m}$ thick, thermal gradients are assumed to be negligible. Therefore, the inaccuracy of the temperature that results from measuring the sample temperature on the sample holder is supposed to be small. The load is applied with

a piezo-translator that drives a diamond Vickers indenter in steps of 10 nm into the sample surface. The load is measured with a load cell that is part of the loading column.

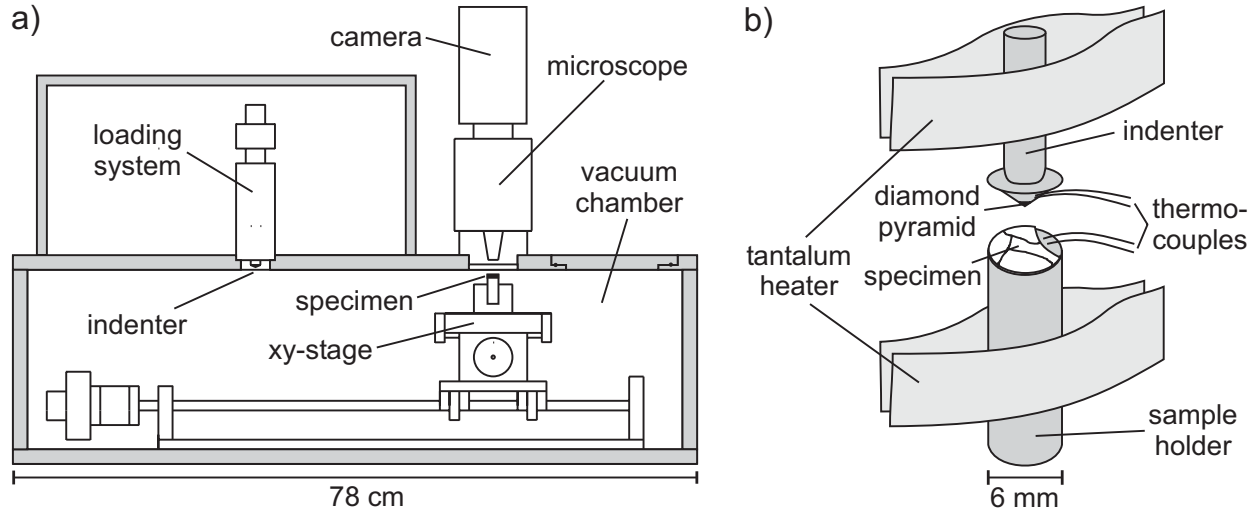


Figure 11: a) High-temperature microindentation apparatus. b) Sample assembly.

At the beginning of each experiment both specimen and indenter are heated to the same temperature. After selecting the spots to be used for the indentation test under the microscope, the specimen is automatically positioned under the loading system. The indenter is advanced with a constant velocity of $0.6 \mu\text{ms}^{-1}$ until being loaded with a force of 0.5 N. Then, the load is held constant for a period of 10 s. The specimen is unloaded using the same indenter velocity as for the loading. About 30 indents are generated in a single grain at the specified test conditions. The distance between the individual indents is at least three times their diagonal diameter of about $10 \mu\text{m}$ to $13 \mu\text{m}$. The same minimum distance is kept from grain boundaries, microfractures, and other discontinuities. A scanning electron microscope (SEM; Leo 1530 Gemini, operated at 5 kV) is used to measure the diagonal diameter and to study the morphology of the indents. The crystallographic orientation of the tested crystals is determined by electron backscatter diffraction (EBSD; Prior *et al.*, 1999).

3.5 Sample material

The indentation hardness tests were performed on selected jadeite, diopside, and omphacite grains within natural aggregates. For jadeite, a jadeite-quartzite from Parigi, Dora Maira Massif, Western Alps with number 19471 of the Mineralogical Collection of the Ruhr-University Bochum (MCRUB) was used. The chemical composition of this jadeite is $\text{Na}_{0.9}\text{Ca}_{0.1}\text{Al}_{0.9}\text{Fe}_{0.1}\text{Si}_2\text{O}_6$ as determined by energy dispersive X-ray analysis. For diopside, a calcsilicate fels specimen (22174, MCRUB) collected in a quarry 10 km north-east from Garies, Namaqua Land, South Africa, was used. The chemical composition of

the diopside is $\text{Ca}_{1.0}\text{Mg}_{0.7}\text{Al}_{0.1}\text{Fe}_{0.2}\text{Si}_2\text{O}_6$. Two different omphacites were used, referred to as omphacite I and II. Omphacite I is from an eclogite of Cabo Ortegal, north-west Spain (18083, MCRUB). Omphacite II is from an eclogite of the Sesia zone, Western Alps (ST29, collection of B.S.). The chemical composition of omphacite I and II are both near $\text{Na}_{0.5}\text{Ca}_{0.5}\text{Al}_{0.4}\text{Mg}_{0.4}\text{Fe}_{0.2}\text{Si}_2\text{O}_6$, with slight inhomogeneities. The grain size of all tested minerals is about 1 mm to 3 mm.

Slabs with a thickness of about 200 μm , which is about 100 times the indentation depth, were polished mechanically and chemically with colloidal silica. The thickness of the slabs is a compromise to make sure that the indents are not affected by the lower sample surface, while the samples remain translucent to enable examination by optical microscopy. Disc-shaped samples with a diameter of 6 mm were diamond-cored from these slabs.

3.6 Results

3.6.1 Indentation hardness of jadeite and diopside

The microindentation hardness tests were performed at temperatures T between 300 °C and 750 °C (Fig. 12, Tab. 2). For jadeite with a melting temperature T_m of 1100 °C at a pressure of 0.1 MPa (Bell, 1964) these temperatures correspond to homologous temperatures T/T_m of 0.42 to 0.75. For diopside with a melting temperature of 1392 °C at 0.1 MPa (Williams and Kennedy, 1969) the test temperatures correspond to homologous temperatures of 0.34 to 0.61. The quoted hardness data represent the mean and the standard deviation obtained from about 25 single indents generated at identical test conditions and within the same grain. Three jadeite and three diopside crystals with different and mutually corresponding orientations (Tab. 3) were tested. For jadeite the determined hardness ranges from 7.4 GPa to 8.5 GPa, for diopside from 4.9 GPa to 6.1 GPa. Thus, the hardness of jadeite is found to be 33% to 48% higher than that of diopside for a given temperature and a similar crystal orientation. Both the jadeite and the diopside hardness data depend only weakly on temperature with a gradient of $dH/dT = -2 \text{ MPa/K}$. Also, the variation of hardness with crystal orientation is mostly within the experimental errors.

3.6.2 Hardness tests on omphacite

In order to analyse if an intermediate chemical composition yields also an intermediate strength, we also performed microindentation hardness tests on two different omphacites (labeled I and II), both with a near intermediate composition. All hardness data fall inbe-

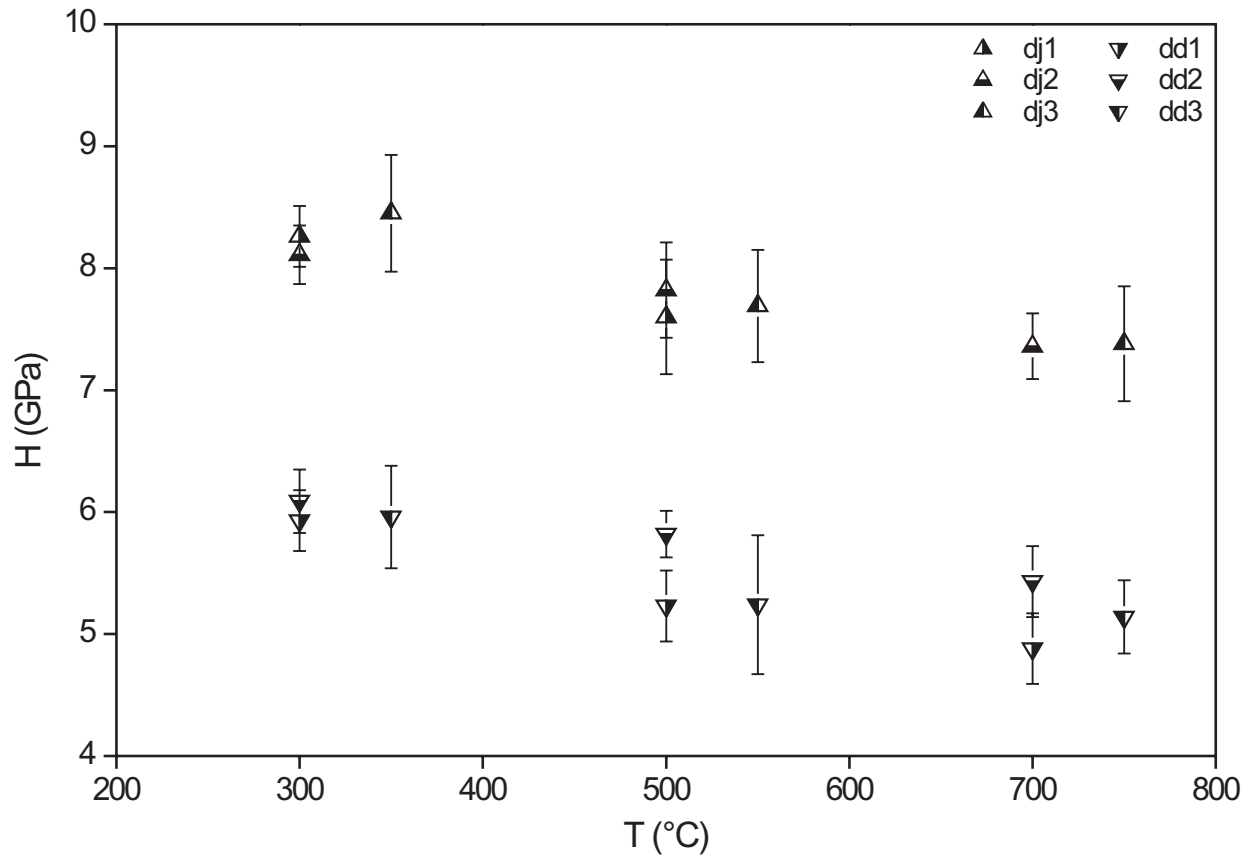


Figure 12: Hardness H of jadeite (Samples dj1, dj2, dj3) and diopside (Samples dd1, dd2, dd3) as a function of temperature T . The tests were performed on three differently oriented jadeite respectively diopside crystals with corresponding jadeite and diopside orientations (Tab. 3). Experiments with similar crystal orientations are indicated by symbols that are filled in the same part (right, lower, left).

tween the bonds given by the results on jadeite and diopside, but show a high and apparently unsystematic variability. At temperatures between 300 °C and about 500 °C, the hardness obtained for omphacite I (Samples dp8 and dp9) is comparable to that of jadeite (Fig. 13, Tab. 4). The determined hardness varies from 8.0 GPa to 8.8 GPa. In the same temperature range, the hardness data of omphacite II (Samples dp2, dp10, dp11, dp12) reveal a great variability. These hardness values cover the whole range between the hardness data for jadeite and diopside ranging from 5.2 GPa to 7.6 GPa (Fig. 13, Tab. 4). Thus, omphacite II yields a lower hardness than omphacite I. The hardness of omphacite II shows no systematic dependence on temperature or crystal orientation. For example, in one case at 300 °C two samples (dp10 and dp12) have a comparable hardness, whereas at 500 °C these two samples show a great difference in hardness with one (dp10) being comparable to that of jadeite and the other one (dp12) to that of diopside. In contrast, the hardness of two other samples (dp11 and dp12) differ at 300 °C, whereas they show a comparable hardness at 500 °C.

Table 2: Compilation of hardness data for jadeite (Samples dj1, dj2, dj3) and diopside (Samples dd1, dd2, dd3). The given hardness data are the mean and the standard deviation of about 25 individual measurements at the same tests conditions and within the same grain.

Sample	Temperature (°C)	Hardness (GPa)
dj1	300	8.3 ± 0.3
	500	7.6 ± 0.5
dj2	300	8.1 ± 0.2
	500	7.8 ± 0.4
	700	7.4 ± 0.3
dj3	350	8.5 ± 0.5
	550	7.7 ± 0.5
	750	7.4 ± 0.5
dd1	300	5.9 ± 0.3
	500	5.2 ± 0.3
	700	4.9 ± 0.3
dd2	300	6.1 ± 0.3
	500	5.8 ± 0.2
	700	5.4 ± 0.3
dd3	350	6.0 ± 0.4
	550	5.2 ± 0.6
	750	5.1 ± 0.3

Table 3: Crystal orientation of tested jadeite and diopside grains. The crystal orientation is given as the azimuth and the dip of [100], [010], and [001], respectively, with respect to the indent diagonals. The azimuth is ambiguous, because of the fourfold symmetry axis of the indent.

Sample	[100]		[010]		[001]	
	Azimuth	Dip	Azimuth	Dip	Azimuth	Dip
dj1	84	46	176	2	269	62
dj2	73	79	195	6	104	8
dj3	20	8	137	74	306	16
dd1	44	30	136	4	243	75
dd2	72	67	164	1	254	7
dd3	67	2	164	75	320	14

All omphacite samples were tested at 700 °C, but mechanical data could only be obtained for Samples dp2 and dp10. For all samples, examination of the 700 °C indents with an SEM reveals that the sample material is partly torn out, which is not observed for indents generated at lower temperatures (Fig. 14). For Samples dp2 and dp10 this phenomenon is not that pronounced, thus their indent diagonal were measured. This was not the case for the other samples, where the torn-out material could be found sticking on the indenter.

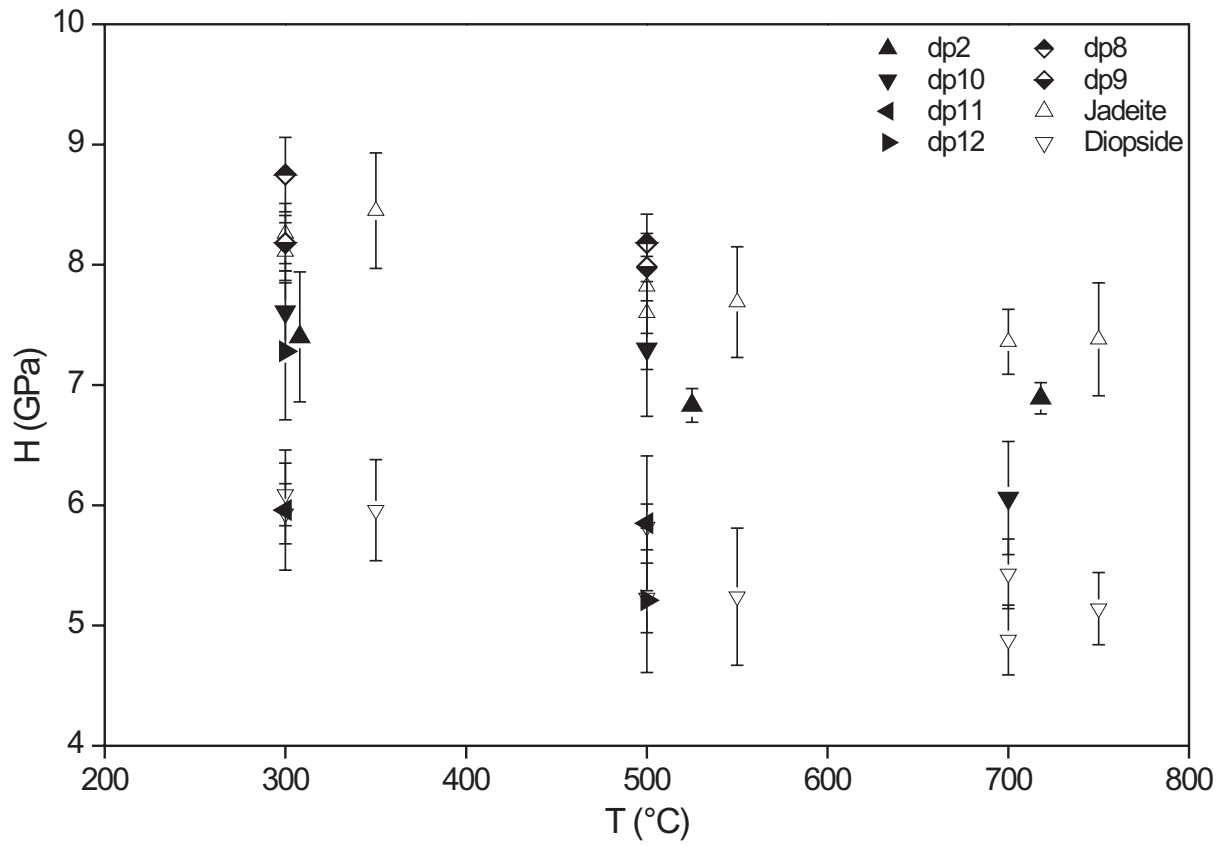


Figure 13: Hardness H of omphacite as a function of temperature T . Indentation hardness tests were performed on two different omphacites. Omphacite I: dp8, dp9 (half filled symbols); Omphacite II: dp2, dp10, dp11, dp12 (filled symbols). The hardness data of jadeite and diopside (Fig. 12, Tab. 2) are included for comparison (open symbols).

Table 4: Results of hardness tests on omphacite (Omphacite I: dp8, dp9; Omphacite II: dp2, dp10, dp11, dp12). The given hardness data are the mean and the standard deviation of about 25 individual measurements at the same test conditions and within the same grain.

Sample	Temperature ($^{\circ}\text{C}$)	Hardness (GPa)
dp2	308	7.4 ± 0.5
	525	6.8 ± 0.1
	718	6.9 ± 0.1
dp8	300	8.8 ± 0.3
	500	8.2 ± 0.2
dp9	300	8.2 ± 0.2
	500	8.0 ± 0.3
dp10	300	7.6 ± 0.3
	500	7.3 ± 0.6
	700	6.1 ± 0.5
dp11	300	6.0 ± 0.5
	500	5.9 ± 0.6
dp12	300	7.3 ± 0.6
	500	5.2 ± 0.6

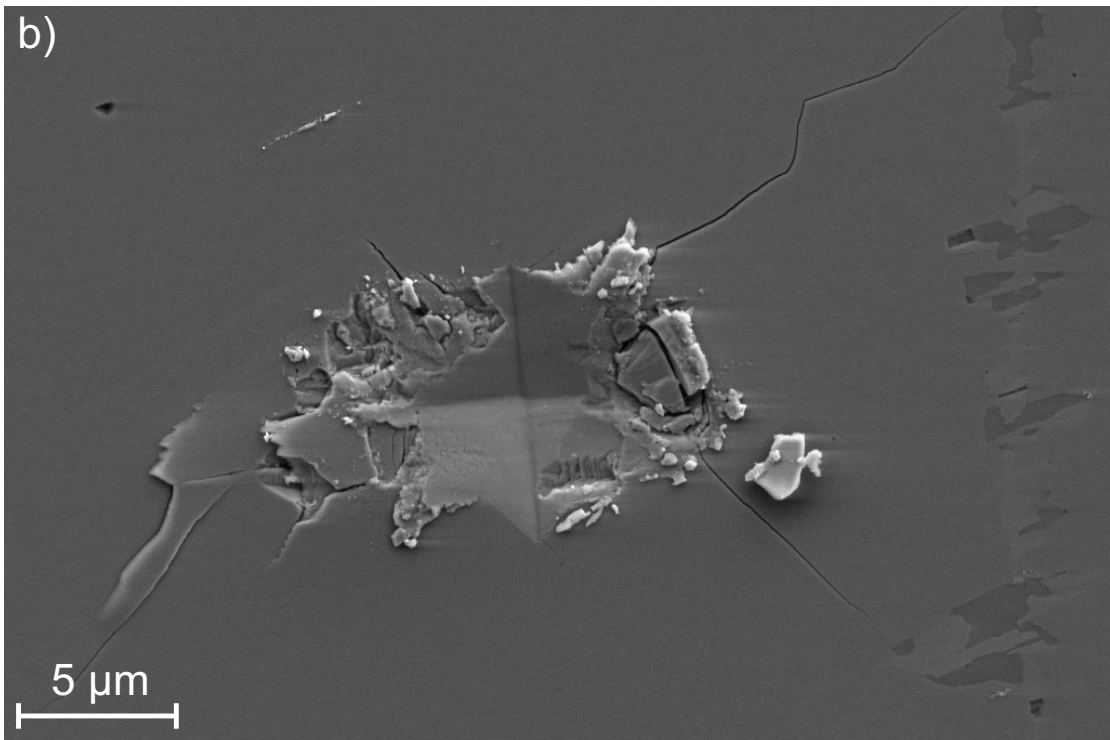
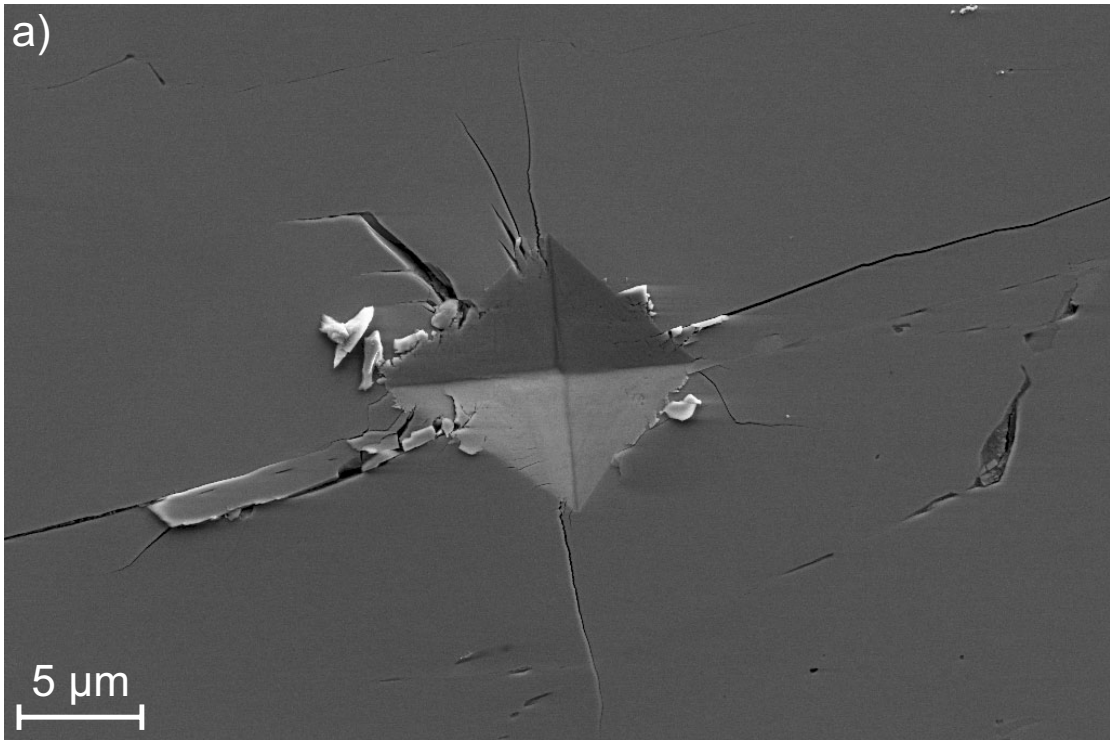


Figure 14: SEM images of indents in omphacite (Sample dp11). a) Indent generated at 500 °C showing no tear-out, only minor cracking. b) Indent generated at 700 °C characterized by strong tear-out of sample material.

3.7 Discussion

3.7.1 Relative strength of the end members jadeite and diopside

Plastic deformation of rocks can take place in different deformation regimes. These regimes denote ranges of temperature, flow stress and strain rate, where different deformation mechanisms and accompanying processes are dominant (Frost and Ashby, 1982; Schmid, 1982; Poirier, 1985). The deformation regime accessed by indentation hardness tests is suggested to be low-temperature plasticity (Dorner *et al.*, in review) with dislocation glide being the dominant deformation mechanism. Dislocation glide is either limited by discrete obstacles or a lattice resistance (Frost and Ashby, 1982). For most metals the lattice resistance is low, but for ionically or covalently bonded crystals, as the pyroxenes of this study, the lattice resistance is high (e. g. Kelly, 1966; Guyot and Dorn, 1967). The stress required to overcome the lattice resistance is the Peierls stress τ_p . For an edge dislocation it can be given as

$$\tau_p = \frac{2\mu}{1-\nu} \exp\left(-\frac{2\pi a}{(1-\nu)b}\right), \quad (3)$$

with μ denoting the shear modulus, ν the Poisson ratio, a the lattice spacing of the slip plane, and b the magnitude of the Burgers vector (Nabarro, 1967). A comparison of these parameters for jadeite and diopside reveals that the difference of the shear moduli is the most significant. In the temperature range from 300 °C to 700 °C the shear modulus of jadeite decreases from about 77 GPa to 71 GPa, that of diopside from about 60 GPa to 56 GPa (Tab. 5). The temperature dependence of the elastic moduli is considered according to Duffy and Anderson (1989), taking into account the Fe content of the tested diopside grains. For the shear moduli of jadeite $\mu(T) = 84 \text{ GPa} - 0.013 \text{ GPa/K} \cdot T$, and for that of diopside $\mu(T) = 66 \text{ GPa} - 0.010 \text{ GPa/K} \cdot T$ is used (Duffy and Anderson, 1989). The shear modulus of jadeite is thus found to be about 27 % higher than that of diopside, while the differences of the Poisson ratios, the lattice spacings of the slip planes, and the magnitudes of the Burgers vectors for jadeite and diopside are about 1 % to 3 %, respectively (Tab. 5). The magnitude of the Burgers vector and the lattice spacing are taken from Cameron *et al.* (1973) assuming that the (100)[001] system is relevant. Since the most significant difference is obtained for the shear moduli, the hardness data were tentatively normalized with respect to the temperature dependent shear moduli (Fig. 15). This normalization reduces the difference in strength of jadeite and diopside to about 10 %, compared to an average strength difference of about 43 % before normalization.

The remaining contrast in strength can be attributed to various sources. On principle, it could reflect experimental errors in the hardness data and the shear modulus. The used derivatives of the shear modulus with respect to temperature could be incorrect, since they

Table 5: Comparison of the shear modulus μ , the Poisson ratio ν , the magnitude of the Burgers vector b , and the lattice spacing of the slip plane a for jadeite and diopside. The values for the elastic moduli are according to Duffy and Anderson (1989). The values of the magnitude of the Burgers vector and the lattice spacing are taken from Cameron *et al.* (1973) assuming that the (100)[001] system is relevant.

	Temperature (°C)	Jadeite	Diopside	Difference ($x_{Diopside} - x_{Jadeite}$)/ $x_{Jadeite}$
μ (GPa)	300	76.6	60.1	-27.5 %
	700	71.4	56.1	-27.3 %
ν	300	0.260	0.263	1.1 %
	700	0.264	0.267	1.1 %
b (Å)	300	5.23	5.26	0.6 %
	700	5.24	5.28	0.8 %
a (Å)	300	9.44	9.77	3.4 %
	700	9.48	9.80	3.3 %

are not measured, but predicted from elasticity systematics (Duffy and Anderson, 1989). Also, the slight deviations of the tested jadeite and diopside from the ideal composition could be a reason for the remaining strength contrast. On the other hand, normalization with respect to the Peierls stress itself, instead of the shear modulus, will not reduce the remaining strength differences, as the Peierls stress is a strong function of the shear modulus. Finally, it cannot be excluded that the strength contrast after normalization results from different concentrations of discrete obstacles, e. g. impurities, against dislocation glide in the natural crystals used.

In addition to normalizing the hardness respectively flow stress with respect to the shear modulus, the temperature is usually normalized with respect to the melting temperature (e.g. Frost and Ashby, 1982; Karato, 1989; Karato *et al.*, 1995a). However, dislocation glide, which is the dominant deformation mechanism in the low-temperature plasticity regime addressed in the hardness tests, is not primarily a thermally activated process. Therefore, normalization with respect to the melting temperature is suggested to have no significant effect with regard to a better correspondence of the mechanical data. In fact, normalization of our hardness data with respect to both melting temperature and shear modulus yields a somewhat inferior correspondence between the data sets for jadeite and diopside compared to normalizing with respect to the shear modulus only (Figs. 15 and 16). The Peierls equation (Eq. 3) indicates that the temperature dependence of the hardness is only indirect and related to the temperature dependence of the shear modulus, the Poisson ratio, the lattice spacing, and the Burgers vector. This is supported by our data showing that part of the observed weak temperature dependence of the hardness can be attributed to the temperature

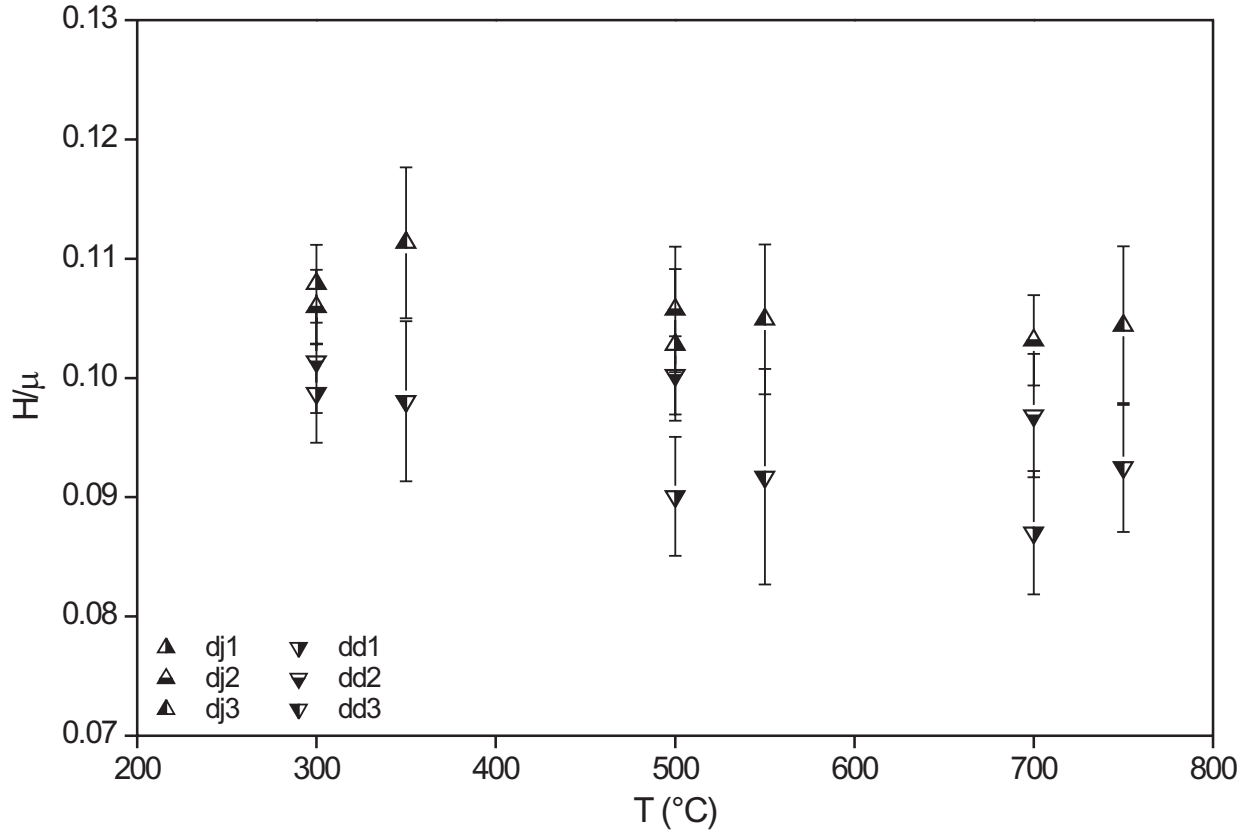


Figure 15: Normalized hardness H/μ of jadeite (Samples dj1, dj2, dj3) and diopside (Samples dd1, dd2, dd3) as a function of temperature T . The temperature dependence of the shear moduli as determined by Duffy and Anderson (1989) was used for the calculation of the corresponding shear moduli: $\mu(T) = 84 \text{ GPa} - 0.013 \text{ GPa/K} \cdot T$ for jadeite and $\mu(T) = 66 \text{ GPa} - 0.010 \text{ GPa/K} \cdot T$ for diopside.

dependence of the shear modulus. For an increase in temperature of $400 \text{ }^\circ\text{C}$ the hardness decreases on average by approximately 12%, whereas the normalized hardness decreases only by about 6%. The remaining dependence on temperature after normalization is possibly due to the formation of kink-pairs during dislocation glide, which is a thermally activated process (Suzuki *et al.*, 1991).

The concept of classifying solid phases into isomechanical groups was first suggested by Frost and Ashby (1982). The members of an isomechanical group show similar mechanical behaviour when the data are properly normalized. The materials that belong to the same isomechanical group are usually characterized by the same crystal structure and similar bonding. Frost and Ashby (1982) defined 21 isomechanical groups, which cover cubic, tetragonal, hexagonal, and trigonal solid phases. Karato (1989) found a systematic relationship in plastic behaviour of cubic garnet, spinel, and rock salt, as well as for orthorhombic olivine and perovskite. The indentation hardness tests of the present study reveal that the

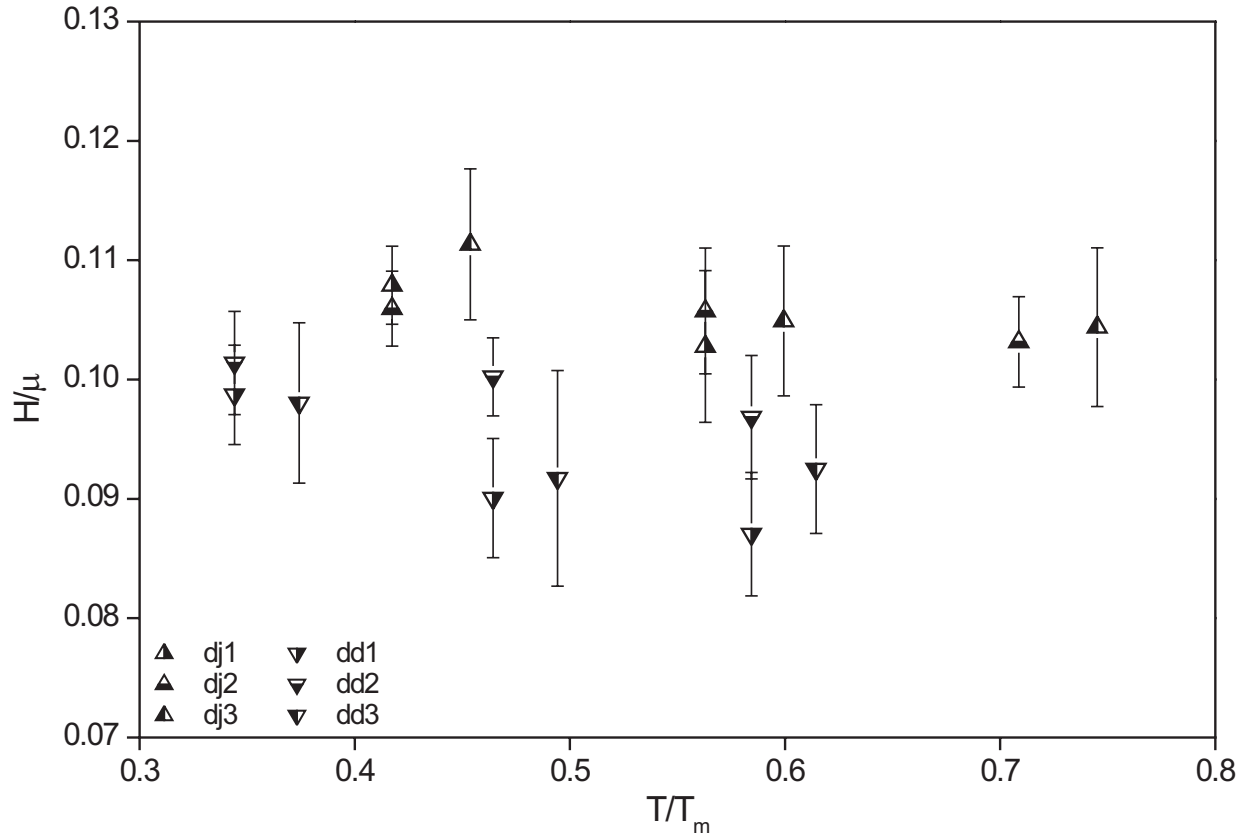


Figure 16: As figure 15, but using the homologous temperature T/T_m instead of the actual test temperature T .

strength of jadeite and diopside is very similar after normalization (Fig. 15). This indicates that jadeite and diopside belong to the same isomechanical group and that the systematics in the mechanical behaviour can be extended to monoclinic pyroxenes.

In the present study, the hardness data of jadeite and diopside for different temperatures are found to be linear dependent on the shear modulus (Fig. 17). The best linear fit of the data (Fig. 17) is described by

$$H = -3.1 \text{ GPa} + 0.15 \cdot \mu . \quad (4)$$

Fitting the data with a straight line through the origin (Fig. 17) yields

$$H = 0.10 \cdot \mu . \quad (5)$$

This linear relationship between the hardness of jadeite and diopside and the corresponding shear moduli is consistent with a comprehensive data set compiled by Teter (1998), who found that the shear modulus is a better predictor for the hardness of a material than the bulk modulus. For fcc metals, NaCl-structure alkali halides, and diamond cubic solids, Gerk (1977) found that hardness and shear modulus are related according to $H = 10^{-2}\mu$, which

differs by a factor of 10 compared to the relationship (Eq. 5) found in the present study. The fact that the hardness data as a function of the shear modulus for jadeite as well as diopside can be described by one functional relationship supports that jadeite and diopside belong to the same isomechanical group.

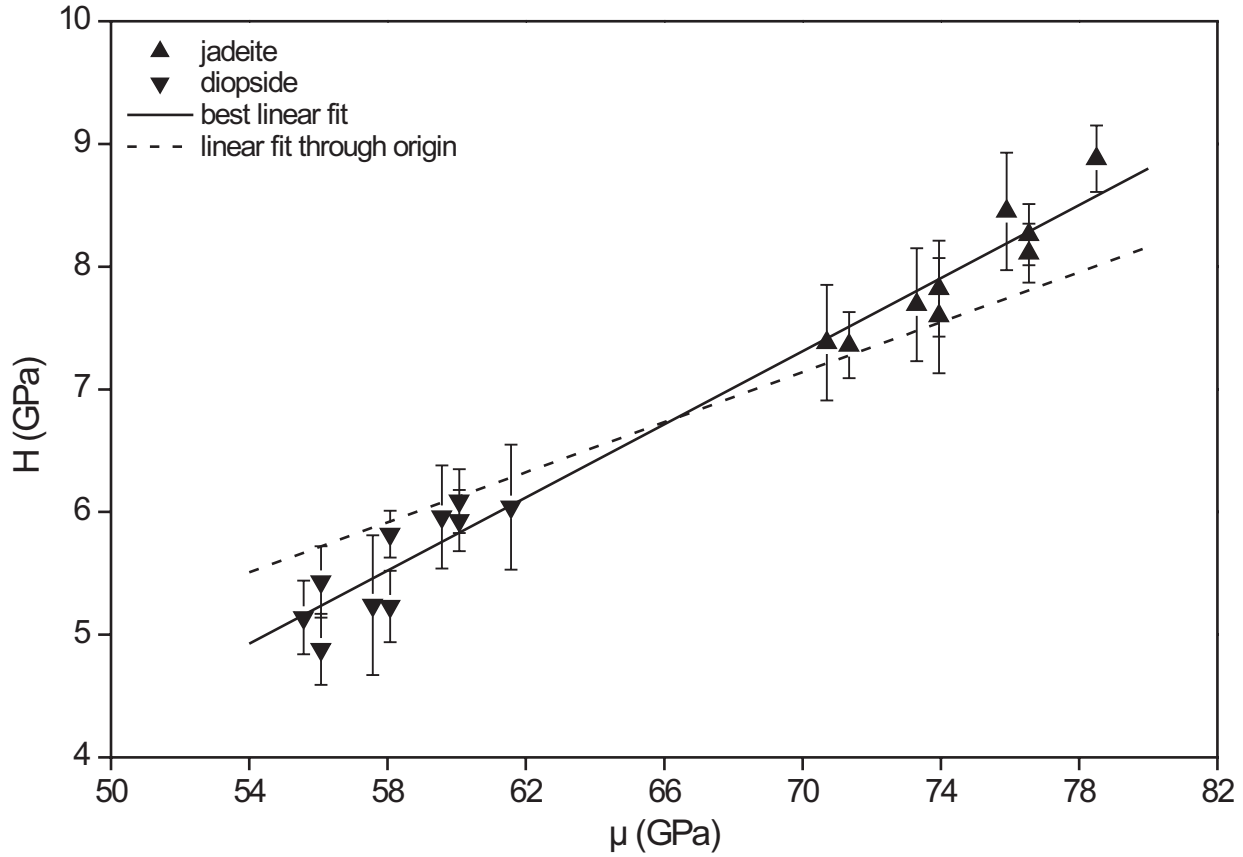


Figure 17: Hardness H of jadeite and diopside for different temperatures as a function of the temperature dependent shear modulus μ . Two linear fits of the data are also included, one being a fit through the origin, and the other the best linear fit.

The indentation hardness tests of the present study reveal that jadeite is stronger than diopside in the low-temperature plasticity regime. In contrast, for the dislocation creep regime it is supposed that the strength of jadeite is lower than that of diopside, since for a given temperature the homologous temperature of jadeite is higher than that of diopside (Stöckhert and Renner, 1998). Recently Orzol *et al.* (2002) experimentally confirmed that jadeite is weaker than diopside in the dislocation creep regime. The conclusion that jadeite and diopside belong to the same isomechanical group, as inferred from indentation hardness tests in the low-temperature plasticity regime in this study, is possibly also true for other deformation regimes.

3.7.2 Morphology of the indents

SEM analysis of the morphology of indents in jadeite and diopside crystals revealed linear features in the surrounding surface (Fig. 18). These lineations can be either interpreted as slip steps that are generated during indentation where mobile dislocations reach the sample surface (Dorner *et al.*, in review). Alternatively, steps in the sample surface can be due to mechanical twinning. From the analysis of the orientation of these steps with respect to the crystal orientation (Fig. 19), (100) is determined as the corresponding lattice plane. For clinopyroxenes, (100)[001] is the predominant slip system in dislocation glide and also the plane and direction of mechanical twinning (e.g. Mercier, 1985; Avé Lallemant, 1978). The critical resolved shear stress for twinning is a weak function of temperature (Tullis, 1980). For clinopyroxene it is about 150 MPa (Kollé and Blacic, 1982; Orzol *et al.*, 2003). Generally, at low temperatures the critical resolved shear stress for dislocation glide is higher than that for mechanical twinning (Avé Lallemant, 1978; Tullis, 1980; Mercier, 1985). Therefore, mechanical twinning is more common at low temperatures and sufficiently high stresses. The flow stress that corresponds to a hardness datum is proposed to be about one-third of the hardness (Tabor, 1970). In our hardness tests on pyroxenes flow stresses of about 2 GPa to 3 GPa correspond to the observed hardness of about 5 GPa to 9 GPa (Tab. 2). These high flow stresses are expected to be sufficient to activate both dislocation glide and mechanical twinning. Thus, the observed linear features can be the results of dislocation glide on (100) and (100) twinning as well, both being consistent with deformation in the low-temperature plasticity regime.

3.7.3 Unsystematic results on omphacite solid solutions

Various potential problems have to be taken into account, when the results obtained for the end members jadeite and diopside of the clinopyroxene solid solution series are transferred to members with an intermediate composition. First, omphacite occurs in the ordered P2/n structure as well as in the disordered C2/c structure. The equilibrium disorder/order temperature was determined to 725 °C by Fleet *et al.* (1978) and to 865 °C by Carpenter (1981) for natural omphacites with an intermediate composition. Since ordering rates in omphacite are slow (Carpenter, 1978, 1981), changes of the degree of ordering are not supposed to occur during our indentation experiments, which were performed at temperatures between 300 °C and 700 °C. However, different thermal histories of natural samples are expected to result in differences in the ordering states. Brenker *et al.* (2002) proposed that different slip systems are active in the ordered P2/n and in the disordered C2/c structure. Therefore, the strength of omphacite could be dependent on the degree of ordering.

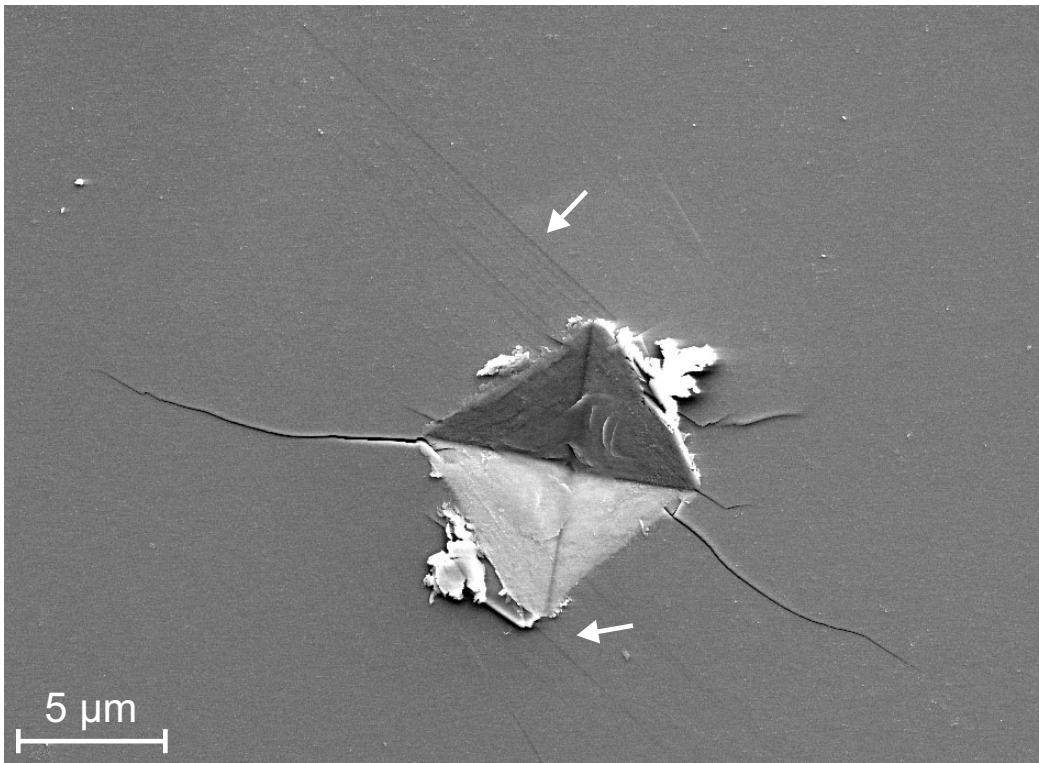


Figure 18: SEM image of an indent in jadeite (Sample dj3, 350 °C). The arrows point to linear features that developed during the indentation process.

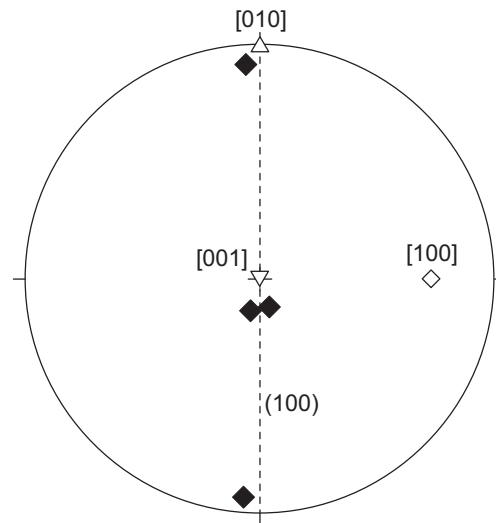


Figure 19: Orientation of linear features in the surface around the indents in two jadeite and diopside samples, respectively (Samples jd1, jd3, dd1, dd3). The orientations of the linear features are shown as directions (filled black diamonds) with respect to the crystal orientation (empty symbols). The corresponding slip plane is also included (broken line).

Second, at low temperatures exsolution is possible in omphacites (Carpenter, 1978, 1980). Microstructural investigations of natural omphacites reveal a great variability of microstructures with antiphase domains, originating by ordering, and exsolution lamellae (e.g. Car-

penter, 1978). These microstructural features change within single grains over distances of less than $1\ \mu\text{m}$ (Carpenter, 1978), and exsolution lamellae never exceed about $500\ \text{\AA}$ in width (Carpenter, 1980). Carpenter (1978) suggested that slight differences in chemical composition and differences in the initial ordering state after crystallization causes the microstructural variations.

Our microindentation hardness tests on natural omphacite revealed a highly variable strength, both within single grains and comparing different specimens. The strength contrast between both tested omphacites is supposed to arise from different ordering states or from slight compositional differences, though the chemical composition being approximately the same. Also, the contrast in strength could be caused by different concentrations or types of submicroscopic inclusions. It is suspected that the variability in strength within single grains may be related to variations in the ordering state, the occurrence of exsolution within short distances, or inhomogeneously distributed submicroscopic inclusions. A more detailed analysis, requiring observations within the scale accessible with transmission electron microscopy, is beyond the scope of the present study.

Furthermore, at a temperature of $700\ ^\circ\text{C}$, the sample material tears out during indentation (Fig. 14). Since omphacite is unstable at low pressures, it is suggested to undergo a phase transformation at higher temperatures resulting in the observed unstable mechanical behaviour. The complex stress field under an indenter during indentation hardness tests has a hydrostatic component that is about two-thirds of the hardness (Tabor, 1970), which is about $3\ \text{GPa}$ to $6\ \text{GPa}$ in our case. While this pressure should suppress phase transformations in the volume underneath the indenter, the hydrostatic component of the stress field vanishes at the sample surface. Thus, the tested omphacite possibly undergoes a local phase transformation enhanced by strain energy.

3.8 Summary and conclusions

(1) Microindentation hardness tests performed on jadeite and diopside grains within natural aggregates at temperatures between $300\ ^\circ\text{C}$ and $750\ ^\circ\text{C}$, corresponding to homologous temperatures of 0.42 to 0.75 for jadeite and 0.34 to 0.61 for diopside, reveal that the hardness of jadeite is about 43% higher than that of diopside.

(2) Normalization of the hardness data with respect to the shear modulus reduces the contrast in strength between jadeite and diopside to about 10% . This indicates that jadeite and diopside belong to the same isomechanical group.

(3) The hardness of jadeite and diopside is linearly dependent on the shear modulus. This correlation of hardness and shear modulus seems reasonable for indentation hardness tests in

the low-temperature plasticity regime, since the Peierls stress also depends linearly on the shear modulus.

(4) Microindentation hardness tests on two different omphacite samples reveal a strength contrast as well as a considerable strength variability within one of the tested omphacite samples. Variable degrees of ordering, exsolution, and submicroscopic solid phase or fluid inclusions are suspected as possible reasons for the apparently unsystematic results on omphacite.

(5) The results on jadeite and diopside demonstrate that indentation hardness tests provide information on the relative strength of minerals in the low-temperature plasticity regime. For members of solid solution series this information allows a classification into isomechanical groups.

4 Creep of a TiAl alloy: a comparison of indentation and tensile testing

4.1 Abstract

The present study compares the indentation and uniaxial creep behaviour of a near- γ -TiAl alloy with a duplex microstructure. Indentation creep tests were performed using a cylindrical indenter at temperatures between 750 °C and 1050 °C and net section stresses between 50 MPa and 1430 MPa. A stress dependent stress exponent ranging from 3 for low net section stresses to 8 for high net section stresses was determined. The apparent activation energy of indentation creep was determined as 343 ± 16 kJ/mol. The stress as well as the temperature dependence of the indentation and uniaxial creep data are in good agreement. The indentation experiments were also analysed with respect to the deformed volume in front of the indenter and the surface bulge that develops around the indenter. A simple dislocation model is proposed to rationalize volume and shape of the bulge around the indenter. The good agreement of creep parameters obtained by indentation and conventional uniaxial creep testing demonstrates that indentation creep tests are suitable to characterize creep.

4.2 Introduction

In engineering materials science uniaxial tensile creep tests are the standard technique to obtain creep parameters. An alternative is provided by indentation creep tests, where a cylindrical indenter is pushed into the flat surface of a solid by a constant load (Chu and Li, 1977; Li, 2002). Compared to conventional creep experiments, indentation creep tests have several advantages. First, only small amounts of material are needed and sample preparation is simple, since only a flat sample surface is required. Moreover, indentation creep tests can be useful for the characterization of the local deformation behaviour of e.g. thin films or particles in composites. Compared to other indentation techniques, e.g. Vickers hardness tests with a pyramid indenter, a cylindrical indenter has the advantage that in a constant load test the net section stress under the indenter is constant, whereas with other indenter geometries it decreases with time. Finally, indentation creep tests with cylindrical indenters avoid problems associated with very high local stresses which characterize the tip region during indentation with sharp indenters. A recent review of indentation creep testing with emphasis on the testing of local material properties is given by Li (2002).

Several studies dealing with the comparison of indentation and conventional uniaxial creep tests showed that the results compare well when considering both the temperature and the stress dependence of the creep data. Some of these studies are experimental (Yu and Li, 1977a; Chu and Li, 1977, 1979; Murthy and Sastry, 1982; Yu *et al.*, 1985; Juhász *et al.*, 1986; Godavarti and Murty, 1987; Chiang and Li, 1994; Hyde *et al.*, 1995; Cseh *et al.*, 1999), most of them on model materials such as LiF, lead, zinc, β -tin, and copper. Others use finite element creep stress and strain analysis to rationalize indentation creep (Yu and Li, 1977b; Hyde *et al.*, 1993; Becker *et al.*, 1994; Butt *et al.*, 1996; Yue *et al.*, 2000, 2001).

The classical approach to compare indentation and uniaxial creep data makes use of conversion factors (Yu and Li, 1977a,b; Chu and Li, 1977, 1979). The net section stress σ_{net} , which characterizes the load in an indentation creep test, is defined as the force F applied on the indenter divided by the circular indenter area A : $\sigma_{net} = F/A$. The conversion factor c_1 relates the net section stress σ_{net} to an appropriate uniaxial reference stress σ by

$$\sigma = c_1 \cdot \sigma_{net} . \quad (6)$$

Experimentally determined values of c_1 range from 0.26 to 0.36 (Chu and Li, 1977, 1979; Yu *et al.*, 1985; Tasnádi *et al.*, 1988; Chiang and Li, 1994). The indentation rate \dot{d} , determined from indentation creep experiments, is related to an appropriate uniaxial reference strain rate $\dot{\epsilon}$ by

$$\dot{\epsilon} = c_2 \cdot \frac{\dot{d}}{2r} , \quad (7)$$

with c_2 denoting the conversion factor and $2r$ the indenter diameter. Relation 7 is often used with $c_2 = 1$ (Chu and Li, 1977, 1979; Chiang and Li, 1994; Butt *et al.*, 1996). Here we use the conversion factors $c_1=0.296$ and $c_2=0.755$ determined with finite element calculations by Hyde *et al.* (1993) to relate creep data from indentation and tensile creep tests. Uniaxial creep behaviour is often described by the well known Sherby-Dorn equation

$$\dot{\epsilon} = A \cdot \sigma^m \cdot \exp \left(-\frac{Q}{RT} \right) , \quad (8)$$

with m denoting the stress exponent, Q the apparent activation energy, T the temperature, R the universal gas constant and A the pre-exponential factor. Inserting the conversion equations (Eqs. 6 and 7) into the power law equation (Eq. 8) reveals that the stress exponents and the apparent activation energies determined from both indentation and uniaxial creep tests are identical.

Recently, Yue *et al.* (2000) outlined a finite element procedure to correlate indentation and uniaxial creep data. Instead of using conversion factors according to equations 6 and 7, they assumed that the indentation rate \dot{d} obeys the power law equation

$$\dot{d} = C_{ind} \cdot \sigma_{net}^n , \quad (9)$$

with n denoting the stress exponent for indentation creep, and C the temperature and material dependent pre-exponential factor for indentation creep. For a material that creeps according to the power law equation (Eq. 8), the isothermal finite element calculations by Yue *et al.* (2000) confirmed the identity of the stress exponents determined from indentation and uniaxial creep tests, respectively. For the determination of the pre-exponential factor for uniaxial creep, they proposed a procedure that uses experimental indentation creep data in combination with finite element calculations. Both approaches relating indentation and uniaxial creep propose identical stress exponents, thus indicating that indentation creep experiments can be used to determine the uniaxial stress exponent.

One objective of the present study is to compare indentation and conventional tensile creep data for an engineering alloy, since most previous studies were performed on model materials. The data are compared on the basis of the two described approaches in order to validate them for an industrial material. For this purpose both indentation and tensile creep tests are performed on the same material. Furthermore, a simple dislocation model is proposed to rationalize material flow during indentation creep on a dislocation basis.

4.3 Experimental

4.3.1 Sample material

The material used for both the uniaxial tensile and the indentation creep experiments is a TiAl alloy of type Ti-47Al-2Mn-2Nb + 0.8 vol.% TiB₂ XDTM produced by Howmet Corporation (Whitehall, USA). Cast rods were HIPed (1260 °C/172 MPa) followed by a heat treatment in vacuum at 1010 °C for 50 h. The resulting undeformed near- γ -TiAl alloy shows a duplex microstructure with lamellar $\alpha_2 + \gamma$ grains and equiaxed γ grains. The lamellar grains are characterized by a grain size of 30 μm and occupy a volume fraction of 15 % to 20 %. The diameter of the γ grains is 15 μm . A preferred orientation is not developed. The grain sizes of both the lamellar and the γ grains are significantly smaller than the diameter of the indenter used in the indentation creep tests. Therefore, the sample material can be considered as homogeneous and isotropic.

4.3.2 Indentation and tensile creep testing

The indentation creep tests were performed in air using a creep apparatus that is suitable for experiments at temperatures of up to 1400 °C (Fig. 20a). The cylindrical indenters are made from Al₂O₃ and have a height of 1 mm and a diameter of 1 mm or 2 mm. The indenter

is positioned on top of a cylindrical sample with a height of 8 mm and a diameter of 15.5 mm (Fig. 20b). The load is directly applied by placing weights on top of the upper piston and measured by a load cell (Fig. 20a). The sample assembly including upper and lower piston is surrounded by a vertical tube furnace. A PtRh-Pt thermocouple placed next to the sample measures the temperature (Fig. 20b). The displacement is detected using Al_2O_3 rods, which transfer the signal to two LVDT displacement transducers outside the furnace. The signal of one LVDT is used to correct for temperature effects on the loading column.

Details concerning indentation creep testing are reported in the present study, whereas those of the uniaxial tensile creep tests were reported previously (Skrotzki *et al.*, 1999). The standard tensile creep experiments were performed on cylindrical samples with a diameter of 5 mm and a gauge length of 25 mm.

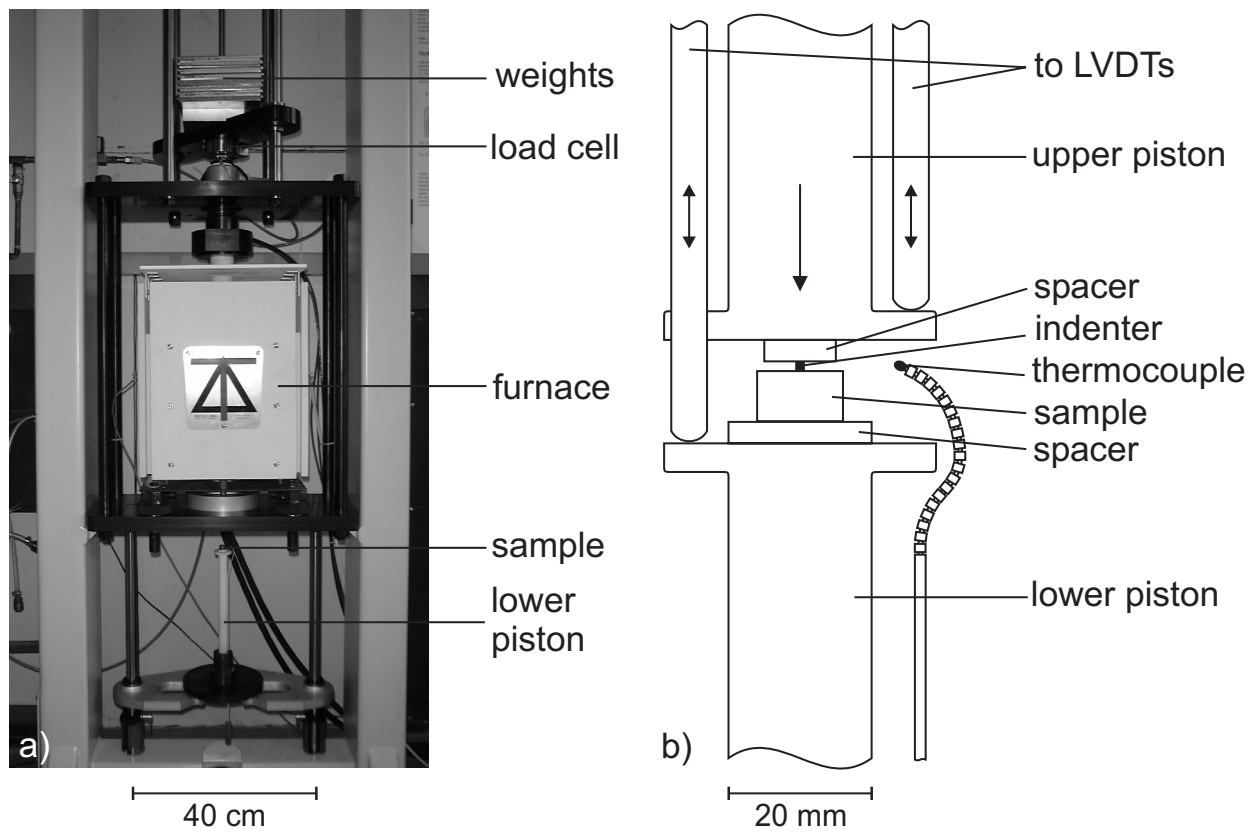


Figure 20: a) Central part of the creep test rig. b) Scheme of the sample assembly for indentation creep experiments with a cylindrical indenter.

4.4 Results

4.4.1 Indentation and tensile creep data

Indentation creep experiments were performed on three TiAl alloy samples (T1, T2, and T3). All three experiments comprise several creep periods during progressive indentation. Each creep period is characterized by one set of net section stress and temperature (Tab. 6). Sample T1 was indented by a cylinder with a diameter of 2 mm at net section stresses ranging from 51 MPa to 183 MPa and temperatures between 854 °C and 1051 °C. Sample T2 was subjected to a temperature of about 750 °C and the net section stresses varied from 810 MPa to 1426 MPa. Sample T3 was indented at a temperature of 902 °C and net section stresses ranging from 196 MPa to 647 MPa. An indenter with a diameter of 1 mm was used for experiments T2 and T3.

The indentation creep curves show the indentation depth as a function of time (Fig. 21). Note that while individual indentation creep curves do not always exhibit a pronounced primary creep stage they all eventually reach a constant indentation rate. Each creep period in our indentation creep tests is characterized by this constant indentation rate (Fig. 21, Tab. 6). For sample T1 the determined indentation rates range from $8.0 \cdot 10^{-11}$ m/s to $1.6 \cdot 10^{-8}$ m/s, for sample T2 from $6.6 \cdot 10^{-11}$ m/s to $4.2 \cdot 10^{-9}$ m/s, and for sample T3 from $3.8 \cdot 10^{-11}$ m/s to $1.5 \cdot 10^{-8}$ m/s.

For creep periods characterized by the same temperature a linear relationship is observed in a log-log plot of indentation rates \dot{d} versus net section stresses σ_{net} (Figs. 22, 23 and 24). This demonstrates that the proportionality

$$\dot{d} \sim \sigma_{net}^n . \quad (10)$$

and thus the power law equation (Eq. 9) used by Yue *et al.* (2000) hold for the indentation creep tests, at least for a limited stress range. The stress exponent is determined to be $n = 3.2 \pm 0.1$ for low net section stresses of 51 MPa to 183 MPa at 1050 °C (Fig. 22, Tab. 7). For a temperature of 900 °C and net section stresses of 196 MPa to 647 MPa it is $n = 5.2 \pm 0.4$ (Fig. 23, Tab. 7). For higher net section stresses of 810 MPa to 1426 MPa at a temperature of 750 °C the stress exponent is $n = 7.6 \pm 0.3$ (Fig. 24, Tab. 7). These results reveal that the stress exponent for the TiAl alloy is stress dependent ranging from about 3 to 8.

Considering creep periods with the same net section stress, an Arrhenius plot of indentation rates \dot{d} versus inverse temperatures $1/T$ also shows a linear relationship (Fig. 25), thus indicating that the relation

$$\dot{d} \sim \exp\left(-\frac{Q}{RT}\right) \quad (11)$$

Table 6: Compilation of the results obtained from indentation creep tests on a TiAl alloy. T: temperature; σ_{net} : net section stress; \dot{d} : indentation rate.

Sample	Creep period	T (°C)	σ_{net} (MPa)	\dot{d} (m/s)
T1	1	854	183	$8.0 \cdot 10^{-11}$
	2	898	183	$2.4 \cdot 10^{-10}$
	3	949	183	$9.9 \cdot 10^{-10}$
	4	999	182	$4.1 \cdot 10^{-9}$
	5	1051	182	$1.6 \cdot 10^{-8}$
	6	1051	90	$1.7 \cdot 10^{-9}$
	7	1051	110	$2.5 \cdot 10^{-9}$
	8	1051	131	$4.2 \cdot 10^{-9}$
	9	1050	71	$6.9 \cdot 10^{-10}$
	10	1050	51	$2.4 \cdot 10^{-10}$
	11	896	183	$1.7 \cdot 10^{-10}$
T2	1	750	810	$6.6 \cdot 10^{-11}$
	2	749	917	$1.4 \cdot 10^{-10}$
	3	750	1038	$5.3 \cdot 10^{-10}$
	4	750	1087	$7.4 \cdot 10^{-10}$
	5	750	1136	$1.1 \cdot 10^{-9}$
	6	750	1187	$1.5 \cdot 10^{-9}$
	7	750	1237	$2.1 \cdot 10^{-9}$
	8	750	1286	$2.5 \cdot 10^{-9}$
	9	750	1326	$3.1 \cdot 10^{-9}$
	10	749	1366	$2.8 \cdot 10^{-9}$
	11	749	1426	$4.2 \cdot 10^{-9}$
T3	1	902	196	$3.8 \cdot 10^{-11}$
	2	902	280	$1.7 \cdot 10^{-10}$
	3	902	353	$1.2 \cdot 10^{-9}$
	4	902	483	$4.7 \cdot 10^{-9}$
	5	902	647	$1.5 \cdot 10^{-8}$

Table 7: Compilation of stress exponents and activation energies obtained from indentation creep tests and conventional tensile creep tests. T: temperature; σ_{net} : net section stress; σ : tensile creep stress; n: stress exponent; Q: activation energy.

Reference	T (°C)	σ_{net} or σ (MPa)	n	Q (kJ/mol)
Indentation creep/this study	854-1050	183	-	343
”	1050	51-183	3.2	-
”	900	196-647	5.2	-
”	750	810-1426	7.6	-
Tensile creep/Skrotzki <i>et al.</i> (1999)	750	150-350	7.3	-
”	650-750	150-350	-	288-398

is valid for indentation creep experiments. For a constant load of $\sigma_{net} = 183$ MPa and temperatures between 854 °C and 1050 °C an apparent activation energy of $Q = 343 \pm 16$ kJ/mol

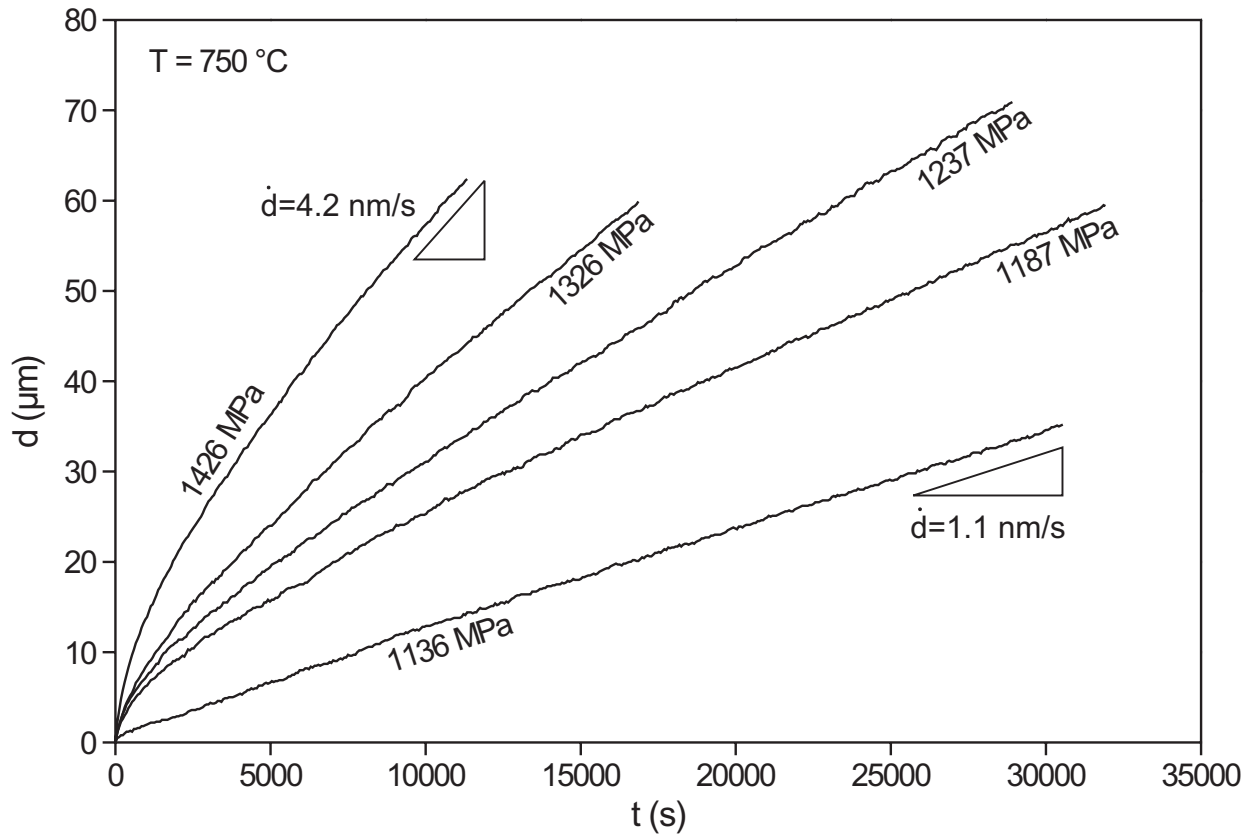


Figure 21: Indentation depth d as a function of time t . Indentation creep curves of several creep periods at different net section stresses at $750\text{ }^\circ\text{C}$ (Sample T2) are shown. The numbers next to the creep curves denote the applied net section stresses. The indentation rate decreases after loading and finally establish a constant rate, which varies from 1.1 nm/s at a net section stress of 1136 MPa to 4.2 nm/s at 1426 MPa .

was determined (Fig. 25, Tab. 7).

The results of the uniaxial tensile creep experiments are described in detail by Skrotzki *et al.* (1999). The uniaxial creep stresses varied between 150 to 350 MPa and the test temperature range was 650 to $750\text{ }^\circ\text{C}$. Although the experimental results by Skrotzki *et al.* (1999) show a stress dependent stress exponent increasing from 3 at low stresses to 8 at high stresses, the experimental scatter of the data also allows interpretation of the results on the basis of a constant stress exponent. This can be seen from the straight line in Figure 28, that reasonably accounts for the experimental data. For $750\text{ }^\circ\text{C}$ this yields a stress exponent of 7.3 ± 0.8 (Fig. 28, Tab. 7). The apparent activation energy determined by Skrotzki *et al.* (1999) ranges from 288 kJ/mol at low stresses to 398 kJ/mol at high stresses.

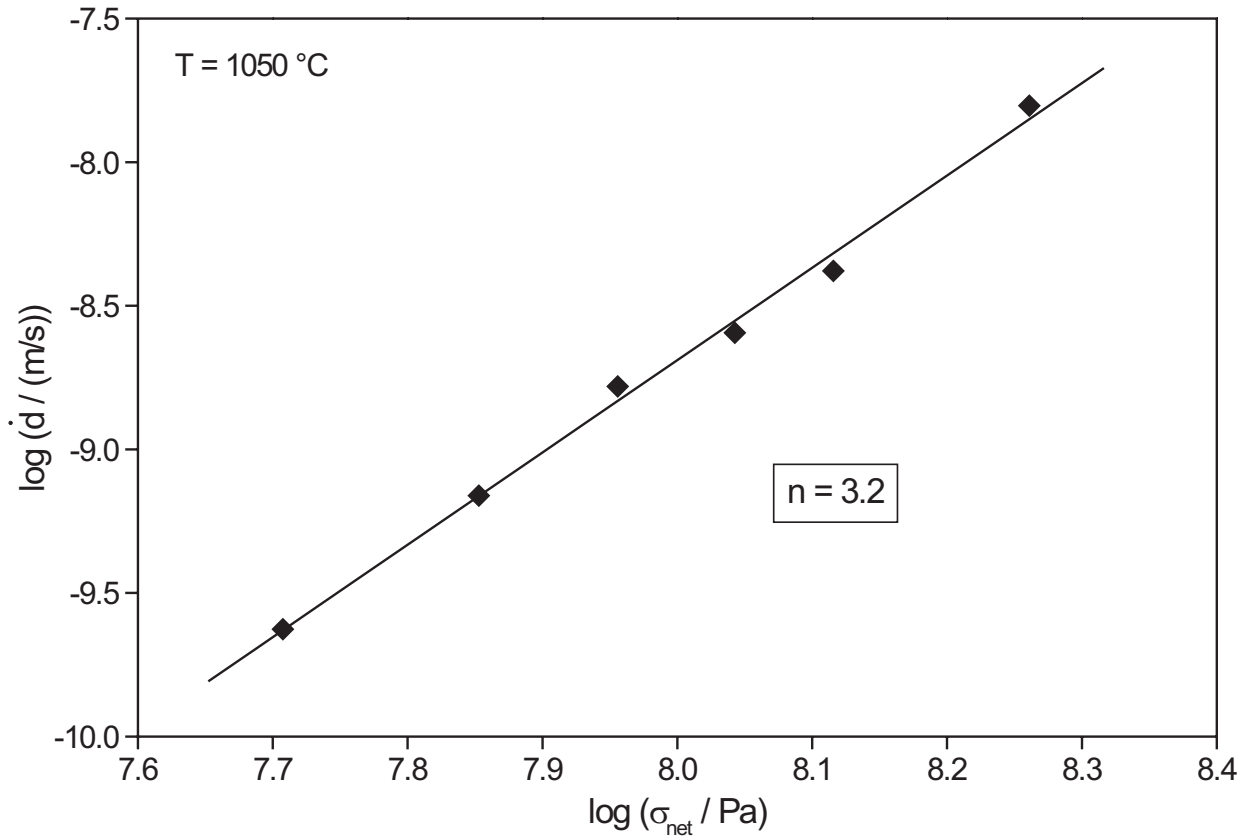


Figure 22: Log-log plot of indentation rate \dot{d} versus net section stress σ_{net} for a temperature of 1050 °C (Sample T1).

4.4.2 Morphological and microstructural aspects of indentation creep testing

In this section we characterize the surface morphology around the indenter, that developed during indentation creep, as well as the deformed volume in front of the indenter. The investigation of the indent after an indentation creep test reveals two prominent features (Fig. 26a). Firstly, the sample material bulges out around the indenter (Figs. 26a, 26b). For one indent of 1 mm diameter the height and the diameter of the surface bulge were determined as about 130 μm and 3 mm, respectively, using an optical microscope. The volume of the bulge was roughly estimated as $4 \cdot 10^{-10} \text{ m}^3$ by approximating its shape as a truncated cone with an inner hole. The volume displaced by the indenter is about $7 \cdot 10^{-10} \text{ m}^3$. Thus, only about half of the displaced material can be found in the direct vicinity of the indent.

The other characteristic feature is a gap between the indenter and the surrounding sample material (Fig. 26a). This gap exists down to the indenter front, since an oxide layer is found between the indenter and the indented material suggesting that there is free space during indentation. The existence of a gap between indenter and sample material indicates that

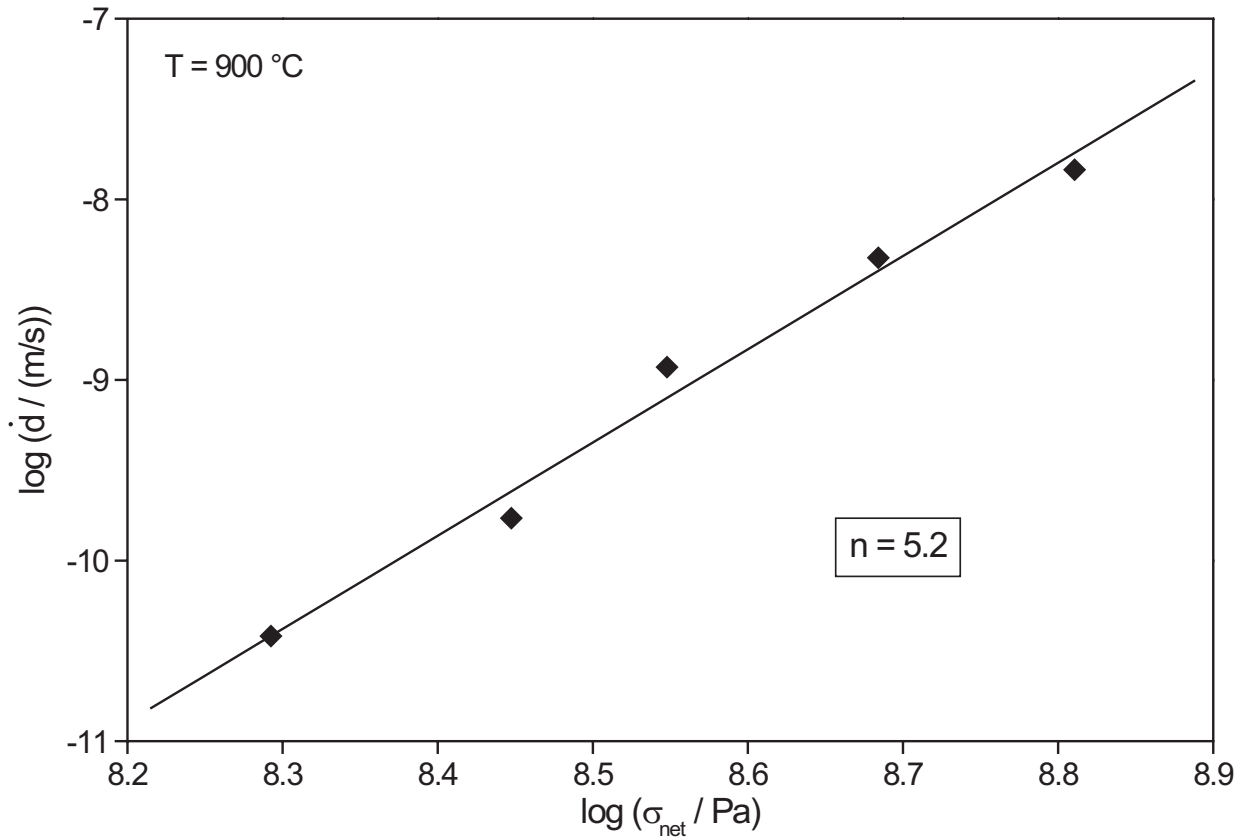


Figure 23: Log-log plot of indentation rate \dot{d} versus net section stress σ_{net} for a temperature of $900\text{ }^{\circ}\text{C}$ (Sample T3).

friction is not important during indentation creep. This is supported by the fact that the indentation creep curves are characterized by a constant indentation rate during secondary creep.

A metallographic cross section through the indenter and the surrounding material reveals a clear line pattern in front of the indenter (Figs. 27a). These lines can be approximated by circle segments with radii that decrease with increasing distance from the indenter (Fig. 27b). Near the indenter edges the line density is higher than in front of the indenter (Figs. 27a, 27b). The diameter of the region where the line pattern is observed is comparable to the indenter diameter. We are not certain about the origin of the contrast of these light and dark lines, but the line pattern is supposed to be associated with material flow during indentation creep. The line density indicates that the strain is higher near the indenter edges than in front of the indenter. This flow pattern resembles that of a sphere in a moving fluid, which is well known in fluid mechanics. The resistance to flow of a sphere is less than that of a flat cylinder. Therefore, the spherical volume in front of the indenter is assumed to become part of the indenting system, and thus the part of material resistance to indentation that is associated with the shape of the indenter is reduced.

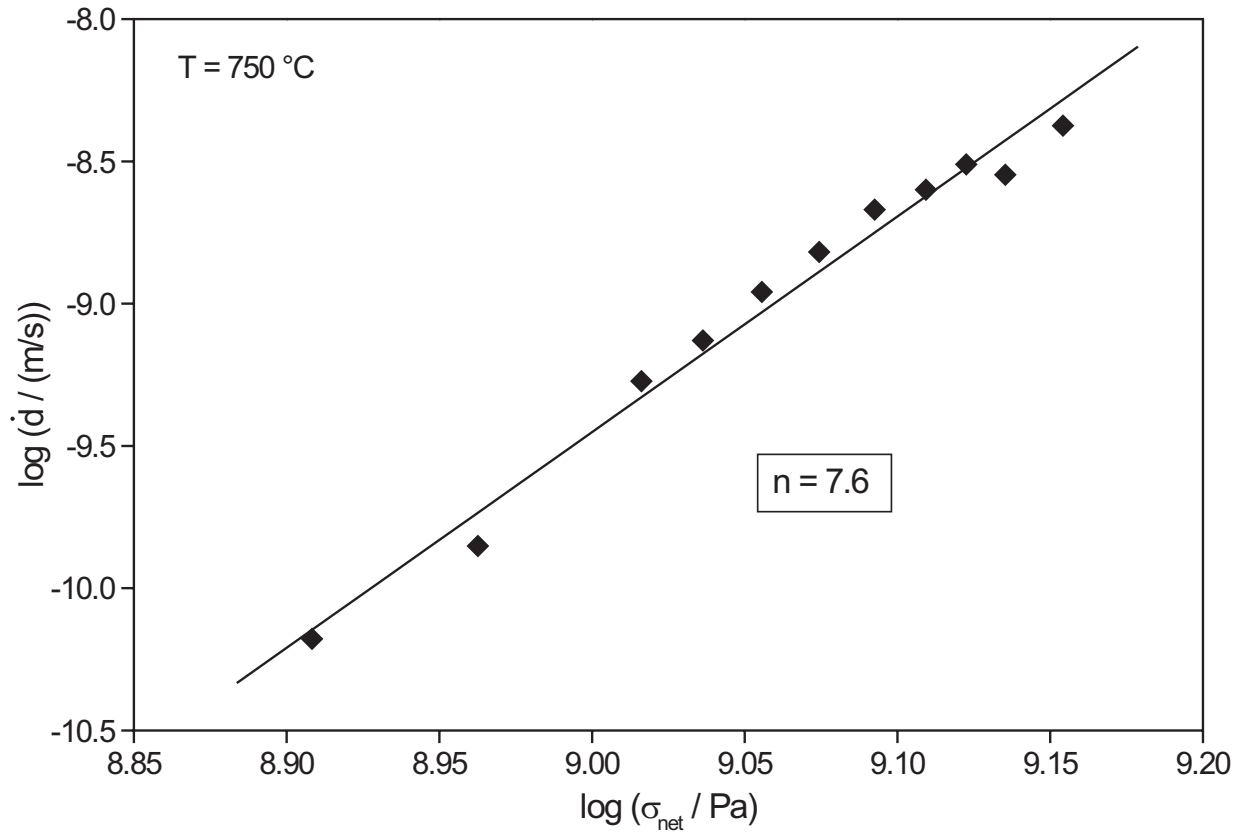


Figure 24: Log-log plot of indentation rate \dot{d} versus net section stress σ_{net} for a temperature of 750 °C (Sample T2).

4.5 Discussion

4.5.1 Comparison of indentation and uniaxial tensile creep tests

First, the indentation and tensile creep data are compared on the basis of the results of Yue *et al.* (2000). Their isothermal finite element calculations reveal that the stress exponents obtained from indentation creep tests and uniaxial creep tests, respectively, are identical. The present study confirms these results experimentally for an engineering alloy. For a temperature of 750 °C the indentation creep tests yield a stress exponent of 7.6 ± 0.3 (Tab. 7, Fig. 24). A comparable stress exponent of 7.3 ± 0.8 was determined from the tensile creep tests for the same test temperature (Tab. 7, Fig. 28). The isothermal finite element modelling of Yue *et al.* (2000) yields no translation rules for the apparent activation energies obtained in indentation and uniaxial creep testing. However, the activation energy of 343 kJ/mol obtained from indentation creep tests is consistent with the activation energy of 288 kJ/mol to 398 kJ/mol determined from the conventional tensile creep experiments (Tab. 7, Fig. 25).

Second, the indentation and tensile creep data are compared using the conversion factors that Hyde *et al.* (1993) determined from finite element modelling. They found that the net

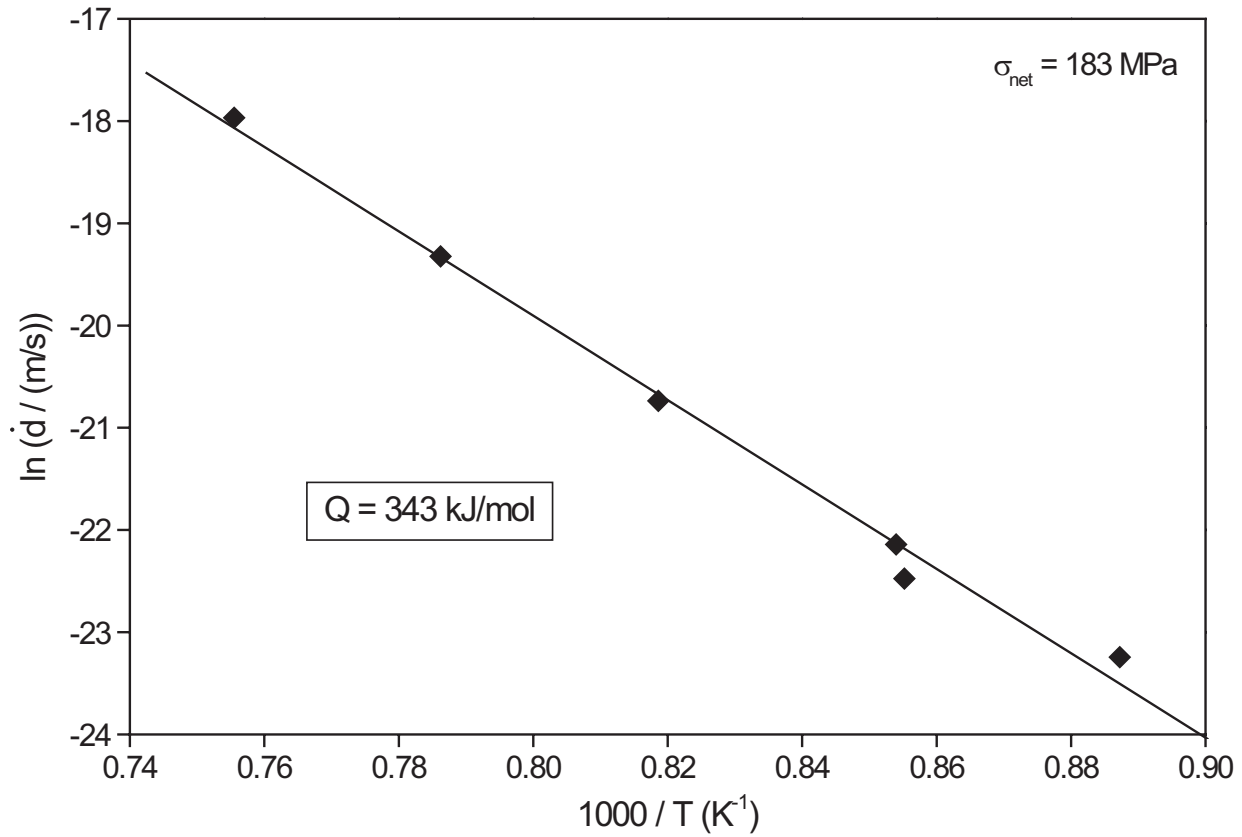


Figure 25: Arrhenius plot of indentation rate \dot{d} versus inverse temperature $1/T$ for a net section stress of 183 MPa (Sample T1).

section stress can be related to the uniaxial creep stress using Equation 6 with $c_1=0.296$, and that the indentation rate can be related to the uniaxial strain rate using Equation 7 with $c_2=0.755$. The converted indentation creep data and the uniaxial creep data for the tested TiAl alloy are in good agreement (Fig. 28). This shows that the approach of Hyde *et al.* (1993) is reasonable and also rationalizes the behaviour of an intermetallic engineering material. Note that the indentation and tensile creep data obtained at different temperatures fall on one master curve (Fig. 28) when the strain rates are normalized by an apparent activation energy term with an apparent activation energy of 343 kJ/mol.

There is a remarkable difference of the creep behaviour between indentation and tensile creep as far as the shape of the corresponding creep curves is concerned. The indentation creep curves are characterized by a pronounced secondary creep stage with a constant indentation rate (Fig. 21). In contrast, the tensile creep curves show a sharp creep rate minimum in the secondary creep stage followed by tertiary creep (Skrotzki *et al.*, 1999), which is absent in indentation creep testing. The minimum creep rates were used to analyse the stress and temperature dependence of creep in uniaxial testing (Fig. 28, Skrotzki *et al.*, 1999), while the stress and temperature dependence of indentation creep was determined using the constant

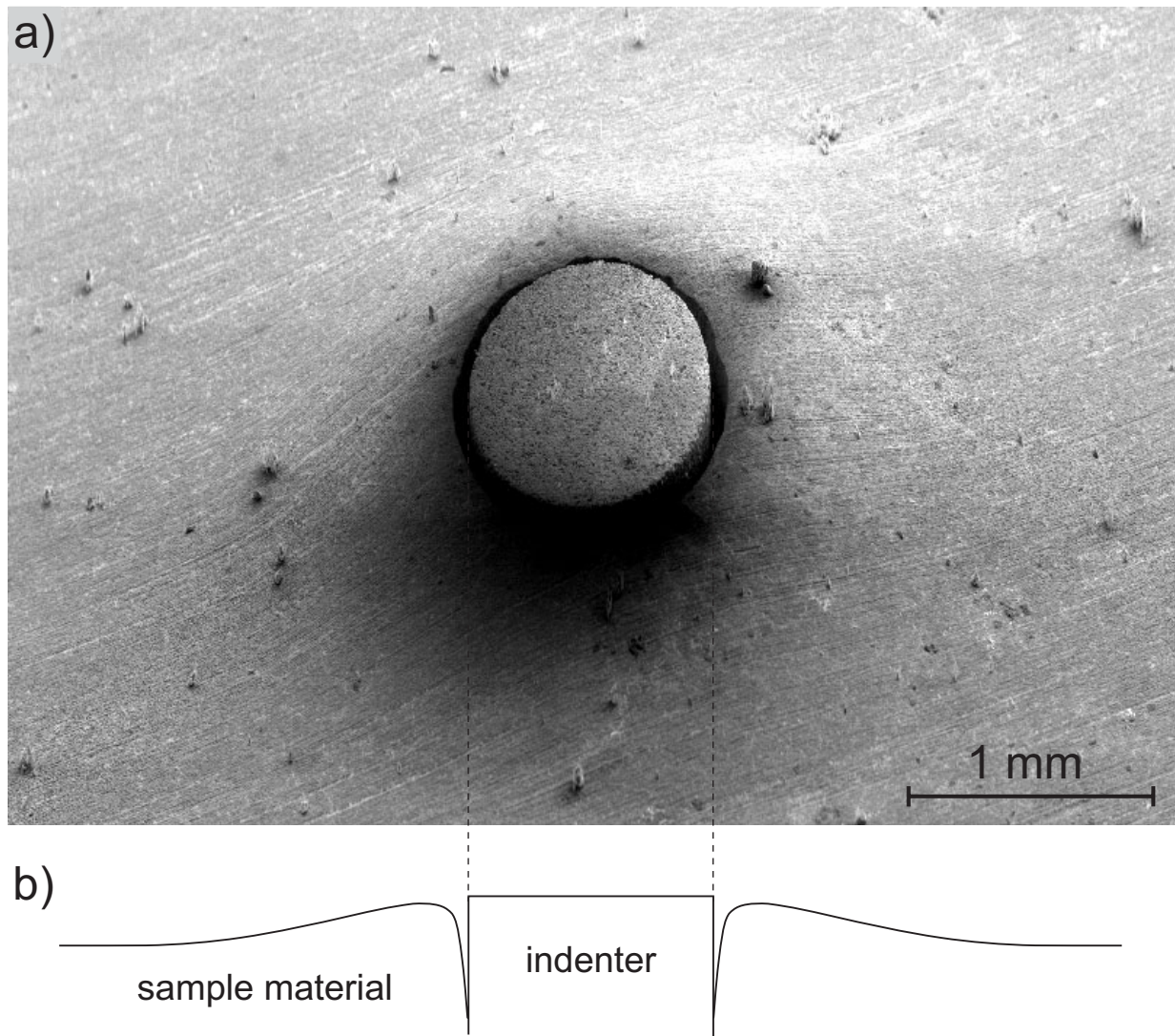


Figure 26: a) Scanning electron microscope image of an indent in a TiAl alloy sample with the indenter still in place (oblique top view). The surrounding surface shows a distinct surface bulge. Between the indenter and the indented material a gap is visible. b) Schematic side view of the surface bulge and the gap that formed during indentation creep.

indentation rates. This yields a good correspondence of the creep parameters obtained from both kinds of creep testing (Fig. 28).

Our indentation creep data are supported by the good agreement with results from conventional uniaxial creep tests on the same material. However, they are in contrast with indentation creep data recently reported by Rao and Swamy (1995). These authors performed indentation creep tests on a TiAl alloy with a slightly different chemical composition and microstructure placing their main emphasis on the investigation of the influence of microstructure on the stress and temperature dependence of creep. Their stress exponent of 1.2 is low compared to 3.2 observed in our study at a comparable stress level (Tab. 7).

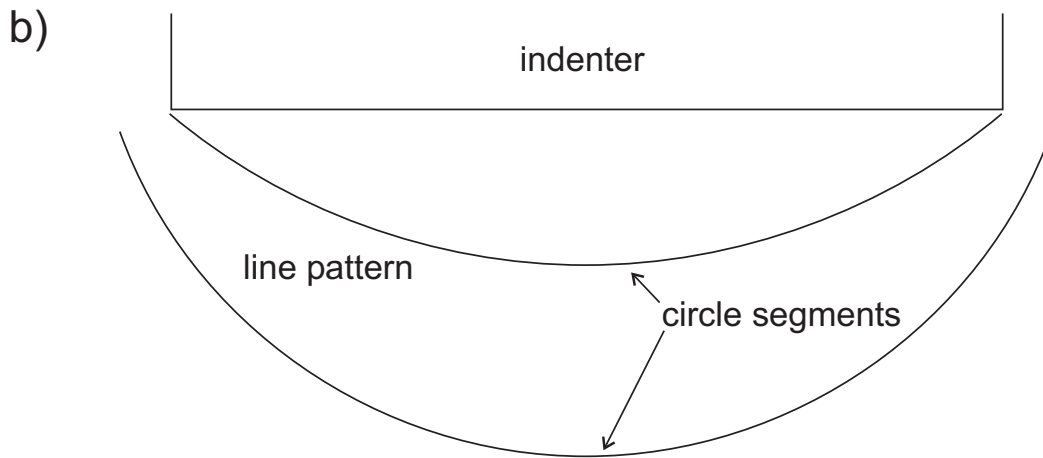
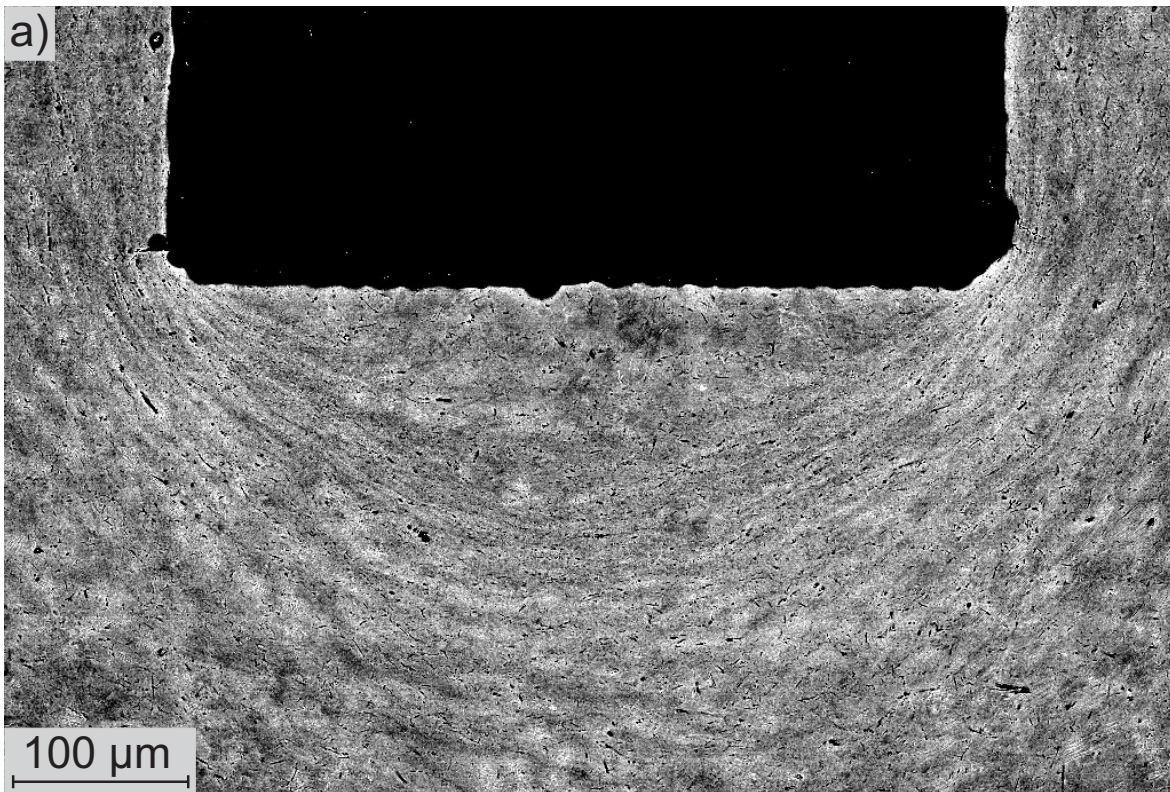


Figure 27: a) Scanning electron microscope image of an indent in a TiAl alloy sample with the indenter still in place (side view). In front of the indenter a pattern of light and dark lines is visible reflecting the pattern of material flow during indentation. b) Schematic drawing of the line pattern in front of the indenter. The lines can be approximated by circle segments.

Moreover, the apparent activation energy of 185 kJ/mol determined by Rao and Swamy (1995) for a volume fraction of lamellar grains of 22% is significantly lower than the value of 343 kJ/mol of the present study.

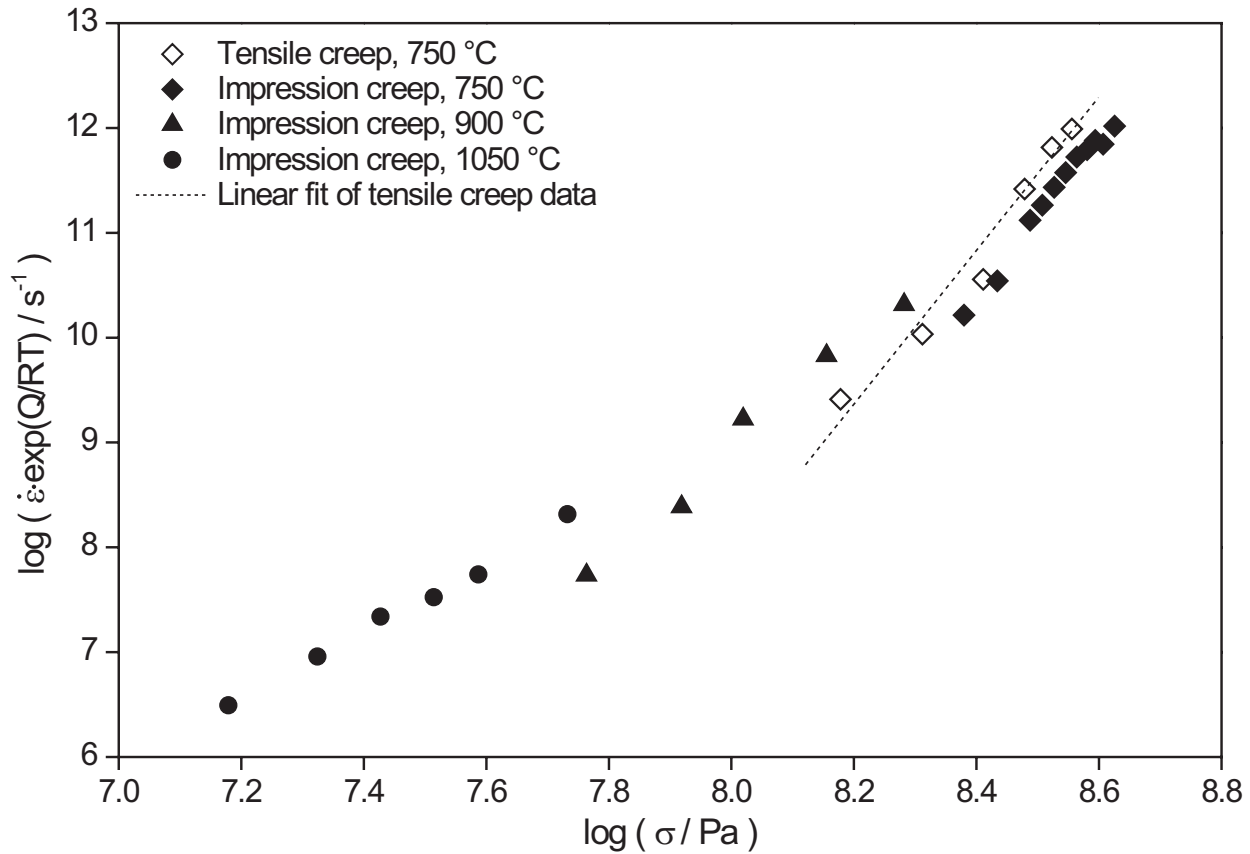


Figure 28: Log-log plot of the temperature compensated strain rate $\dot{\epsilon} \exp(Q/RT)$ versus creep stress σ . The indentation rates and net section stresses determined from indentation creep tests are converted into reference strain rates and reference uniaxial stresses according to equations 6 and 7, respectively. The conversion factors $c_1=0.296$ and $c_2=0.755$ obtained from finite element calculations by Hyde *et al.* (1993) were used.

4.5.2 Material bulging and dislocation mechanisms during indentation creep

Here we propose a simple dislocation model to describe material flow during indentation with a cylindrical indenter (Fig. 29). It is based on the idea of prismatic loop punching, which was first proposed as a possible dislocation mechanism by Seitz (1950), who was inspired by experimental observations of Smakula and Klein (1949). Our simple model material is characterized by two intersecting slip systems. During the indentation process prismatic dislocation loops form around the cylindrical indenter, while the same number of prismatic dislocation loops with opposite sign are punched into the material in front of the indenter (Fig. 29a). An approximate number n of punched prismatic loops can be estimated as $n=d/b$, where d is the indentation depth and b the magnitude of the Burgers vector (Fig. 29a). The prismatic dislocation loops may well be sessile, because their Burgers vector is not a common slip vector for our model material. However, the sessile prismatic loops can decompose into normal dislocation loops which can glide (Fig. 29b).

This simple model can rationalize why half of the material displaced by the indenter is found in the surface bulge adjacent to the indent. If we assume that a punched prismatic dislocation loop decomposes (Fig. 29b), then the dislocation segments characterized by a Burgers vector with a vertical component pointing upwards can reach the sample surface and form surface steps (Fig. 29c). Many such steps can give rise to the formation of a surface bulge around the indenter. Only half of the dislocation segments reach the sample surface (Fig. 29c). Those dislocation segments with vertical Burgers vector components pointing downwards glide into the interior of the sample and therefore do not contribute to the formation of the surface bulge. Thus, in our simple model half of the displaced material is transported to the sample surface in agreement with our experimental observations.

We now make an attempt to rationalize the shape of the surface bulge around the indenter (Fig. 26). Within each depth interval the same number of dislocations is created and the displaced amount of material is the same. When a volume element is displaced deeper inside the material, our glide geometry implies that the associated amount of material is distributed within a larger surface ring area (Fig. 29d). Therefore, the same amount of material creates a smaller height increase of the sample surface when it comes from deeper inside. Thus, the height of the bulge decreases with increasing distance from the indenter, which is also observed by investigation of the experimentally generated indents (Fig. 26).

Our simple dislocation model considers only two slip systems, and thus strictly applies only for single crystals with two slip systems. For a polycrystalline material this model can only qualitatively account for the observed effects.

4.6 Summary and conclusions

The present study investigates the indentation and tensile creep behaviour of a TiAl alloy. Two approaches reported in the literature are used to compare the creep data obtained from both kinds of creep testing. Furthermore, the morphology of the indent and the deformed volume in front of the indenter are studied. The following conclusions can be drawn.

(1) In a limited stress range the indentation creep data can be described by a constant stress exponent, which is also observed in uniaxial creep testing. A stress exponent of 3.2 was determined for a test temperature of 1050 °C and net section stresses ranging from about 50 MPa to 180 MPa. For 900 °C and net section stresses of about 200 MPa to 650 MPa the stress exponent is 5.2. For higher net section stresses of about 810 MPa to 1430 MPa and a temperature of 750 °C a stress exponent of 7.6 was found from the indentation creep tests. Thus, the stress exponent increases with increasing net section stress.

(2) From the indentation creep experiments an apparent activation energy of 343 kJ/mol

was determined for a net section stress of about 180 MPa and for temperatures ranging from about 850 °C to 1050 °C. This activation energy is consistent with values of 288 kJ/mol to 398 kJ/mol obtained from uniaxial tensile creep tests.

(3) The theoretical results of Yue *et al.* (2000), indicating that the stress exponents for indentation creep and uniaxial creep are identical, can be confirmed for an engineering alloy. For the same test temperature of 750 °C both the tensile and the indentation creep data yield a stress exponent near 7.5.

(4) A very good correlation of indentation and tensile creep data for the TiAl alloy is observed, where the data are compared using conversion factors determined by Hyde *et al.* (1993), which relate net section stresses to uniaxial stresses and indentation rates to uniaxial strain rates, respectively.

(5) A simple dislocation model is proposed to rationalize material flow in indentation creep testing.

(6) The good correspondence of the indentation and tensile creep results on an engineering alloy demonstrates that indentation creep testing can be used to characterize creep. This might be especially useful in cases where conventional uniaxial creep tests cannot be applied, e. g. if only small amounts of material are available, if the machining of the sample material is difficult, or if the local deformation behaviour of e. g. thin films or particles in composites must be analysed.

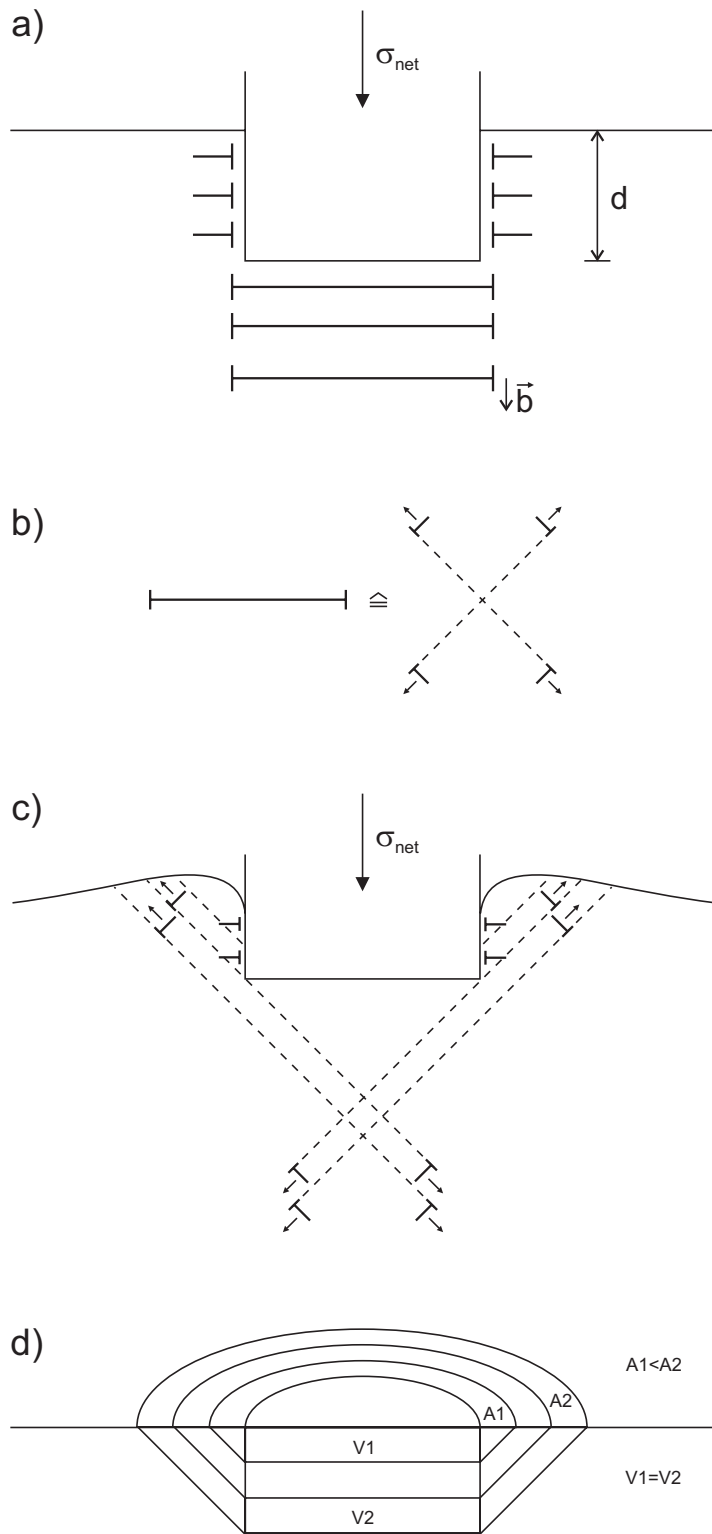


Figure 29: Simple dislocation model describing the indentation process in an indentation creep test. a) Formation of prismatic dislocation loops during indentation with a cylindrical indenter. b) Decomposition of a prismatic dislocation loop into two normal dislocations. c) Dislocation glide to the sample surface accounts for material bulging around the indenter. d) During indentation with a cylindrical indenter the displaced material volume is the same within each depth interval ($V1=V2$). As the ring surface area, that can be reached by the displaced material, increases with increasing indentation depth ($A1 < A2$), the surface height of the bulge decreases with increasing distance from the indenter.

5 Summary and conclusions

5.1 Microindentation hardness tests

Two major parts of this thesis (Chaps. 2, 3) deal with results of high-temperature microindentation hardness tests on minerals using a pyramid-shaped Vickers indenter. These experiments are simple and can be performed on single grains within natural polyphase aggregates (Chaps. 1.4.2, 3.2, 2.2). Therefore, indentation hardness tests are useful to investigate the rheological behaviour of minerals that are not available as natural monophase aggregates with properties suitable for conventional rock deformation experiments. The indentation hardness study on olivine (Chap. 2) revealed that this kind of deformation experiment can be used to investigate mechanical anisotropy of minerals. The morphology of the indents provides information on the activated slip systems. The study on the clinopyroxene solid solution series with the end members jadeite and diopside (Chap. 3) demonstrates how indentation hardness tests can be used to investigate the relative strength of minerals. These results can also provide a base for the classification of minerals into isomechanical groups. Due to extremely high stresses during the deformation process, indentation hardness tests address the low-temperature plasticity regime, which is important in specific tectonic settings (Chap. 2.5.2). The dislocation creep regime, which is more widespread in natural rock deformation, cannot be addressed by this approach. Moreover, indentation hardness tests are not suitable to derive flow law parameters, because of the complex stress and strain field in space and time during indentation (Chap. 1.4.2).

5.2 Indentation creep experiments

The third part of this thesis (Chap. 4) reports on the design and results of indentation creep experiments using a cylindrical indenter. Compared to indentation hardness tests with a pyramid-shaped indenter, indentation creep tests with a cylindrical indenter have the advantage that the net section stress on the indenter remains constant during the experiment (Chap. 4.2) and steady state deformation is possible (Chap. 4.4). Also, the magnitude of stress is lower and the dislocation creep regime can be studied. The creep parameters derived from indentation creep experiments on a TiAl alloy with a complex microstructure, which serves as a model material for a polycrystalline silicate aggregate, compare very well to those obtained in conventional uniaxial creep tests (Chap. 4.5.1). Indentation creep tests are thus expected to be useful for the investigation of the rheological behaviour of phases, that are not available as natural rocks with properties suitable for conventional

rock deformation experiments. For instance, creep experiments using a dead-load creep apparatus are usually performed on single crystals because of problems with grain boundary cracking in polycrystalline aggregates (e. g. Mackwell *et al.*, 1990a). However, homogeneous and perfect single crystals with appropriate dimensions are rarely available. Our results indicate that indentation creep experiments in a dead-load creep apparatus can also be used to investigate the mechanical behaviour of polycrystalline materials, since the hydrostatic stress component provided by the load on the sample during the indentation test suppresses brittle failure.

Finally, the microstructure that develops during indentation creep of the engineering alloy reveals a distinct flow pattern in front of the indenter. This indicates that indentation creep tests are also suitable to study the microstructures and fabrics along small scale strain and strain rate gradients in geological materials, especially the development of preferred orientations in non-coaxial deformation (Kunze and Avé Lallemant, 1981). As the state of stress and the resulting flow field can be simulated for the cylindrical indenter geometry, this simple approach is expected to provide valuable insight into the microstructural history of inhomogeneously deformed materials.

References

- Aines, R.D. and Rossman, G.R. 1984. Water in minerals? A peak in the infrared. *Journal of Geophysical Research*, **89**(B6), 4059–4070.
- Avé Lallemant, H.G. 1978. Experimental deformation of diopside and websterite. *Tectonophysics*, **48**, 1–27.
- Bai, Q., Mackwell, S.J. and Kohlstedt, D.L. 1991. High-temperature creep of olivine single crystals, 1. Mechanical results for buffered samples. *Journal of Geophysical Research*, **96**(B2), 2441–2463.
- Bai, W., Mei, S. and Kohlstedt, D.L. 1997. Rheology of partially molten olivine aggregates under water-saturated conditions. *Continental Dynamics*, **2**(1), 54–62.
- Becker, A.A., Hyde, T.H. and Xia, L. 1994. Numerical analysis of creep in components. *Journal of Strain Analysis*, **29**(3), 185–192.
- Bell, P.M. 1964. High-pressure melting relations for jadeite composition. *Pages 171–174 of: Yearbook 63*. Carnegie Institution of Washington.
- Berns, H. and Lührig, M. 1994. Mikrohärte bei erhöhter Temperatur prüfen. *Materialprüfung*, **36**(6), 223–226.
- Blenkinsop, T.G. and Drury, M.R. 1988. Stress estimates and fault history from quartz microstructures. *Journal of Structural Geology*, **10**(7), 673–684.
- Blumenauer, H. 1994. *Werkstoffprüfung*. Deutscher Verlag für Grundstoffindustrie.
- Brace, W.F. 1960. Behavior of rock salt, limestone, and anhydrite during indentation. *Physics of the Earth and Planetary Interiors*, **65**(6), 1773–1788.
- Brace, W.F. 1963. Behavior of quartz during indentation. *The Journal of Geology*, **71**(5), 581–595.
- Brace, W.F. 1964. Indentation hardness of minerals and rocks. *Neues Jahrbuch für Mineralogie. Monatshefte*, **9-11**, 257–269.
- Brenker, F.E., Prior, D.J. and Müller, W.F. 2002. Cation ordering in omphacite and effect on deformation mechanism and lattice preferred orientation (LPO). *Journal of Structural Geology*, **24**(12), 1991–2005.
- Brookes, C.A., O'Neill, J.B. and Redfern, B.A.W. 1971. Anisotropy in the hardness of single crystals. *Proceedings of the Royal Society of London, A*, **322**, 73–88.
- Butt, D.P., Korzekwa, D.A., Maloy, S.A., Kung, H. and Petrovic, J.J. 1996. Impression creep behavior of SiC particle-MoSi₂ composites. *Journal of Materials Research*, **11**(6), 1528–1536.
- Bystricky, M., Kunze, K., Burlini, L. and Burg, J.-P. 2000. High shear strain of olivine aggregates: Rheological and seismic consequences. *Science*, **290**, 1564–1567.
- Cameron, M., Sueno, S., Prewitt, C.T. and Papike, J.J. 1973. High-temperature crystal chemistry of acmite, diopside, hedenbergite, jadeite, spodumene, and ureyite. *American Mineralogist*, **58**, 594–618.

- Carpenter, M.A. 1978. Kinetic control of ordering and exsolution in omphacite. *Contributions to Mineralogy and Petrology*, **67**, 17–24.
- Carpenter, M.A. 1980. Mechanisms of exsolution in sodic pyroxenes. *Contributions to Mineralogy and Petrology*, **71**, 289–300.
- Carpenter, M.A. 1981. Time-temperature-transformation (TTT) analysis of cation disordering in omphacite. *Contributions to Mineralogy and Petrology*, **78**, 433–440.
- Carter, N.L. and Avé Lallemant, H.G. 1970. High temperature flow of dunite and peridotite. *Geological Society of America Bulletin*, **81**, 2181–2202.
- Carter, N.L. and Tsenn, M.C. 1987. Flow properties of continental lithosphere. *Tectonophysics*, **136**, 27–63.
- Chiang, D. and Li, J.C.M. 1994. Impression creep of lead. *Journal of Materials Research*, **9**(4), 903–908.
- Chiang, S.S., Marshall, D.B. and Evans, A.G. 1982. The response of solids to elastic/plastic indentation. I. Stresses and residual stresses. *Journal of Applied Physics*, **53**(1), 298–311.
- Chu, S.N.G. and Li, J.C.M. 1977. Impression creep; a new creep test. *Journal of Materials Science*, **12**, 2200–2208.
- Chu, S.N.G. and Li, J.C.M. 1979. Impression creep of β -tin single crystals. *Materials Science and Engineering*, **39**, 1–10.
- Cseh, G., Bär, J., Gudladt, H.-J., Lendvai, J. and Juhász, A. 1999. Indentation creep in a short fibre-reinforced metal matrix composite. *Materials Science and Engineering*, **A272**, 145–151.
- Darot, M., Gueguen, Y., Benchemam, Z. and Gaboriaud, R. 1985. Ductile-brittle transition investigated by micro-indentation: results for quartz and olivine. *Physics of the Earth and Planetary Interiors*, **40**, 180–186.
- Dimanov, A., Dresen, G. and Wirth, R. 1998. High-temperature creep of partially molten plagioclase aggregates. *Journal of Geophysical Research*, **103**(B5), 9651–9664.
- DIN50133. 1985. *Härteprüfung nach Vickers*. Deutsches Institut für Normung e.V.
- Dorner, D., Schellewald, M. and Stöckhert, B. in review. Hardness anisotropy and slip systems of olivine investigated by high-temperature microindentation hardness tests. *Tectonophysics*.
- Duffy, T.S. and Anderson, D.L. 1989. Seismic velocity in mantle minerals and the mineralogy of the upper mantle. *Journal of Geophysical Research*, **94**(B2), 1895–1912.
- Duyster, J. and Stöckhert, B. 2001. Grain boundary energies in olivine derived from natural microstructures. *Contributions to Mineralogy and Petrology*, **140**, 567–576.
- Evans, B. 1984. The effect of temperature and impurity content on indentation hardness of quartz. *Journal of Geophysical Research*, **89**(B6), 4213–4222.
- Evans, B. and Goetze, Ch. 1979. The temperature variation of hardness of olivine and its implication for polycrystalline yield stress. *Journal of Geophysical Research*, **84**(B10), 5505–5524.

- Evans, B. and Kohlstedt, D.L. 1995. Rheology of rocks. *Pages 148–165 of: Rock Physics and Phase Relations - A Handbook of Physical Constants*. American Geophysical Union.
- Fleet, M.E., Herzberg, C.T., Bancroft, G.M. and Aldridge, L.P. 1978. Omphacite studies, I. The P2/n \rightarrow C2/c transformation. *American Mineralogist*, **63**, 1100–1106.
- Frost, H.J. and Ashby, M.F. 1982. *Deformation-Mechanism Maps*. Pergamon Press.
- Gerk, A.P. 1977. The effect of work-hardening upon the hardness of solids: minimum hardness. *Journal of Materials Science*, **12**, 735–738.
- Godavarti, P.S. and Murty, K.L. 1987. Creep anisotropy of zinc using impression tests. *Journal of Materials Science Letters*, **6**, 456–458.
- Green, H.W. and Borch, R.S. 1989. A new molten salt cell for precision stress measurement at high pressure. *European Journal of Mineralogy*, **1**, 213–219.
- Groshong, R.H. 1988. Low-temperature deformation mechanisms and their interpretation. *Geological Society of America Bulletin*, **100**, 1329–1360.
- Guyot, P. and Dorn, J.E. 1967. A critical review of the Peierls mechanism. *Canadian Journal of Physics*, **45**, 983–1016.
- Handy, M.R., Braun, J., Brown, M., Kukowski, N., Paterson, M.S., Schmid, S.M., Stöckhert, B., Stüwe, K., Thompson, A.B. and Wosnitza, E. 2001. Rheology and geodynamic modelling: the next step forward. *International Journal of Earth Sciences (Geologische Rundschau)*, **90**, 149–156.
- Hyde, T.H., Yehia, K.A. and Becker, A.A. 1993. Interpretation of impression creep data using a reference stress approach. *International Journal of Mechanical Sciences*, **35**(6), 451–462.
- Hyde, T.H., Yehia, K.A. and Becker, A.A. 1995. Application of the reference stress method for interpreting impression creep test data. *Materials at High Temperatures*, **13**(3), 133–138.
- Ji, S. and Zhao, P. 1993. Flow laws of multiphase rocks calculated from experimental data on the constituent phases. *Earth and Planetary Science Letters*, **117**, 181–187.
- Ji, S. and Zhao, P. 1994. Strength of two-phase rocks: a model based on fiber-loading theory. *Journal of Structural Geology*, **16**(2), 253–262.
- Johnson, K. L. 1970. The correlation of indentation experiments. *Journal of the Mechanics and Physics of Solids*, **18**, 115–126.
- Juhász, A., Tasnádi, P., Szászvári, P. and Kovács. 1986. Investigation of the superplasticity of tin-lead eutectic by impression creep tests. *Journal of Materials Science*, **21**, 3287–3291.
- Kameyama, M., Yuen, D.A. and Karato, S. 1999. Thermal-mechanical effects of low-temperature plasticity (the Peierls mechanism) on the deformation of a viscoelastic shear zone. *Earth and Planetary Science Letters*, **168**, 159–172.
- Karato, S. 1989. Defects and plastic deformation in olivine. *Pages 176–208 of: Karato, S. and Toriumi, M. (eds), Rheology of Solids and of the Earth*. Oxford University Press.

- Karato, S., Wang, Z., Liu, B. and Fujino, K. 1995a. Plastic deformation of garnets: systematics and implications for the rheology of the mantle transition zone. *Earth and Planetary Science Letters*, **130**, 13–30.
- Karato, S., Wang, Z., Liu, B. and Fujino, K. 1995b. Plastic deformation of garnets: systematics and implications for the rheology of the mantle transition zone. *Earth and Planetary Science Letters*, **130**, 13–30.
- Karato, S., Riedel, M.R. and Yuen, D.A. 2001. Rheological structure and deformation of subducted slabs in the mantle transition zone: implications for mantle circulation and deep earthquakes. *Physics of the Earth and Planetary Interiors*, **127**, 83–108.
- Kelly, A. 1966. *Strong Solids*. Clarendon Press.
- Kirby, S.H. 1980. Tectonic stresses in the lithosphere: constraints provided by the experimental deformation of rocks. *Journal of Geophysical Research*, **85**(B11), 6353–6363.
- Kohlstedt, D.L., Evans, B. and Mackwell, S.J. 1995. Strength of the lithosphere: Constraints imposed by laboratory experiments. *Journal of Geophysical Research*, **100**(B9), 17587–17602.
- Kollé, J.J. and Blacic, J.D. 1982. Deformation of single-crystal clinopyroxenes: 1. Mechanical twinning in diopside and hedenbergite. *Journal of Geophysical Research*, **87**(B5), 4019–4034.
- Kollenberg, W. 1986. Microhardness measurement of haematite crystals at temperatures up to 900 °C. *Journal of Materials Science*, 4310–4314.
- Kollenberg, W. 1988. Plastic deformation of Al₂O₃ single crystals by indentation at temperatures up to 750 °C. *Journal of Materials Science*, **23**, 3321–3325.
- Kunze, F.R. and Avé Lallemant, H.G. 1981. Non-coaxial experimental deformation of olivine. *Tectonophysics*, **74**, T1–T13.
- Küster, M. and Stöckhert, B. 1999. High differential stress and sublithostatic pore fluid pressure in the ductile regime - microstructural evidence for short-term post-seismic creep in the Sesia Zone, Western Alps. *Tectonophysics*, **303**, 263–277.
- Li, J.C.M. 2002. Impression creep and other localized tests. *Materials Science and Engineering*, **A322**(1-2), 23–42.
- Lloyd, G.E. 2000. Grain boundary contact effects during faulting of quartzite: an SEM/EBSD analysis. *Journal of Structural Geology*, **22**, 1675–1693.
- Lloyd, G.E. and Knipe, R.J. 1992. Deformation mechanisms accommodating faulting of quartzite under upper crustal conditions. *Journal of Structural Geology*, **14**(2), 127–143.
- Lührig, M. 1993. *Temperaturabhängigkeit der Mikrohärtigkeit von Mischkristallen in Phasengemischen*. Fortschritt-Berichte VDI, no. 297. VDI-Verlag.
- Mackwell, S.J., Kohlstedt, D.L. and Paterson, M.S. 1985. The role of water in the deformation of olivine single crystals. *Journal of Geophysical Research*, **90**(B13), 11319–11333.
- Mackwell, S.J., Kohlstedt, D.L. and Durham, W.B. 1990a. High-resolution creep apparatus. *Pages 235–238 of: Duda, A.G., Durham, W.B., Handin, J.W. and Wang, H.F. (eds), The Brittle-Ductile Transition in Rocks*, vol. 56. American Geophysical Union.

- Mackwell, S.J., Bai, Q. and Kohlstedt, D.L. 1990b. Rheology of olivine and the strength of the lithosphere. *Geophysical Research Letters*, **17**(1), 9–12.
- Marshall, D.B. and Lawn, B.R. 1986. Indentation of brittle materials. *Pages 26–46 of: Blau, P.J. and Lawn, B.R. (eds), Microindentation Techniques in Materials Science and Engineering*. ASTM STP 889. American Society for Testing and Materials.
- Mauler, A., Bystricky, M., Kunze, K. and Mackwell, S. 2000. Microstructures and lattice preferred orientations in experimentally deformed clinopyroxene aggregates. *Journal of Structural Geology*, **22**(11-12), 1633–1648.
- McLaren, A.C. and Hobbs, B.E. 1972. Transmission electron microscope investigation of some naturally deformed quartzites. *Pages 55–66 of: Heard, H.C., Borg, I.Y., Carter, N.L. and Raleigh, C.B. (eds), Flow and Fracture of Rocks*. Geophysical Monograph Series, vol. 16. American Geophysical Union.
- Mei, S. and Kohlstedt, D.L. 2000a. Influence of water on plastic deformation of olivine aggregates, 1. Diffusion creep regime. *Journal of Geophysical Research*, **105**(B9), 21457–21469.
- Mei, S. and Kohlstedt, D.L. 2000b. Influence of water on plastic deformation of olivine aggregates, 1. Dislocation creep regime. *Journal of Geophysical Research*, **105**(B9), 21471–21481.
- Mercier, J.-C.C. 1985. Olivine and pyroxenes. *Chap. 19, pages 407–430 of: Wenk, H.-R. (ed), Preferred Orientation in Deformed Metals and Rocks: An Introduction to Modern Texture Analysis*. Academic Press.
- Miller, G.H., Rossman, G.R. and Harlow, G.E. 1987. The natural occurrence of hydroxide in olivine. *Physics and Chemistry of Minerals*, **14**, 461–472.
- Murthy, G.S. and Sastry, D.H. 1982. Impression creep of zinc and the rate-controlling dislocation mechanism of plastic flow at high temperatures. *Physica Status Solidi (a)*, **70**, 63–71.
- Nabarro, F.R.N. 1967. *Theory of Crystal Dislocations*. Clarendon Press.
- Orzol, J., Stöckhert, B. and Rummel, F. 2002. An experimental study of the rheology of jadeite. *Eos Transactions AGU, Fall Meeting Supplement*, **83**(47). Abstract MR51A-11.
- Orzol, J., Trepmann, C., Stöckhert, B. and Shi, G. 2003. Critical shear stress for mechanical twinning of jadeite - an experimental study. *Tectonophysics*, **372**(3-4), 135–145.
- Paterson, M.S. 1970. A high-pressure, high-temperature apparatus for rock deformation. *International Journal of Rock Mechanics and Mining Sciences*, **7**, 517–526.
- Paterson, M.S. 1982. The determination of hydroxyl by infrared absorption in quartz, silicate glasses and similar materials. *Bull. Minéral.*, **105**, 20–29.
- Paterson, M.S. 1987. Problems in the extrapolation of laboratory rheological data. *Tectonophysics*, **133**, 33–43.
- Paterson, M.S. 2001. Relating experimental and geological rheology. *International Journal of Earth Sciences (Geologische Rundschau)*, **90**, 157–167.

- Paterson, M.S. and Olgaard, D.L. 2000. Rock deformation tests to large shear strains in torsion. *Journal of Structural Geology*, **22**, 1341–1358.
- Phakey, P., Dollinger, G. and Christie, J. 1972. Transmission electron microscopy of experimentally deformed olivine crystals. *Pages 117–138 of: Heard, H.C., Borg, I.Y., Carter, N.L. and Raleigh, C.B. (eds), Flow and Fracture of Rocks*. Geophysical Monograph Series, vol. 16. American Geophysical Union.
- Piepenbreier, D. and Stöckhert, B. 2001. Plastic flow of omphacite in eclogites at temperatures below 500 °C - implications for interplate coupling in subduction zones. *International Journal of Earth Sciences (Geologische Rundschau)*, **90**, 197–210.
- Poirier, J.-P. 1975. On the slip systems of olivine. *Journal of Geophysical Research*, **80**(29), 4059–4061.
- Poirier, J.-P. 1985. *Creep of Crystals*. Cambridge University Press.
- Poumellec, B. and Jaoul, O. 1984. Influence of pO₂ and pH₂O on the high temperature plastic behaviour of olivine. *Pages 281–305 of: Tressler, R.E. and Bradt, R.C. (eds), Deformation of Ceramic Materials II*. Materials Science Research, vol. 18. Plenum Press.
- Prior, D.J., Boyle, A.P., Brenker, F., Cheadle, M.C., Day, A., Lopez, G., Peruzzo, L., Potts, G., Reddy, S., Spiess, R., Timms, N.E., Trimby, P., Wheeler, J. and Zetterstrom, L. 1999. The application of electron backscatter diffraction and orientation contrast imaging in the SEM to textural problems in rocks. *American Mineralogist*, **84**(11-12), 1741–1759.
- Raleigh, C.B. 1968. Mechanisms of plastic deformation of olivine. *Journal of Geophysical Research*, **73**(14), 5391–5406.
- Ranalli, G. 1987. *Rheology of the Earth*. Allen & Unwin.
- Rao, P.P. and Swamy, K.S. 1995. Effect of microstructure on the impression creep of two-phase titanium aluminide. *Zeitschrift für Metallkunde*, **86**(11), 760–763.
- Ricoult, D.L. and Kohlstedt, D.L. 1985. Experimental evidence for the effect of chemical environment upon the creep rate of olivine. *Pages 171–184 of: Shock, R.N. (ed), Point Defects in Minerals*. Geophysical Monograph, vol. 31. American Geophysical Union.
- Rutter, E.H. 1986. On the nomenclature of mode of failure transitions in rocks. *Tectonophysics*, **122**, 381–387.
- Rutter, E.H. 1993. Experimental rock deformation: techniques, results and applications to tectonics. *Contributions to Mineralogy and Petrology*, 61–65.
- Rybacki, E., Renner, J., Konrad, K., Harbott, W., Rummel, F. and Stöckhert, B. 1998. A servohydraulically-controlled deformation apparatus for rock deformation under conditions of ultra-high pressure metamorphism. *Pure and Applied Geophysics*, **152**, 579–606.
- Samuels, L.E. 1986. Microindentations in metals. *Pages 5–25 of: Blau, P. J. and Lawn, B. R. (eds), Microindentation techniques in materials science and engineering*. ASTM STP 889. American Society for Testing and Materials.
- Schmid, E. and Boas, W. 1950. *Plasticity of crystals*. London: Hughes.

- Schmid, S.M. 1982. Microfabric studies as indicators of deformation mechanisms and flow laws operative in mountain building. *Chap. 1-8, pages 95–110 of: Hsue, K.J. (ed), Mountain Building Processes.* Academic Press.
- Scholz, C.H. 1990. *The mechanics of earthquakes and faulting.* Cambridge University Press.
- Schwarz, S. and Stöckhert, B. 1996. Pressure solution in siliciclastic HP-LT metamorphic rocks - constraints on the state of stress in deep levels of accretionary complexes. *Tectonophysics*, **255**, 203–209.
- Seitz, F. 1950. Prismatic dislocations and prismatic punching in crystals. *Physical Review*, **79**, 723–724.
- Skrotzki, B., Rudolf, T. and Eggeler, G. 1999. Creep behavior and microstructural evolution of a near- γ -TiAl alloy with duplex microstructure. *Zeitschrift für Metallkunde*, **90**(6), 393–402.
- Smakula, A. and Klein, M.W. 1949. The plastic deformation and crystal orientation of thallium halides. *Journal of the Optical Society of America*, **39**(6), 445–453.
- Stöckhert, B. 2002. Stress and deformation in subduction zones: insight from the record of exhumed high pressure metamorphic rocks. *Pages 255–274 of: de Meer, S., Drury, M.R., de Bresser, J.H.P. and Pennock, G.M. (eds), Deformation mechanisms, Rheology, and Tectonics: Current Status and Future Perspectives.* Special Publication, vol. 200. Geological Society of London.
- Stöckhert, B. and Renner, J. 1998. Rheology of crustal rocks at ultrahigh pressure. *Chap. 3, pages 57–95 of: Hacker, B.R. and Liou, J.G. (eds), When Continents Collide: Geodynamics and Geochemistry of Ultrahigh-Pressure Rocks.* Kluwer Academic Publishers.
- Stöckhert, B., Brix, M.R., Kleinschrodt, R., Hurford, A.J. and Wirth, R. 1999a. Thermochronometry and microstructures of quartz - a comparison with experimental flow laws and predictions on the temperature of the brittle-plastic transition. *Journal of Structural Geology*, **21**, 351–369.
- Stöckhert, B., Brix, M.R., Kleinschrodt, R., Hurford, A.J. and Wirth, R. 1999b. Thermochronometry and microstructures of quartz - a comparison with experimental flow laws and predictions on the temperature of the brittle-plastic transition. *Journal of Structural Geology*, **21**, 351–369.
- Suzuki, T., Takeuchi, S. and Yoshinaga, H. 1991. *Dislocation Dynamics and Plasticity.* Springer.
- Swain, M.V. and Atkinson, B.K. 1978. Fracture surface energy of olivine. *Pure and Applied Geophysics*, **116**, 866–872.
- Tabor, D. 1951. *The hardness of metals.* Clarendon Press.
- Tabor, D. 1970. The hardness of solids. *Review of Physics in Technology*, **1**, 145–179.
- Tabor, D. 1986. Indentation hardness and its measurement: some cautionary comments. *Pages 129–159 of: Blau, P.J. and Lawn, B.R. (eds), Microindentation techniques in materials science and engineering.* ASTM STP 889. American Society for Testing and Materials.

- Tasnádi, P., Juhász, A., Chinh, N.Q. and Kovács, I. 1988. Theoretical description of the deformation taking place in an impression test. *Res Mechanica*, **24**, 335–347.
- Teter, D.M. 1998. Computational alchemy: the search for new superhard materials. *MRS Bulletin*, **23**(1), 22–27.
- Trepmann, C. and Stöckhert, B. 2001. Mechanical twinning of jadeite - an indication of synseismic loading beneath the brittle-ductile transition. *International Journal of Earth Sciences (Geologische Rundschau)*, **90**(1), 4–13.
- Trepmann, C. and Stöckhert, B. 2002. Cataclastic deformation of garnet: a record of synseismic loading and postseismic creep. *Journal of Structural Geology*, **24**(11), 1845–1856.
- Tullis, T.E. 1980. The use of mechanical twinning in minerals as a measure of shear stress magnitudes. *Journal of Geophysical Research*, **85**(B11), 6263–6268.
- Tullis, T.E. and Tullis, J. 1986. Experimental rock deformation techniques. *Pages 297–324 of: Hobbs, B.E. and Heard, H.C. (eds), Mineral and Rock Deformation, Laboratory Studies, the Paterson Volume.* Geophysical Monograph, vol. 36. American Geophysical Union.
- Tullis, T.E., Horowitz, F.G. and Tullis, J. 1991. Flow laws of polyphase aggregates from end-member flow laws. *Journal of Geophysical Research*, **96**(B5), 8081–8096.
- Wang, Z., Dresen, G. and Wirth, R. 1996a. Diffusion creep of fine-grained polycrystalline anorthite at high temperatures. *Geophysical Research Letters*, **23**(22), 3111–3114.
- Wang, Z.-C., Bai, Q., Dresen, G., Wirth, R. and Evans, B. 1996b. High-temperature deformation of calcite single crystals. *Journal of Geophysical Research*, **101**(B9), 20377–20390.
- Westbrook, J.H. 1957. Microhardness testing at high temperatures. *Pages 873–897 of: Proceedings of the Sixtieth Annual Meeting*, vol. 57. American Society for Testing and Materials (ASTM).
- Williams, D.W. and Kennedy, G.C. 1969. Melting curve of diopside to 50 kilobars. *Journal of Geophysical Research*, **74**(17), 4359–4366.
- Yu, E.C. and Li, J.C.M. 1977a. Impression creep of LiF single crystals. *Philosophical Magazine*, **36**(4), 811–825.
- Yu, H.Y. and Li, J.C.M. 1977b. Computer simulation of impression creep by the finite element method. *Journal of Materials Science*, **12**, 2214–2222.
- Yu, H.Y., Imam, M.A. and Rath, B.B. 1985. Study of the deformation behaviour of homogeneous materials by impression tests. *Journal of Materials Science*, **20**, 636–642.
- Yue, Z.F., Probst-Hein, M. and Eggeler, G. 2000. Determination of creep parameters from indentation creep experiments: a parametric finite element study for single phase materials. *Materials at High Temperatures*, **17**(4), 449–456.
- Yue, Z.F., Eggeler, G. and Stöckhert, B. 2001. A creep finite element analysis of indentation creep testing in two phase microstructures (particle/matrix- and thin film/substrate-systems). *Computational Materials Science*, **21**, 37–56.

Danksagung

Ich danke allen, die mir mit Rat und Tat geholfen haben, und jenen, die dafür gesorgt haben, dass neben der Arbeit auch der Spass nicht zu kurz kam.

Insbesondere möchte ich dem Betreuer dieser Arbeit, Bernhard Stöckhert, für viele anregende Diskussionen und seine stets motivierende positive Einstellung danken.

Lebenslauf

Name Dorothée Dorner
Geburtsdatum 20. Oktober 1973
Geburtsort Holzminden
Wohnort 44789 Bochum, Drusenbergstrasse 22

Schulbildung

1980 – 1984 Gerhard-Hauptmann-Grundschule, Bergkamen
1984 – 1993 Städtisches Gymnasium, Kamen
1993 Abitur

Hochschulausbildung

1993 – 1999 Studium der Geophysik an der Ruhr-Universität
Bochum
1999 Abschluss des Studiums als Diplom-Geophysikerin

Beschäftigungsverhältnisse

seit 1999 wissenschaftliche Mitarbeiterin am Institut für
Geologie, Mineralogie und Geophysik an der
Ruhr-Universität Bochum

Hiermit erkläre ich, dass ich die vorliegende Arbeit selbstständig und ohne unerlaubte Hilfen ausgeführt und verfasst habe. Die Arbeit ist in dieser oder ähnlicher Form noch bei keiner Fakultät oder einer anderen Hochschule eingereicht worden.

Bochum, November 2002